DEVELOPMENT OF ONLINE CHEMISTRY FOR RUTHERFORDIUM (ELEMENT 104): COMMISSIONING OF A GAS STOPPER AND EXTRACTION CHROMATOGRAPHY OF RUTHERFORDIUM HOMOLOGS (ZIRCONIUM AND HAFNIUM)

A Dissertation
by

MARISA CHRISTINA ALFONSO

Submitted to the Office of Graduate and Professional Studies of
Texas A&M University
in partial fulfillment of the requirements for the degree of

DOCTOR OF PHILOSOPHY

Chair of Committee,	Sherry J. Yennello
Co-Chair of Committee,	Charles M. Folden III
Committee Members,	Abraham Clearfield
	Daniel G. Melconian
Head of Department,	Simon W. North

December 2016

Major Subject: Chemistry

Copyright 2016 Marisa C. Alfonso

ABSTRACT

The chemical and physical properties of the heaviest elements are of particular interest because relativistic effects increase as proton number squared. Transactinides, elements where relativistic effects are expected to be the largest, do not exist naturally; they are produced via fusion-evaporation reactions. The products of these reactions must be degraded down to sub-eV energies for chemical studies. At the Cyclotron Institute at Texas A&M University, a device for the thermalization of fusion-evaporation reaction products, the Recoil Transfer Chamber (RTC), has been designed, fabricated, and characterized. The design of this device is based on a gas stopper previously used at the National Superconducting Cyclotron Laboratory. This device uses a combination of laminar gas flow and static electric field to effectively transport the thermalized ions to the appropriate chemistry experiment. The RTC's efficiency was determined using products of the $^{118}Sn(^{40}Ar, 6n)^{152}Er$ reaction. An efficiency of 34 ± 5% was directly measured.

Additionally, extraction chromatographic systems for the future chemical characterization of Rf were optimized offline. Trace quantities of long-lived radioactive homologs of Rf, ^{89}Zr ($t_{½}$ = 78.41 hr) and ^{175}Hf ($t_{½}$ = 70 d), were used to mimic the "one-atom-at-a-time" nature of transactinide chemistry. The extraction behavior of Zr and Hf was studied in HCl, HNO_3, and H_2SO_4 using TEVA (a trioctyl and tridecyl methyl ammonium-based resin) and UTEVA (a diamyl amylphosphonate-based resin). Batch

uptake studies were performed to determine which systems could separate Zr and Hf. Both resins showed the most promise in an HCl media. A separation factor of 18 ± 8 in 8.4 M HCl was measured using TEVA, while a separation factor of greater than 9.4 in 5.6 M HCl was measured using UTEVA. Offline, both TEVA and UTEVA column studies in HCl had good intergroup separation and showed viability for future extraction chromatographic studies of Rf.

DEDICATION

A mi familia, especialmente a mi abuelo,

porque de él heredé mi amor por las ciencias.

To my family, especially my grandfather,

from whom I inherited my love of the sciences.

ACKNOWLEDGEMENTS

Words cannot accurately describe my gratitude to all the wonderful people who helped me with my dissertation project. I will be forever indebted to all of them.

I would like to start by thanking my advisor, Dr. Charles M. Folden III. Let's just say it has been a crazy journey. As your VERY first student, I experienced all the ups and downs of starting a new research group. I am very grateful for this "special" version of graduate school; it has made me a better and stronger scientist and person.

I would like to express my gratitude to my committee members: Dr. Abraham Clearfield, Dr. Daniel G. Melconian, and Dr. Sherry J. Yennello. In particular, thank you Dr. Yennello for inspiring me to join the nuclear field.

Dr. Dmitriy Mayorov and Dr. Tyler Werke, I have unofficially decided the three of us will be forever known as the "OG" group members. I am so glad that the three of us together played a role in all of our dissertation projects. "Beam Times" will always hold a special place in my heart. Thank you so much for ALL your help with the RTC; that was quite a doozy of a project. Lastly, I am sorry that group meetings ran so much longer when I was present.

Dr. Evgeny Tereshatov, thank you so much for helping me with both the RTC and my radiochemistry project. You are the radiochemist I will always aspire to become.

Cyclotron Institute faculty and staff, thank you so much for EVERYTHING! They say it takes a village to raise a child. Well, I say it takes a village to make a nuclear scientist.

Stephen Molitor and William Seward, the RTC would not have been possible without your help, thank you.

I would also like to thank our collaborators at Lawrence Livermore National Lab and the University of Nevada at Las Vegas. Thank you, Dr. Dawn Shaughnessy, for giving me the opportunity to spend a summer at a national lab. Also, thank you to both Dr. Ken Moody and Dr. John Despotopulos for answering all my questions on my radiochemistry project.

I would also like to acknowledge Eckert and Ziegler Analytics, for giving me the opportunity to continue my career as a nuclear scientist in industry. I am very excited about my future with your company!

My parents, siblings, and friends deserve recognition for their support. Thank you all for being there for me all the times I wanted to throw in the towel and give up. Your words of support were invaluable. To my husband, Ray, you are my rock and without you I would not have survived graduate school. Also, I would like to thank my brother and my now sister-in-law for sharing their college experience with me. I know most people do not experience the “joy” of going to college with their older sister. Gig’em!

Lastly, I would like to thank my funding sources: Department of Energy, the Welch Foundation, and Texas A&M University College of Science.

NOMENCLATURE

k'	Capacity Factor
AC	Aerosol Chamber of Recoil Transfer Chamber
AIDA	Automated Ion-exchange separation apparatus coupled with the Detection system for Alpha spectroscopy
BGS	Berkeley Gas-filled Separator
DP	Pressure difference between Main Chamber and Aerosol Chamber
EVR	Evaporation Residue
GSI	GSI Helmholtz Center for Heavy Ion Research (Darmstadt, Germany)
HPGe	High Purity Germanium Detector
LLNL	Lawrence Livermore National Laboratory
MARS	Momentum Achromat Recoil Spectrometer
MC	Main Chamber of Recoil Transfer Chamber
NSCL	National Superconducting Cyclotron Laboratory
PP	Polypropylene
PSSD	Position-Sensitive Silicon Detector
RF	Radiofrequency
RIKEN	Institute of Physical and Chemical Research (Rikagaku Kenkyusho, Japan)
RTC	Recoil Transfer Chamber
TASCA	TransActinide Separator and Chemistry Apparatus

TBP	Tributylphosphate
TEVA	Trialkyl, Methylammonium Chloride – Based Extraction Chromatography Resin (produced by Eichrom, Inc.)
TOPO	Trioctylphosphine Oxide
UTEVA	Diamyl Amylphosphonate – Based Extraction Chromatography Resin (produced by Eichrom, Inc.)
VAD	Variable Angle Degrader

TABLE OF CONTENTS

Page

LIST OF FIGURES

Page

LIST OF TABLES

Page

CHAPTER I

INTRODUCTION

Chemists have been probing the upper limits of the periodic table throughout the last century. The chemistry of the heaviest elements, transactinides (Z > 104), is particularly interesting due to relativistic effects [1]. This dissertation focuses on establishing the foundation necessary to study the chemistry of transactinides. There are two distinct projects discussed in this dissertation: (1) commissioning of a gas stopper to thermalize accelerator-produced elements and (2) offline development of a chemical system to study rutherfordium (Rf) using homologs. As background for the new experimental set-up, this chapter will explore the following topics: First, Section 1.1 will discuss the production and properties of transactinides, particularly Rf, and how they affect both projects. Section 1.2 will focus on thermalization of accelerator-produced elements and the different types of gas stoppers that are used in these experiments. Next, Section 1.3 will discuss relativistic effects, and Section 1.4 will review previous studies of Rf chemistry.

1.1 Production and Properties of Transactinides

Transactinides are man-made elements produced by the fusion of two lighter elements. A particle accelerator is needed to overcome the Coulomb repulsion between the accelerated projectile ion and stationary target atom. The resulting nuclear reaction creates a compound nucleus with both intrinsic excitation energy and kinetic energy. The compound nucleus will de-excite by either fission (> 99% of the time) or particle evaporation. This reaction process is known as fusion-evaporation and produces evaporation residues (EVRs) (Figure 1-1) [2].

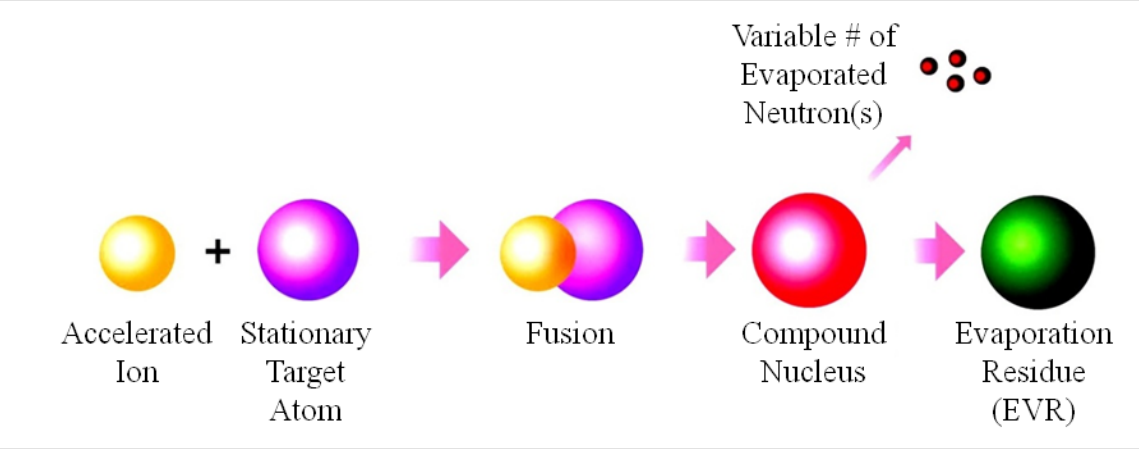

Figure 1-1. Fusion-evaporation reaction schematic.

1.1.1 Hot Versus Cold Fusion

Transactinide production reactions are generally grouped into two categories based on the excitation energy of the compound nucleus formed: cold fusion, where the excitation energy is typically 10-20 MeV, and hot fusion, where the excitation energy is

typically >30 MeV [2, 3]. The cross sections of these reactions are small (sub-microbarn) and decrease significantly with the atomic number of the EVR (Figure 1-2).

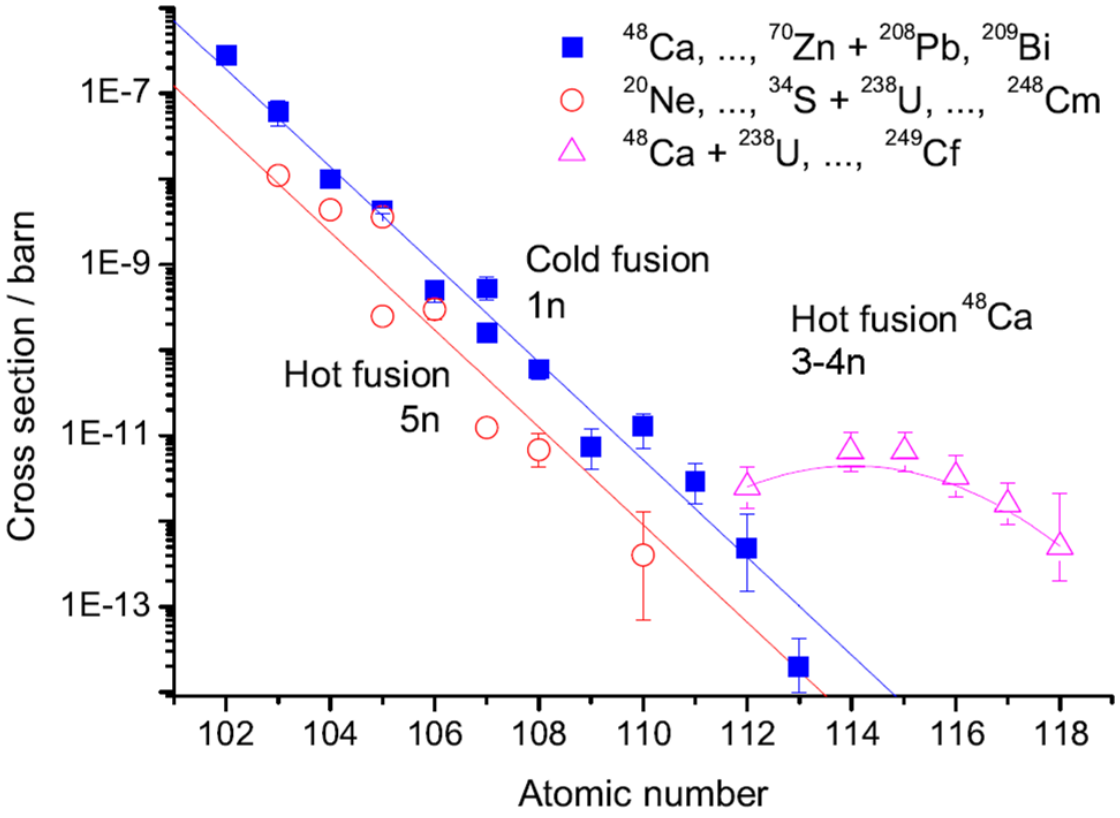

Figure 1-2. Experimental measured fusion evaporation reaction cross sections for various elements (Z > 102). Lines are to guide the eye. Adapted with permission from A. Türler and V. Pershina, Chem. Rev. **113**, 1237-1312 (2013). Copyright 2013 American Chemical Society.

In practice, cold fusion reactions occur between a ^{204,206,207,208}Pb or ^{209}Bi target and an accelerated medium-mass ion (predominantly ^{48}Ca or heavier). The particle beam energy is at or slightly below the Coulomb barrier. Due to the unusually negative Q-values of these reactions, the excitation energy of the compound nucleus is less than

20 MeV and only 1 to 2 neutrons are emitted. Hot fusion reactions occur between actinide targets and accelerated lighter ions (commonly ^{48}Ca or lighter). For this reaction type, the particle beam energy is above the Coulomb barrier, leaving the compound nucleus with relatively more excitation energy (30–60 MeV) and the ability to evaporate up to 6 (but typically 3–4) neutrons [2, 3]. Lighter transactinides have been produced by both cold and hot fusion (Figure 1-2). However, cold fusion reactions often have higher cross sections, while hot fusion reactions produce more neutron-rich transactinides with longer half-lives, making them useful for chemical studies [2]. Hot fusion reactions start having higher cross sections around Cn (element 112), and all transactinides heavier than element 113 have only been produced by hot fusion [2, 3].

The difference between the cross sections of hot and cold fusion reactions can be explained by taking a closer look at the factors that affect the production of EVRs (Eq. 1-1) [2].

$$\sigma_{EVR} = \sigma_{cap} P_{CN} W_{sur} \qquad \text{Eq. 1-1}$$

The cross section for a particular EVR reaction, σ_{EVR}, can be described by the product of the capture cross section, σ_{cap}, probability of complete fusion, P_{CN}, and the survival probability, W_{sur}. In simple terms, σ_{cap} is proportional to probability of the accelerated ion and target nucleus overcoming the Coulomb barrier and making contact. In the classical approximation, it is zero when the center-of-mass projectile energy is less than the Coulomb barrier, and increases with increasing energy until it saturates at approximately the geometrical cross section. For the reactions used to produce transactinides, it tends to vary slowly as the projectile and/or target are changed.

However this is not the case for P_{CN}. The probability of complete fusion is relatively constant (~10^{-2}) for hot fusion reactions [4], but decreases substantially for cold fusion reactions, ranging from ~0.1 for ^{48}Ca + ^{208}Pb to ~10^{-6} for ^{70}Zn + ^{208}Pb [5]. P_{CN} is hindered by quasifission; this is where the accelerated ion and target atom briefly interact ($t < 10^{-21}$ s), but ultimately re-separate. After the compound nucleus fully equilibrates it must de-excite. W_{sur} describes the probability that a particular compound nucleus will de-excite purely through particle evaporation. Each time a particle is emitted from the compound nucleus there is a high probability that it will instead fission; therefore, W_{sur} decreases as the excitation energy of the compound nucleus increases. This is more significant in hot fusion reactions which create compound nuclei with more excitation energy than cold fusion reactions [2, 3].

1.1.2 Discovery and Production of Rf (Element 104)

In 1964, a group of researchers led by G.N. Flerov at the Joint Institute for Nuclear Research in Dubna bombarded a ^{242}Pu target with a ^{22}Ne beam. They published results stating that they detected "activity" with a 300-ms-spontaneous-fission half-life and assigned it to ^{260}104 [6]. The Soviet group decided to name element 104 "kurchatovium" (Ku) in honor of Igor Kurchatov. Five years later, researchers led by A. Ghiorso at Lawrence Berkeley Laboratory tried to confirm the existence of the 300-ms half-life 104 isotope using the ^{246}Cm(^{18}O, 4n) and ^{248}Cm(^{16}O, 4n) reactions. However, they did not find any evidence supporting the Soviets' claim.

During the same year, this American group bombarded ^{249}Cf with a ^{12}C beam and detected alpha-decaying nuclei with a half-life of (4.5 ± 1) s. They determined that

the product of this reaction was ^{257}104 [6]. The mass and atomic number were confirmed by the detection of its daughter, ^{253}No, a well-studied alpha emitter. The Americans decided to name element 104 "rutherfordium" (Rf) in honor of Ernest Rutherford. Both names were widely used in literature for decades. The disagreement was finally resolved in 1997 at the 39th IUPAC General Assembly, where the two teams agreed to call element 104 "rutherfordium" and share the discovery claim [7].

Currently, 13 isotopes of Rf have been reported [2, 3, 6, 8-14]. They have been produced by two different methods: the fusion of two lighter nuclei (Table 1-1) or the decay of heavier elements. More neutron-rich isotopes of Rf have been produced via the decay of heavier elements. For example, ^{263}Rf ($t_{½}$= 15 min) is produced from the electron capture (3% branch) of ^{263}Db (element 105) [13, 15]; ^{265}Rf ($t_{½}$= 2.5 min) from the alpha decay of ^{269}Sg (element 106) [13, 16]; and ^{267}Rf ($t_{½}$= 1.3 h) from the alpha decay of ^{271}Sg [13, 17]. These relatively long-lived isotopes could be advantageous for the chemical study of Rf, but their production rates are significantly lower than lighter, directly produced Rf isotopes.

Table 1-1. Properties of known Rf isotopes. Rf isomers and isotopes produced by the decay of heavier elements have been omitted.

Isotope	Half life	Main Decay Mode	Experimental Measured Cross Section	Direct Production Reaction
^{253}Rf	48^{+17}_{-10} μs [8]	spontaneous fission	0.19 ± 0.05 nb [8]	^{204}Pb(^{50}Ti, n)
^{254}Rf	23 ± 3 μs [8]	spontaneous fission	2.4 ± 0.2 nb [8]	^{206}Pb(^{50}Ti, 2n)
^{255}Rf	1.6 s [2]	alpha decay & spontaneous fission	0.7 ± 0.5 nb [8]	^{208}Pb(^{50}Ti, 3n)
^{256}Rf	8 ms [2]	spontaneous fission	15.7 ± 0.2 nb [9]	^{208}Pb(^{50}Ti, 2n)
^{257}Rf	4.7 s [2]	alpha decay	40 ± 5 nb [9]	^{208}Pb(^{50}Ti, n)
^{258}Rf	13 ms [2]	spontaneous fission	10^{+10}_{-3}nb [10]	^{246}Cm(^{16}O, 4n)
^{259}Rf	2.8 s [2]	alpha decay	7 nb [10]	^{245}Cm(^{18}O, 4n)
^{260}Rf	21 ms [2]	spontaneous fission	14 ± 2 nb [10]	^{249}Bk(^{15}N, 4n)
^{261}Rf	75 ± 7 s [14]	alpha decay	12 ± 3 nb [12]	^{248}Cm(^{18}O, 5n)
^{262}Rf	2.1 s [2]	spontaneous fission	~0.7 nb [2]	^{244}Pu(^{22}Ne, 4n)

1.1.3 Decay Modes of Transactinides

The main decay modes for transactinides are alpha decay and spontaneous fission. Since transactinides are created by fusion-evaporation reactions, they are inherently neutron deficient. Thus, they are stable to beta-minus decay [6]. Although it is energetically possible for odd-mass transactinides (e.g., ^{263}Db) to decay by electron

capture, alpha decay and/or spontaneous fission are more favorable because they usually occur on a considerably shorter time scale. Both alpha decay and spontaneous fission are hindered in nuclei with an odd number of neutrons or protons [6]; these isotopes tend to have longer half-lives (making them useful for chemical studies). This difference in half-life is caused by the need to combine pairs of neutrons and protons from low-lying orbitals into an alpha particle with zero spin. If the neutron number is odd, then the daughter can be left in an excited state, reducing the decay energy and therefore the barrier tunneling probability. Evidence of this can be seen in Table 1-1, where Rf isotopes with an odd number of neutrons have half-lives longer than those with an even number of neutrons. Additionally, alpha decay is the dominant decay mode for ^{257,259,261}Rf (Table 1-1). This is the preferred mode of decay for chemical studies because direct confirmation is possible [2]. The energy signature of the alpha particle is unique to the parent nucleus and can be used to confirm the transactinide's presence.

1.1.4 Experimental Design Constraints for Chemical Studies of Transactinides

Since most transactinides have short half-lives and are produced in reactions with very low cross sections, designing an experiment to study the chemical behavior of these elements raises several challenges [2, 3, 18]. First, the newly formed transactinide's kinetic energy must be rapidly degraded from MeV to sub-eV energies. Second, the chemical system must operate on a time scale less than or comparable to the element's short half-life. Third, with current accelerator technology, transactinide production rates range from approximately one per minute to one per month, so the experiment must be repeated numerous times over many days [2, 3, 18]. Fourth, the chemical procedure

must be easily reproducible for the results to have statistical significance. Fifth, due to transactinides' short half-lives and low production rates, there will never be more than one atom in a system at any given time. This significantly limits the possible chemical reactions since polynuclear species will not form [2, 3, 18]. Therefore, transactinides must be studied on an "atom-at-a-time" basis. Sixth, samples resulting from the chemistry study must be prepared to be measured by nuclear spectroscopy. As previously discussed, alpha spectroscopy is preferred.

1.2 Thermalization of Nuclear Reaction Products

After a fusion-evaporation reaction, the EVRs produced have 30 to 50 MeV of kinetic energy from the transfer of momentum from the beam particle. The EVRs must be thermalized before their chemistry can be studied. Two different methods have been used to stop EVRs [2, 18]. One method uses a thick metal foil or block to catch the recoils directly downstream of the accelerator target. After the target is irradiated, the foil is retrieved and quickly dissolved in a solution to allow the chemical study of online-produced (accelerator-produced) nuclei [2, 18]. If a block is used, the first ~10 μm of the block are shaved off and dissolved. This method is efficient, but not timely. It takes several minutes to complete, so it does not work well with most transactinides, which have half-lives of a minute or less. However, it has been used to study the chemistry of long-lived ^{268}Db [19, 20]. Another method to thermalize EVRs uses a gas-filled (usually He, see section 1.2.3 for more details) chamber with a foil window acting as a pressure barrier. The window is located either directly behind the target or downstream of a physical separator (discussed in more detail in Section 1.2.2.1) [21-25]. This technique

is not as efficient, but is very fast and can operate continuously; some devices can transport EVRs to a chemistry experiment in less than a few seconds [2]. In this method, the kinetic energy degradation of the product concludes in a gas-filled chamber known as a thermalization chamber [21]. This is advantageous because most, if not all, of the recoils' stopped distribution can be contained in the gas. The device that was built and tested is based on this "thermalization chamber method" and will be the focus of this section.

1.2.1 Thermalization Chambers

The scientific community has many different names for thermalization chambers, such as gas stopper, gas catcher, gas cell, and recoil transfer chamber (RTC) [21, 24, 26-42]. Different variations of these devices are used to facilitate a wide range of experiments: chemical studies of EVRs [24-26], precision mass measurements using Penning traps or a multi-reflection time-of-flight spectrographs [31, 34], and post-accelerated radioactive beam production [33, 37, 42].

After the ions are thermalized in gas cells, different forces guide the ions through the device. Gas catchers commonly used in the transactinide field use the aerosol gas-jet technique [24-26]: EVRs stop in an aerosol-loaded gas, attach to an aerosol particle, and are then guided through a capillary to the experiment site by differential pumping of gases. Alternatively, several other gas cells [27-42] use an additional force: One or more electric fields are applied inside the device, which aides the gas flow in the focusing and transportation of the ions through the chamber.

1.2.2 Gas Stoppers: Aerosol Gas-Jet Technique

The aerosol gas-jet technique for the thermalization and transportation of accelerator-produced nuclei was first described by Wollnik *et al.* [21]. The experimental design is simple (Figure 1-3): Energetic reaction products recoil out of the target, pass through a thin metal foil to enter the thermalization chamber (containing 1–2 atm of He), and stop within the first few centimeters of the thermalization chamber. Here they attach to aerosol particles and are carried through a capillary to the collection chamber. The collection chamber is connected to a strong vacuum pump, which makes the pressure in the collection chamber only a few torr. At the end of the capillary, the gas velocity increases to approximately 90% of the speed of sound due to the pressure gradient between the thermalization and collection chambers [21]. Thus, the ion-aerosol clusters are "thrown" with substantial force onto the collector foil.

Using the aerosol gas-jet technique, Wollnik *et al.* consistently measured transportation efficiencies between 60% and 90% [21]. This was a significant improvement over aerosol-free gas-jet systems, which had average transportation efficiencies of approximately 10% to 20% [22, 23]. These measurements were called "transportation efficiencies" because they were determined offline using a radioactive source. At the time of Wollnik *et al.*'s experiments, online efficiency measurements were not possible [21].

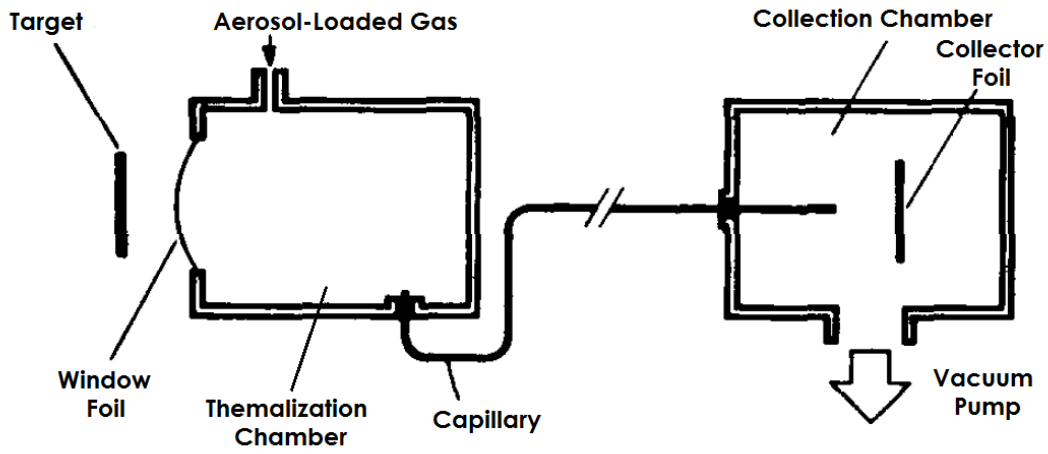

Figure 1-3. Schematic of an aerosol gas-jet system. See main text for more details. Figure from Nucl. Instr. Meth. [21].

1.2.2.1 Present Day Aerosol Gas-Jet Gas Cells

The aerosol gas-jet system described in Figure 1-3 has a number of limitations for the chemical investigation of transactinides [24]. First, only thermally stable gaseous molecules (oxides and halides) can be studied because the plasma created in the RTC by the intense heavy-ion beam destroys thermally unstable compounds (e.g., organometallic compounds). The EVRs can be transported away from the beam-created plasma using aerosols; however, the high temperature (> 800°C) needed to remove the aerosol particles from the gas phase makes the formation of thermally unstable compounds again impossible [24]. Second, there are a significant number of unwanted reaction products that interfere with the detection of the EVRs, thus limiting the possible chemical investigations. Third, the chemical system used to the study the transactinide's chemistry must also remove the unwanted reaction products. This chemical system

requires good selectivity between different groups in the periodic table; therefore, chemical differences between elements in the same group cannot be studied with great detail [24]. Fortunately, all these issues can be solved by using a physical separator upstream of the thermalization chamber (Figure 1-4).

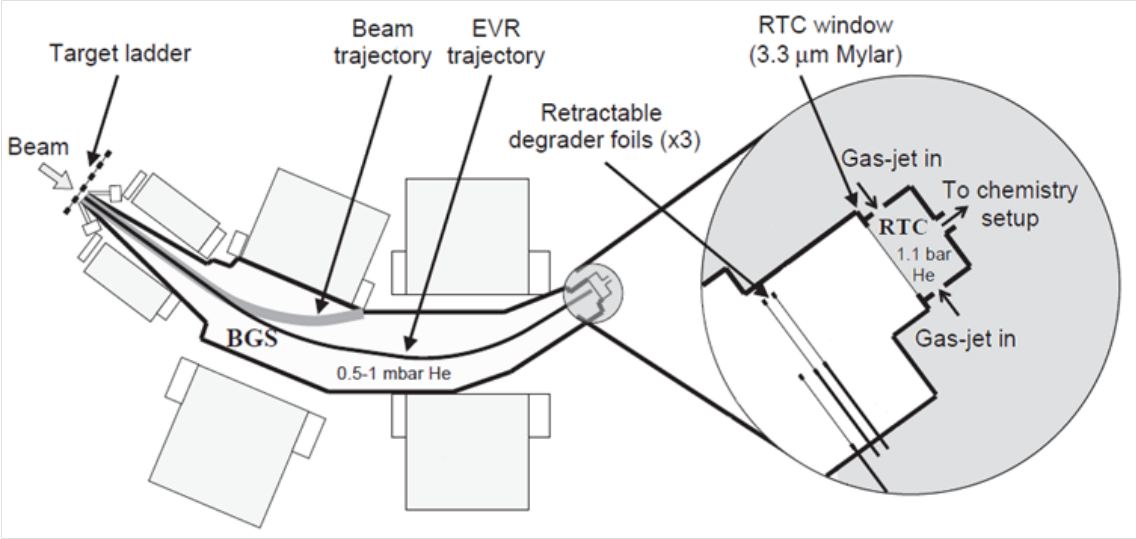

Figure 1-4. Schematic of the Berkeley Gas-filled Separator (BGS) with a RTC attached to its focal plane. Figure from Nucl. Instr. Meth. Phys. Res. A [24].

The concept of using physical preseparation to aid the chemical study of transactinides and their homologs was first applied at the University of California, Berkeley in the early 2000s [24]. Physical separators separate beam particles and unwanted reaction products from the EVRs based on differences in their magnetic rigidity, electric rigidity, and/or velocity. The Berkeley Gas-fill Separator (BGS) separates particles based on magnetic rigidity. As shown in Figure 1-4, the intense

heavy-ion beam trajectory is very different than the EVR trajectory due to the magnetic rigidity difference.

After physical separation, the EVRs lose kinetic energy by passing through the retractable degrader foils and the 3.3-μm Mylar RTC window (Figure 1-4). Depending on the kinematics of the fusion-evaporation reaction, more or fewer degrader foils are inserted. The final thermalization occurs in 1.1-bar He gas in the RTC [24]. Then a gas-jet (with or without aerosols) transports the EVRs to the chemistry setup.

Physical preseparation makes it possible for thermally unstable compounds to be added to He for gas phase studies; the volatile species are immediately carried to a thermochromatographic separator for analysis [24]. A thermochromatographic separator is a column with a decreasing temperature gradient; the volatility of a compound is quantified by the distance the molecule travels within the column before it adheres to the column walls [43]. A more volatile compound will travel further through the thermochromatographic separator. If the EVRs need to be transported through a capillary to a different chemistry experiment (i.e., liquid phase), aerosols are added to the He gas [24].

The disadvantage of using physical separators is that the rate of EVRs that enter the RTC is lower than if the gas cell was directly downstream of the target. This can be explained by both separator efficiency (~60% for BGS) and the use of a thin target (0.5 mg/cm^2 versus 1.5 mg/cm^2) decreasing EVR production rates. A thinner target is needed due to the momentum and angular acceptance of the BGS. Nevertheless, the chemical

investigations of transactinides made possible by physical separators outweigh this disadvantage [24].

A similar gas cell to the one used at Berkeley has been built at GSI Helmholtz Center for Heavy Ion Research (GSI) for use with the TransActinide Separator and Chemistry Apparatus (TASCA) [26]. This RTC has spacers that can be added to increase the depth of the device, which is useful depending on the width of the EVRs' stopped distribution. However, larger RTCs have increased transportation time of the EVRs, which is detrimental to transporting short-lived isotopes [26].

The most efficient RTC tested at GSI had a depth of 4 cm and a window size of 14 x 4 cm^2, which was expected to accept ~60% of the EVRs at the end of TASCA. The RTC window was made out of Mylar foil; the foil's thickness depended on the kinetic energy of the EVR being studied [26]. A honeycomb grid with ~80% geometrical transparency was used to help support the large force on the Mylar RTC window due to the pressure differential between the RTC and TASCA [26]. The pressure in the RTC was held at ~1 bar and KCl aerosol particles were carried by He gas through a 10-m capillary with an inner diameter of 2 mm. The device's efficiency was characterized by the reaction $^{nat}Ce(^{40}Ar, xn)^{175-177}Os$ [26]. In tests of this RTC, Even *et al.* measured an efficiency of 80 ± 8% with a gas flow rate greater than 3 L/min. This was the efficiency from directly behind the RTC window to end of the 10-m capillary. The transportation time for this device was calculated to be at least 7 to 8 s [26]. This transportation time was sufficient for the chemical study of elements with half-lives greater than 10 s, which is well within the half-life range of several transactinide isotopes.

1.2.3 Gas Stoppers: Electric Field Technique

The aerosol gas-jet technique cannot be used to study nuclides with half-lives on the order of milliseconds since transportation times are too long. An additional force is needed to transport these short-lived nuclides. To solve this issue, researchers use an electric field to rapidly transport ions through a gas cell. In many cases, efficiency is sacrificed for shorter transportation time. Two different types of electric field methods are used to guide the ions through the gas stopper: static electric field design [27-30] and RF ion-guide design [31-38]. The static electric field design uses a DC field that has a decreasing potential gradient. The RF ion-guide design uses an oscillating electric field, also known as radiofrequency (RF) field, superimposed on a DC field.

The electric fields in these devices can only guide the online-produced ions if they remain positively charged. Thermalization occurs when ions collide with gaseous atoms in the RTC. If the first ionization potential of the gas is higher than that of the ion, neutralization is improbable. Two gases have been considered, He and Ar. Ar has the advantage of higher stopping power than He due to its larger atomic radius and greater nuclear charge, thermalization will occur within fewer collisions. The stopped distribution of the products will be tighter in Ar than He. However, the ionization potential of Ar (15.8 eV) is significantly lower than He (24.6 eV). Neutralization of the online-produced ions is more probable in Ar. Therefore, He has been determined to be the optimum gas for these devices [32]. Ions can also be neutralized by forming molecules with contaminants. Aerosols cannot be used because, like contaminants, they

would neutralize the ions. To decrease the contaminate level in present-day gas cells, 99.999% pure He is used after further purification by a heated getter purifier [32].

Physical preseparation of the product of interest from unwanted reaction products and beam particles is critical to the effectiveness of the electric field in these devices [24]. Nuclear reaction byproducts would contaminate the He in the gas cell. Also the particle beam would ionize the He gas at a significantly higher rate than the product beam alone, making charge transfer between a He ion and an ion of interest more probable [32]. In addition, the ionized He would create a space charge that would hamper the electric field's effectiveness [44].

1.2.3.1 Static Electric Field Design

The RTC commissioned for this dissertation project was inspired by a gas cell used at the National Superconducting Cyclotron (NSCL) for the thermalization of projectile-fragmentation reaction products (Figure 1-5). The NSCL's device used a static electric field to guide thermalized ions [27-30].

Before the reaction products entered the gas cell, the A1900 fragment separator was used to select the projectile fragments of interest. Projectile fragments exited the separator with considerably more kinetic energy than fusion-evaporation EVRs (~100–150 MeV/*u* versus ~125–200 keV/*u*). Consequently, thicker degraders (mm versus μm) had to be used upstream of the gas cell. The experiment setup, described in [29], used a 1.5-mm-thick glass variable angle degrader (VAD), a 0.75-mm-thick glass wedge degrader, and a grounded 6.5-mm-thick beryllium gas cell window. Together, these

degraded the energy of ^{38}Ca and ^{37}K projectile fragments from 92 MeV/*u* to approximately 3 MeV/*u*.

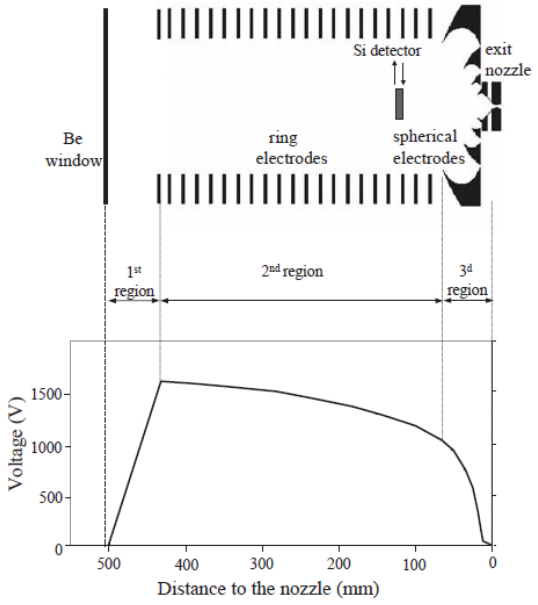

Figure 1-5. NSCL gas cell schematics. Top: schematic diagram of NSCL's gas cell. Bottom: voltage distribution on the gas cell electrodes. See the main text for a discussion. Figure from Nucl. Instr. Meth. Phys. Res. A [29].

After the ions passed through the Be window, they were thermalized in 760 torr of He. This 50-cm gas cell was longer than ones used for stopping EVRs to compensate for the larger width of projectile fragments' stopped distribution. Once the ions stopped, a decreasing potential gradient across the ring and spherical electrodes guided the ions toward the exit nozzle (Figure 1-5). The optimum voltage distribution was determined through simulations using SIMION (bottom of Figure 1-5) [29]. Figure 1-6 shows the expected equipotential lines determined by SIMION for the NSCL gas stopper. The Be

window was grounded, which caused a majority of the ions that stopped in the first ~100 mm of the device to be diverted to the walls of the gas cell [30]. After this region, the ring electrodes (also known as drift electrodes) with a decreasing potential pulled the ions through [29, 30]. Then the concentric spherical electrodes focused the ions into the exit nozzle. The exit nozzle, with a 0.6-mm inner diameter, separated the gas cell from an expansion chamber, which was held at a pressure of 0.2 torr. This large pressure differential (760 torr versus 0.2 torr) caused the gas to reach supersonic speed. Thus, gas flow became the dominant force pushing the ions through the exit nozzle.

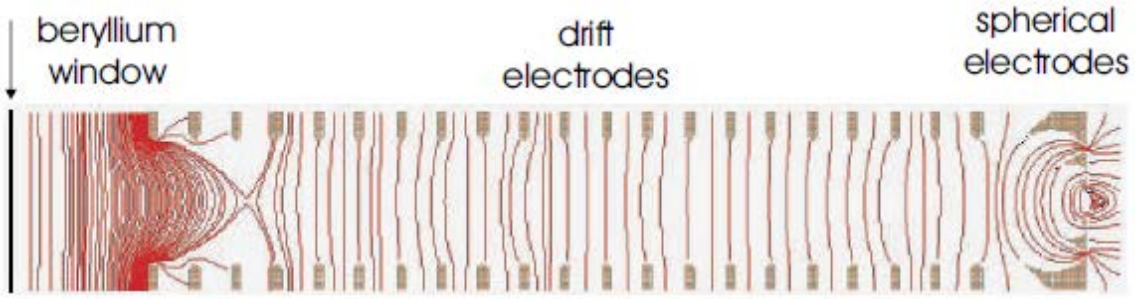

Figure 1-6. Equipotential lines of the NSCL gas stopper determined by SIMION. Ions travel perpendicular to equipotential lines. Figure from [30] used with permission from author.

In the NSCL's experimental setup, the stopped distribution of the 92 MeV/*u* ^{38}Ca and ^{37}K projectile fragments was too large to be contained by the gas cell [29, 30]. Since the VAD angle determined the location of the stopped distribution, changing the angle could maximize stopping efficiency, or the fraction of the stopped distribution that was stopped in the gas cell. The VAD effective thickness (and thus, stopped distribution

location) changed with the reciprocal of the cosine of the angle. If the angle of the degrader was too small, a majority of the ions would hit the rear of the gas cell; too large, a majority of the ions would stop in the Be window. A retractable silicon detector located 39 cm (Figure 1-5) from the RTC window was used to determine the gas cell's stopping efficiency at various angles [29, 30]. For the 92 MeV/*u* ^{38}Ca and ^{37}K projectile fragments, a maximum stopping efficiency of 50% was measured with the VAD set at ~29° (effective thickness = 1.715 mm) [29].

The extraction efficiency, also known as ion guide efficiency, is the fraction of ions that are transported through the exit nozzle after being stopped. For the 92-MeV/*u* ^{38}Ca and ^{37}K projectile fragments, a maximum ion guide efficiency of 7% was measured [29]. It was also discovered that most ions that stopped in the first 30 cm of the device were not affected by the electric field. However, an overall efficiency (product of both stopping and extraction efficiency) of a few percent was considered usable "to begin a broad experimental program with thermalized, rare-ion beams at the NSCL" [29].

1.2.3.2 Limitations of Static Electric Field Design

Two notable problems with static electric field designs are the limits on the shape and strength of the DC field [32, 37]. The first limitation is electrode shape. In the NSCL device, the decreasing potential gradient focuses the ions into the extraction nozzle due to the physical shape of the spherical electrodes. However, the focusing potential of electrode shape is limited—only a small number of shapes would create the curved equipotential lines shown in Figure 1-6 [30]. Substantial improvements are not possible by changing the shape of the electrodes with the static electric field design.

Second, the strength of the electric field is limited by the breakdown voltage of the He gas [32]. Arc discharge can occur between two electrodes in high electric field environments. The Paschen curve describes the threshold, also known as breakdown voltage, for this process: At the pressure of all RF gas cells (> 40 mbar), the breakdown voltage of He is proportional to the product of the distance between the two electrodes and the pressure of the gas between them. The breakdown voltage threshold for the NSCL device was approximately 200 V/cm. This phenomenon severely limits the possible potential gradients, which increases the extraction time and decreases the focusing ability of the device [32, 37].

A solution to these problems is adding an extra force, such as an RF field superimposed on a DC field, to help guide the ions into the extraction nozzle [32, 37]. The RF field repels the ions away from the electrodes (discussed in more detail below). Moreover, the focusing effect of the combined fields is due to the physical location of the electrodes, not their physical shape. Therefore, more options are available.

1.2.3.3 RF Ion-guide Design

There are many different variations of gas catchers that use DC and RF fields superimposed on each other. Most devices fall into three categories based on the configuration of the electrodes: RF walls [31-34, 38], RF funnels [32-34, 38], and RF carpets [35-37]. RF walls contain a series of cylindrical electrodes with constant diameter, like the drift electrodes in the NSCL gas cell [33]. RF funnels are very similar to RF walls except that the individual ring electrodes' diameters decrease as the ion

moves through the gas cell to the exit nozzle [34, 38]. RF carpets are a planar, two-dimensional version of RF funnels and can be used in their place [36, 37].

Most RF gas stoppers first use an RF wall or DC field ring system to steer the ions into an RF funnel or RF carpet, which then guides the ions into an extraction orifice [31-34, 36-38]. All RF configurations work based on the same principle: Along the length of the RF device, there is an overall decreasing DC potential gradient across the series of ring electrodes. The RF field is created by adjacent electrodes' voltages oscillating 180° out of phase from each other [38]. Similar to the DC field ring system, the decreasing potential gradient pulls the ions through the device by creating a force, F_{DC}. In tandem, the RF field creates a repulsive force, F_{RF}, which prevents contact between ions and electrodes. F_{RF} exists because adjacent electrodes' voltages oscillate at such a high frequency that the ions' trajectories are reversed before the ions can travel a fraction of the distance between neighboring electrodes [35]. Figure 1-7 shows how F_{DC} and F_{RF} combine to make the effective force, F_{eff}, which guides the ions to the end of the device. The decreasing diameter of the ring electrodes and their location in the RF funnel focuses the ions into the extraction nozzle. Please see the appendix for pictures and details of different RF devices.

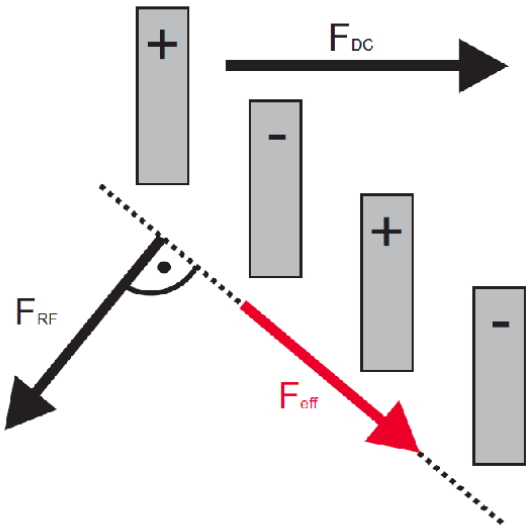

Figure 1-7. Schematic that shows how the forces created by the DC field (F_{DC}) and the RF field (F_{RF}) combine to make an effective force (F_{eff}), which focuses the ions to the end of the RF funnel . See text for more detail. Figure from Nucl. Instr. Meth. Phys. Res. B [38].

All of the designs discussed in this section—aerosol gas-jet, static electric field, and RF ion-guide—were considered when designing a new RTC for the chemical study of heavy elements. The aerosol gas-jet RTC designed at GSI by J. Evens *et al.* claims an extraction efficiency of ~80% [26], which is higher than most RF devices [31-38]. At Argonne National Laboratory an RF device has been built to thermalize EVRs which claims to have an extraction efficiency of 40-50% [32]. RF devices do have the benefit of faster extraction times, and the products exiting their extraction nozzles have a smaller emittance than those of aerosol gas-jet gas cells [31-38]. However, significant disadvantages of the RF ion-guide design are its complexity and cost (see appendix for

more details). Also, the new device does not require extraction times on the order of milliseconds since the nuclides of interest have half-lives on the order of tens of seconds. However, a system with a small emittance would be beneficial for next-generation transactinide experiments such as mass measurements [45]. For these reasons, the new RTC was based on the simpler static electric field design and included an optional secondary aerosol gas-jet chamber for EVR transportation through a capillary. The commissioning, simulation, design, fabrication, and testing, of this new RTC will be discussed in Chapter III.

1.3 Relativistic Effects

The chemical study of transactinides is of particular interest due to relativistic effects. These effects could lead to significantly different chemical and physical properties than predicted, perhaps even altering the periodicity of the elements. Transactinides are expected to exhibit the largest relativistic effects of all elements because the speed of the innermost electrons increases with atomic number. Pyykkö and Desclaux [1] showed how the 1*s* electrons' velocity, *v*, scales with *Z*:

$$v \approx \alpha Z c \qquad \text{Eq.1.2}$$

where α is the fine structure constant (≈1/137), *Z* is the proton number of the atom, and *c* is the speed of light. Einstein's relativistic mass equation illustrates how the mass of a particle (in this case, an electron) increases with velocity:

$$m_e = \frac{m_o}{\sqrt{1-\frac{v^2}{c^2}}} \qquad \text{Eq.1.3}$$

where m_o is the rest mass of the electron. This increase in the innermost electrons' mass, m_e, will cause the 1*s* orbital radius, *r*, to decrease according to the mass-dependent Bohr radius equation:

$$r = \frac{\hbar}{m_e \alpha c} \qquad \text{Eq.1.4}$$

where ħ is the reduced Planck's constant.

Using these three equations, it can be calculated that for Rf (Z=104), the 1*s* electrons' mass will increase by ~50% and the radius of the 1*s* orbital will decrease by ~50%. The 2*p* orbital will also contract; the $2p_{1/2}$ subshell will contract by about the same magnitude as the 1*s* orbital, while the $2p_{3/2}$ subshell will contract much less [1]. Due to orthogonality requirements, all higher-lying *s* and *p* orbitals will also contract and the *p* subshells will split. Consequently, the *d* and *f* orbitals will expand and destabilize because the contracted *s* and *p* orbitals will increase screening of the nuclear charge. Similar to the *p* orbitals, the *d* and *f* orbitals' subshells will be non-degenerate [1]. Overall, these disruptions in valence electron energies could affect the chemical and physical properties of the element. If the effects are large enough, it is possible that the ground state electronic configuration of the atom could change, possibly altering the periodicity of the heaviest elements [2, 3, 18].

Relativistic effects explain many chemical and physical properties of lighter elements. For instance, these effects cause the red-yellow color of Au [46] and the low melting temperature of Hg [47]. Additionally, relativistic destabilization of the 5*f* orbital impacts the stability of minor actinides' high oxidation states in solution [48].

Relativistic effects increase as Z^2. Therefore, an important question for nuclear chemists is, "How do relativistic effects influence the chemical and physical properties of the heaviest elements [2, 3, 18]?"

1.4 Chemistry of Rutherfordium

It has been predicted that the ground state electronic configuration of Rf is [Rn] $5f^{14}6d^{2}7s^{2}$ [49] and should behave chemically similar to its Group IV homolog Hf (ground state electronic configuration [Xe] $4f^{14}5d^{2}6s^{2}$). However, simple extrapolation of periodic table trends does not account for large relativistic effects that may affect the periodicity of the element. It has also been predicted that the relativistic stabilization of the $7p_{1/2}$ orbital may cause Rf's ground state electronic configuration to be [Rn] $5f^{14}7s^{2}7p_{1/2}{}^{2}$ and that Rf may behave chemically more like Pb (ground state electronic configuration [Xe] $4f^{14}5d^{10}6s^{2}6p^{2}$) [49]. If this is true, Rf would be significantly more volatile than Group IV elements since Pb is considerably more volatile than Hf. A thermochromatographic experiment with a quartz column was used to determine whether Rf behaved like a Group IV "d-element" or a "p-element" [50, 51]. The beginning of the column was held to room temperature and within the first ~5 cm the temperature inside the column increased to 1170°C. After another ~10 cm, the column cooled back to room temperature. An Ar-H_2 carrier gas mixture was used to carry the online-produced nuclides from the gas cell to the quartz column. Each element was studied separately. Solid-state track detectors on either end of the column would detect the decay of the online produced nuclide [50, 51]. Volatile "p-elements," such as Pb and Tl, passed through the column and were detected on the other side. Less volatile

"d-elements," such as Hf and Sc, did not pass through and were only detected at the beginning of the column. ^{259}Rf also did not pass through; none was detected on the other side of the column, but 65 spontaneous fission events were detected at the beginning of the column [50, 51]. This was evidence that Rf is not as volatile as "p-elements" and behaves more like other Group IV "d-elements."

Currently, there are no chemical studies demonstrating that Rf behaves differently than other Group IV elements. The present focus of the scientific community is to instead investigate the intergroup trends of Group IV elements (Ti, Zr, Hf, and Rf) to determine how relativistic effects influence Rf [2, 3, 18]. Periodic table trends dictate that Rf would behave more like Hf than Zr; however, this may not be the case due to relativistic effects.

Liquid chromatographic separations have frequently been used to determine complex formation trends of transactinides and their homologs [2, 3, 18]. Liquid chromatography contains two phases—stationary and mobile (liquid)—and separates mixture components based on their interactions with the two phases. This method was used to develop new chemical systems to study Rf that are discussed in this dissertation.

1.4.1 Complex Formation of Group IV Elements

A complex is a metal ion covalently bonded to ligands. The ligand can either be a negative ion (e.g., OH^-, Cl^- or NO_3^-), or a neutral molecule (e.g., H_2O) that possesses a lone pair of electrons. Complexes can be negatively charged (anionic), neutral, or positively charged (cationic). In a neutral solution, metal ions are hydrated, surrounded

by H_2O molecules. For Group IV elements, the predominate metal aquo complex is $[M(H_2O)_8]^{4+}$; for simplicity reasons, this is often written in reactions as M^{4+}.

In acidic, HA, environments, water molecules are replaced in sequential steps by the conjugate base, A^-. The overall reaction is the sum of the stepwise reactions:

$$M^{4+} + nA^- \leftrightarrow MA_n^{(4-n)+} \qquad \text{Eq. 1.5}$$

The number of conjugate base atoms, n, that will replace water molecules increases with the concentration of the acid. This changes the charge of the metal complex from cationic to neutral to anionic. However, another reaction occurs simultaneously: hydrolysis, the stepwise deprotonation of the H_2O molecules:

$$M(H_2O)_8^{4+} \leftrightarrow MOH(H_2O)_7^{3+} + H^+ \qquad \text{Eq. 1.6}$$

This reaction becomes more favorable as the solution's pH becomes less acidic. Group IV elements are known to undergo extensive hydrolysis in solution with pH greater than 0 [52, 53]. Hydrolyzed Group IV species have strong tendencies to sorb to surfaces. In general, hydrolyzed species are known to have different chemical behaviors than non-hydrolyzed species [52, 53]. Due to the competition between these two reactions (Eq. 1.5 and 1.6), a large number of different complexes can be present in solution at low acid concentrations. When studying the chemistry of any transactinide it is important to limit the number of complexes present in the solution, so it possible to deduce the complexation reaction taking place. Consequently, most liquid phase chemistry studies of Rf occur in acid concentration greater than 1.0 M ($pH \leq 0$).

1.4.2 Fundamentals of Transactinide Liquid Chromatography Experiments

Two specific types of liquid chromatography, ion-exchange and extraction, have been used to investigate complex formation trends of transactinides and their homologs [2, 3, 18]. It is important to note that, in these particular experiments, the columns are not used in the classical liquid chromatography mode where species are separated based on different migration rates through the column. Instead, the columns are used to determine uptake by the stationary phase. Both ion-exchange and extraction columns are used in the same fashion: They retain metal complexes based on their charge in the mobile phase.

The main difference between ion-exchange and extraction chromatography columns is the stationary phase [54, 55]. In an ion-exchange column, the stationary phase is a functionalized polymer (porous or gel) [54]. The functional group can be a negatively charged cationic-exchanger (such as a sulfonic acid) or positively charged anionic-exchanger (such as a quaternary ammonium). The stationary phase in an extraction column is an extractant molecule physisorbed to an inert support, usually porous silica or an organic polymer [55, 56]. The extractant could preferentially bind to cationic, neutral, or anionic species. Another important difference between the two chromatographic methods is that the kinetics of extraction chromatography is faster than ion-exchange chromatography [55], which is advantageous when considering the short half-lives of most transactinides.

With this type of experiment, the short half-lives of most transactinides make it necessary to use microcolumns, columns which have a free column volume (interstitial

space of the column) less than a few hundred microliters [2, 3, 18]. This is critical to the speed of the chemical system; if a larger column were used, the transactinide would spend more time in the column and the elution fractions would be larger. The elution fractions must be evaporated to dryness for alpha spectroscopy measurements, as this is the only method that can directly confirm the presence of a transactinide. The size of the elution fractions needs to be as small as possible to decrease the time necessary to evaporate the samples.

The mobile phase for these types of experiments is an aqueous solution and the charge that the metal complexes presents in solution varies with acid concentration, as previously discussed in Section 1.4.1. Thus, the column's retention of Group IV elements will change with acid concentration of the mobile phase. The mobile phase's acid concentration is changed to manipulate the charge of the metal complex. In most transactinide experiments of this type (results discussed in the next section), three different acid concentrations are used, which can be broadly characterized as:

- Solution A*: Acid concentration where the column is expected to retain 100% of all Group IV elements.
- Solution B: Acid concentration where there is difference in column retention of Group IV elements (i.e., separation).
- Solution C: Acid concentration where the column is expected to retain 0% of all Group IV elements.

*In some cases, Solutions A is not used.

A similar method is used with this type of experiment, which can be summarized as follows [2, 3, 18]: First, online-produced Zr, Hf, and Rf are transported from the gas cell by a He/KCl gas-jet system and collected on a Ta or Pt disk. The product collected is then dissolved in ~150 µL of Solution A, and the sample is loaded onto a microcolumn. The flow rate of the mobile phase is 1 mL/min. The effluent of Solution A is discarded. Then 200 to 300 µL of Solution B is sent through the column and the effluent is collected on a Ta disk—this is elution fraction 1. In cases where solution A is not used, the online-produced nuclides collected on the disk are dissolved by Solution B and the sample is loaded onto the microcolumn. The effluent is collected on a Ta disk—this is elution fraction 1. Then in both cases, any remaining Group IV elements are then eluted from the column using approximately 200 µL of Solution C. This effluent is also collected on a fresh Ta disk and considered elution fraction 2. Both elution fractions are then quickly evaporated to dryness for alpha/gamma spectroscopy measurement. This procedure is repeated hundreds of times. It is important to note that the presence of an online-produced isotope is unknown until the two elution fractions are analyzed [2, 3, 18]. For each specific element, a ratio of the total number of events detected in elution fraction 2 to the total number of events detected in elution fractions 1 and 2 is determined. These ratios can be used to deduce strength of complex formation trends between different elements.

This type of experiment can best be described as the “column version” of a liquid-liquid extraction. In liquid-liquid extraction there are two liquid phases: aqueous and organic [54]. The extractant is in the organic phase, while the metal complexes start

out in the aqueous phase. The two phases are mixed and then separated; depending on the affinity of the extractant for the metal complexes, more or less will move into the organic phase. The extractability of the metal complex is quantified as the percentage of metal ions extracted into the organic phase [54]. Both methods reveal the same information. However, extraction or ion-exchange chromatography is advantageous for transactinide chemistry since it is faster than liquid-liquid extraction and automatable. An automatable chemical system is beneficial for transactinides studies since it is more reproducible and can run continuously for multiple days (see Section 1.1.4) [2, 3, 18].

1.4.3 Liquid Chromatographic Studies of Rf

The first liquid-phase chemistry experiment of Rf conducted by Silva *et al.* had similar results as the gas-phase thermochromatographic experiment discussed at the beginning of section 1.4 [57]. Silva *et al.* studied the periodicity of Rf, but did not analyze the intergroup trends of Group IV elements. In this study, researchers used Dowex 50 x 12, a cation exchange resin column with a mobile phase containing a chelating agent, ammonium α-hydroxyisobutyrate (0.1 M, pH 4.0) to characterize the chemistry of Rf. In this experiment, the mobile phase did not change concentration. The researchers discovered that trace quantities of Zr and Hf were not retained by the column, but trivalent and divalent actinides remained on the column [57]. The retention of online-produced ^{261}Rf was also tested and— like Zr and Hf—it eluted from the column, evidence that Rf behaves like a Group IV element.

Nine years later, Hulet *et al.* studied the chloride complexation of Rf using an extraction chromatography column [58]. The stationary phase was an anionic extractor,

Aliquat-336 (a mixture of trioctyl and tridecyl methyl ammonium chlorides), physisorbed to a fluoro-carbon powder. The mobile phase was HCl. In this experiment, the mobile phase concentrations did change. Solutions A and B (elution fraction 1) both contained 12 M HCl; in this concentration, Group IV elements are expected to be present as an anionic chloride complex and there is no separation of Zr and Hf. Solution C (elution fraction 2) was 6 M HCl; in this concentration, Group IV elements tend to form neutral and cationic complexes and will not remain on an Aliquat-336 extraction column. Hulet *et al.* performed the experiment with online-produced Hf, Rf, Cm, Fm, and No. A majority of Hf and Rf events were detected in fraction 2, while a majority of Cm, Fm, and No events were detected in fraction 1 [58]. This was evidence that Rf formed anionic chloride complexes like Hf in 12 M HCl, but Cm, Fm, and No did not. Again, intergroup trends could not be studied, but this experiment reaffirmed that relativistic effects in Rf were not strong enough to alter its periodicity.

In the 1990s, researchers began using liquid phase chemical systems to investigate the intergroup trends of Rf and its homologs [59, 60]. Czerwinski *et al.* studied the extraction of Zr, Hf, and Rf by tributylphosphate (TBP) in a liquid-liquid extraction system [60]. In this experiment, the organic phase was 0.25 M TBP in benzene and the aqueous phase ranged from 8 to 12 M HCl. The researchers concluded that the extractability trend of TBP was Hf < Rf < Zr. This evidence suggested that relativistic effects were altering expected periodic trends. However, these experiments could not elucidate complex formation trends because two different complexation reactions occur in a neutral extractant system. First, the metal chloride complex forms,

and then a complex forms between the extractant molecule and the neutral metal chloride complex. These results were confirmed by a research group at GSI. They preformed TBP chromatographic studies of Rf and its homologs [61, 62]. In this experiment, the stationary phase was TBP physisorbed to Voltalef powder and the mobile phase was HCl. Again the extractability trend of TBP was determined to be Hf < Rf < Zr.

In 2002, researchers at RIKEN studied the anionic behavior of Rf in a chloride medium using microcolumns filled with MCI GEL CA08Y (an anionic-exchange resin) [63]. The research group used an automated system called AIDA (the **A**utomated **I**on-exchange separation apparatus coupled with the **D**etection system for **A**lpha spectroscopy). By studying the anion-exchange behavior of online-produced Zr, Hf, and Rf, the researchers concluded that the extractability trend Hf < Zr < Rf. The online results suggested that the strength of chloride complex formation was Hf < Zr < Rf. These results show evidence that relativistic effects may be altering the intergroup trends of Group IV elements. These results cannot be compared with the results from the TBP experiments because TBP in a neutral extractant while MCI GEL CA08Y is an anionic extractant. A similar experiment was also done in nitric medium. At high HNO_3 concentrations the Rf pseudohomologs Pu(IV) and Th(IV) formed anionic nitrate complexes, while Zr and Hf did not [63]. Rf was not retained by the anionic-exchange column in a nitric medium, suggesting once again that Rf behaves like a Group IV element.

In 2007, the same research group at RIKEN repeated the TBP chromatographic separation in chloride medium using AIDA and determined a TBP extractability trend of Rf ≈ Hf < Zr [64]. These results do not disagree with those from Czerwinski *et al*. and from GSI, though Haba *et al.* could not measure a TBP extractability difference between Rf and Hf. However, the RIKEN group inferred the complexation formation trends of Group IV elements with TBP under the assumption that the sequence of the chloride complexation is Hf < Zr < Rf (conclusion from [63]; see paragraph above for details). Haba *et al.* interpreted their TBP results as evidence that the Zr and Hf tetrachlorides form more stable TBP complexes than Rf [64].

Also at RIKEN, a similar experiment was performed using a different neutral extractant, trioctylphosphine oxide (TOPO), again in a chloride medium [65]. This time, researchers observed an extractability trend of Rf ≤ Hf < Zr. These results show a similar trend as Haba *et al.* work using TBP. There is evidence that the extractability of Rf by TOPO may be slightly lower than Hf which would be in disagreement with the TBP extractability trends (Hf < Rf < Zr) determined by Czerwinski *et al*. and GSI.

1.4.4 Offline Development of Chemical Systems for Rf

Before a new chemical system can be used to study Rf and its homologs online, it must be tested and optimized offline using long-lived homologs. This is the focus of Chapter II. Commercially available extraction chromatography resins, TEVA and UTEVA, from Eichrom Technologies (Lisle, Illinois, USA) in HCl, HNO_3, and H_2SO_4 media (six systems) were evaluated as possible candidates for studying the chemistry of Rf. The chloride systems could be used to possibly clarify the ambiguity in the previous

results [60-62, 64, 65]. The other systems were also studied because the chemical behavior of Rf in a pure nitric acid and sulfuric acid solution has been investigated only on a limited basis.

The TEVA resin is an aliphatic quaternary amine (Figure 1-8) physisorbed to an inert polymeric support. The extractant molecule is Aliquat-336, a mixture of trioctyl and tridecyl methyl ammonium chlorides [66]. TEVA extracts anionic species like the anionic-exchange resin used by Haba *et al*. However, the functional groups are in the liquid form, so the extractant can more easily interact with anionic complexes (separation capabilities may be enhanced) [66]. The UTEVA resin is a phosphonate compound physisorbed to an inert polymeric support (Figure 1-8). The extraction molecule is diamyl amylphosphonate, a neutral extractant [67]. As a phosphonate, UTEVA should have an extraction strength in between those of TBP and TOPO. In general, the extraction ability of organophosphorus compounds correlates to the number of carbon-phosphorus bonds in the molecule: phosphate < phosphonate < phosphinate < phosphine oxide [54].

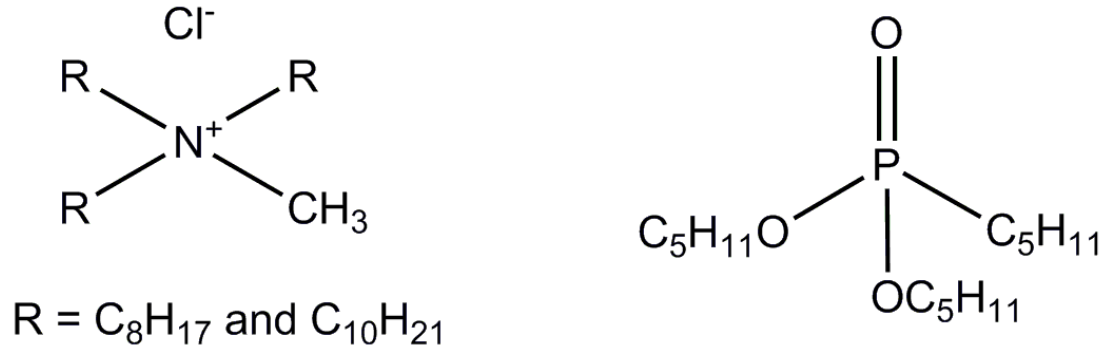

Figure 1-8. Structural formula of TEVA and UTEVA. Left: TEVA extractant molecule. Right: UTEVA extractant molecule.

The same method was used for all six systems to determine if they could be used for a future online study of Rf. First, a batch contact study for Zr and Hf in a wide range of acid concentrations (1.0 M to concentrated) was performed to determine the resin's extraction capabilities. These results were used to determine the acid concentration region where the resin's retention of Zr was significantly different than Hf. This acid concentration region was then tested for the column separation of Zr and Hf. Chapter II will discuss the experimental method, data analysis, and results from these experiments.

CHAPTER II*

OFFLINE DEVELOPMENT OF EXTRACTION CHROMATOGRAPHIC SYSTEMS FOR THE FUTURE STUDY OF RUTHERFORDIUM

The chromatographic separations by TEVA and UTEVA in HCl, HNO_3, and H_2SO_4 media were considered as possible systems for the future chemical study of Rf. New systems must be developed offline before they can be used to study accelerator-produced elements. The method, data analysis, and results of these experiments using long-lived radioisotopes of Zr and Hf will be the focus of this chapter.

2.1 Experimental Method

In offline experiments, tracer solutions of long-lived Rf homologs are used to mimic the "atom-at-a-time" nature of transactinide chemistry. Group IV elements are known to predominantly form mononuclear species at metal ion concentrations less than 10^{-4} M [52]. Therefore, carrier-free solutions of Zr and Hf were used to determine suitable experimental conditions to study Rf. In addition, the effects of hydrolysis were suppressed by only studying Group IV elements in acid concentrations greater than or equal to 1 M, limiting the number of different complexes present in solution (see section 1.4.1 for more details).

---

*Part of the data reported in this chapter is reprinted with permission from M. C. Alfonso *et al.*, J. Radioanl. Nucl. Chem., **307**, 1529-1536 (2016), ©2016 Springer

2.1.1 Materials

TEVA and UTEVA in the free resin form (50–150 μm particle size) were purchased from Eichrom Technologies. Prepackaged 2-ml dry pack cartridges of both TEVA and UTEVA resin (50–100 μm particle size) were also purchased from Eichrom Technologies. Standardized acids of HCl, HNO_3 and H_2SO_4, spanning a wide concentration range (1.0 M to concentrated), were made from reagent-grade acids purchased from VWR International (used without further purification) and de-ionized water (18 MΩ cm).

2.1.1.1 Tracer Solution

Carrier-free solutions of the radionuclides ^{88,89}Zr and ^{175}Hf were used (Table 2-1). ^{89}Zr in a 1.0 M oxalic acid solution was purchased from PerkinElmer (Waltham, Massachusetts, USA). A small amount of ^{88}Zr (< 0.5% of total activity) was present in the sample. The ^{88,89}Zr oxalate was converted to the chloride form by adding 2 ml of $La(NO_3)_3$ carrier solution (10 mg/ml) and 2 ml of 10% NH_4OH solution to the sample, causing the ^{88,89}Zr to coprecipitate with $La(OH)_3$. The solution was centrifuged and the supernatant was removed. The precipitate containing ^{88,89}Zr was then dissolved in concentrated HCl, completing the chloride conversion. Then the ^{88,89}Zr was isolated from the La carrier using a Dowex 1 X 8 anion-exchange column according to the procedure in [68]. The dissolved precipitate was loaded onto the column, concentrated HCl was passed through the column to remove impurities, and then the ^{88,89}Zr was eluted using 2 M HCl. The ^{88,89}Zr was stored in a 2 M HCl solution in a glass bottle.

^{175}Hf was produced via the ^{nat}Lu(p, x)^{175}Hf reaction at the Center for Accelerator Mass Spectrometry at Lawrence Livermore National Laboratory (LLNL). The excitation function of this reaction was studied at the Cyclotron Institute; details and results of this study are presented in [69]. A maximum cross section of 128 ± 14 mb was measured at a proton energy of 10.6 MeV. After irradiation, the ^{nat}Lu target (99.9%, <10 ppm ^{nat}Hf) was dissolved in concentrated HCl at 40 to 50°C for approximately 30 min. The solution was allowed to cool, causing most of the ^{nat}Lu to precipitate out of solution. The sample was immediately centrifuged, and the supernatant containing the majority of the ^{175}Hf was removed (and confirmed by gamma spectrometry). The ^{175}Hf solution was then purified using the same method described above for ^{88,89}Zr. The ^{175}Hf was also stored in a 2 M HCl solution in a glass bottle.

Table 2-1. Properties of radionuclides used in this work [70].

Isotope	Half-life, Days	Decay Mode (Branching Ratio, %)	Prominent Gamma-ray Energy, keV (Absolute Intensity, %)	Theoretical Maximum Specific Activity Ci/μmol
^{88}Zr	64.0	electron capture (100)	392.9 (97)	2.04
^{89}Zr	3.27	electron capture (77) positron emission (23)	909.0 (99)	39.0
^{175}Hf	70.0	electron capture (100)	343.3 (84)	1.87

2.1.2 Batch Study Procedure

Before the experiments, samples were prepared by transferring 1.0 ml of the stock solution into a 12 x 55 mm polypropylene (PP) vial. The samples were evaporated

to dryness in a heated water bath under a stream of compressed air and then reconstituted with 1.0 ml of the acid concentration of interest. It was discovered that a variable amount of activity stayed sorbed to the PP vial depending on the acid concentration used to reconstitute the sample. This was due to the heat used to evaporate the sample to dryness. To eliminate this source of activity lose the samples were transferred to fresh PP vial before the initial activity was measured.

After the initial activity of each sample was measured, the Zr and Hf uptake by TEVA and UTEVA in varying acid concentrations was tested. The method used was based on standard procedures to measure resin extraction capabilities [66, 67, 71]. All batch studies were performed at room temperature. First, 10 to 20 mg of the resin of interest was weighed into each sample vial. The amount of resin used in each sample was recorded. Then all samples were mixed by a shaker for one hour. Afterwards the slurry was filtered using a 0.45-μm (pore size) polytetrafluoroethylene 25-mm-diameter syringe tip filter. It was discovered that the filter paper absorbed a variable amount of the solution depending on the acid concentration of the sample. To correct for this effect, a volumetric pipette was used to acquire a measured aliquot, typically 50% to 65% of the original sample. The sample was transferred to a fresh PP vial, and then water was added to maintain the same 1.0 ml counting geometry as the initial count. The final activity of the samples was measured to determine the amount of Zr or Hf that had been extracted by the resin. The final activity measured was normalized to the size of the aliquot counted to correct for activity loss due to absorption by the filter paper.

The extraction capabilities of TEVA and UTEVA resin were studied in all 3 acid media (HCl, HNO_3 and H_2SO_4) using the method described above. Each acid concentration was tested in triplicate.

2.1.2.1 Activity Balance

Activity balance can be an obstacle with this type of batch study since only the aqueous phase is counted. During these studies, it is assumed that any activity loss is due to resin extraction. The two corrections applied, transferring the sample to a fresh PP vial before the initial activity was measured and normalizing the measured final activity to the aliquot size of the filtered solution counted, were sufficient to account for all sources of activity loss. If all the other sources of activity loss are not accounted for, resin uptake of 0% cannot be accurately measured. Resin uptake for both Zr and Hf of 0% were measured repeatedly for both TEVA and UTEVA in all systems in a wide range of acid concentrations, evidence that activity balance had been accomplished for the work presented in this chapter.

Figure 2-1 shows recovery for individual samples where the resin did not extract any of the radioisotopes of interest: The weighted average was 100% with a 1σ confidence interval of ±3%. This confidence interval was used as the absolute error in the fraction of activity that the resin extracted for all other resin uptake measurements. All batch study results are shown in Section 2.2.

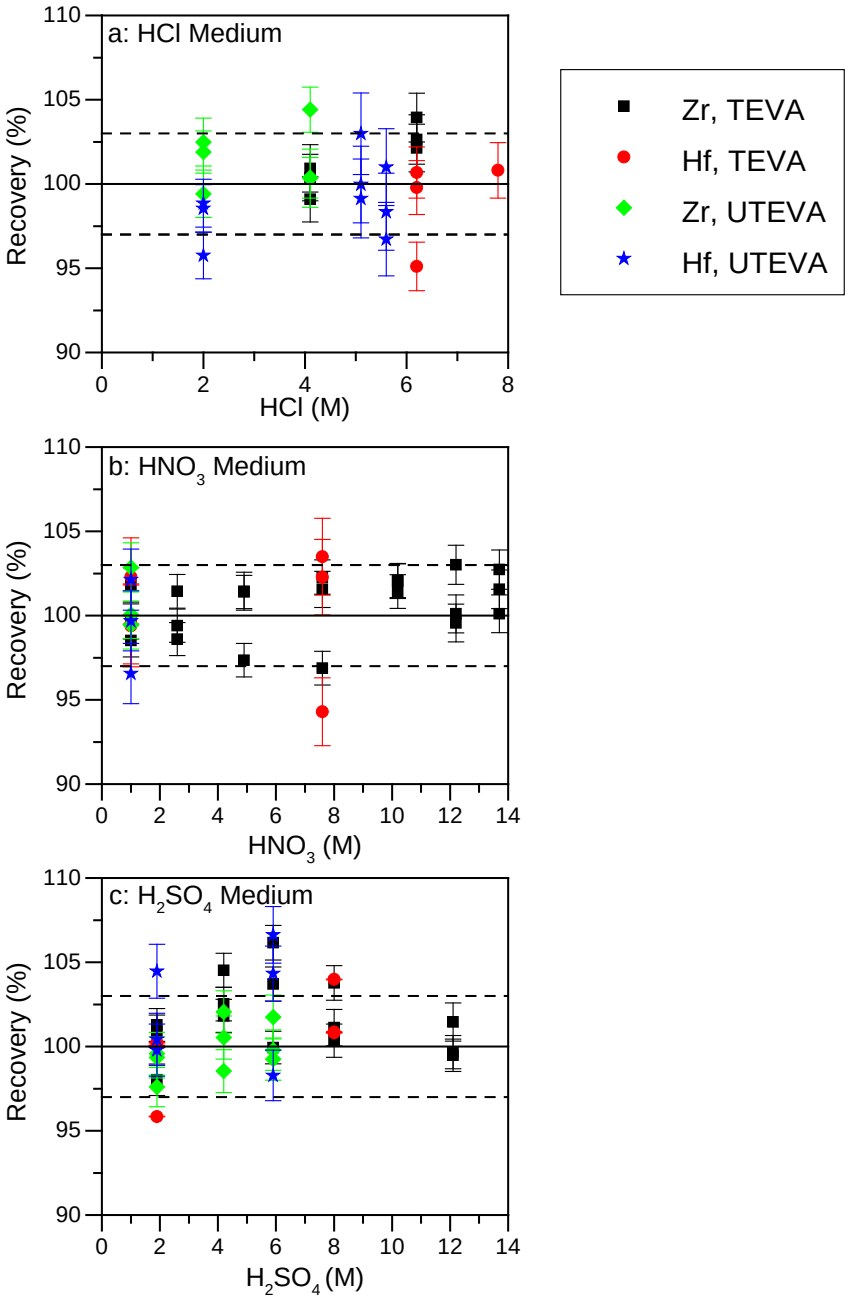

Figure 2-1. Recovery as a function of acid concentration for samples where TEVA and/or UTEVA had no affinity for Zr and/or Hf. HCl (top, a), HNO_3 (middle, b), and H_2SO_4 (bottom, c). The global average across all studies with both radionuclides was 100 ± 3%. The solid line represents the weighted average value, and the dashed lines represent the 1σ confidence interval.

2.1.3 Column Study Procedure

Extraction chromatography was performed using prepackaged 2-ml dry pack cartridges of TEVA or UTEVA resin (50–100 μm particle size). These cartridges had a free column volume 65% to 68% (1.3–1.4 ml) of the bed volume [66, 67]. The load samples were prepared and measured for initial activity using the same method described for batch studies. A vacuum box purchased from Eichrom Technologies was used to control the eluent flow rate to 1.0 ml/min, per recommendation of Eichrom.

All column studies were performed at room temperature. The column was conditioned by running 10.0 ml of the same acid concentration as the load solution through the column. Then the 1.0-ml load sample was loaded onto the column. Due to the free column volume size, the elution profile was determined using 1.0-ml fractions. The first fraction in the elution profile was the load sample. The subsequent five fractions were the same acid concentration as the load sample; the objective was to have only one of the radionuclides, Zr or Hf, elute from the column completely. Then, six fractions of an acid concentration where the resin did not retain either Zr or Hf were collected to elute any remaining radionuclides. The 12 individual fractions were collected in PP vials and counted to determine the elution profile for Zr and Hf. All column study conditions were tested in triplicate.

The acid concentration of the load sample and subsequent five fractions were chosen based on batch study results where the resin's retention of Zr was significantly different than Hf. The resin's extraction capabilities were quantified as the capacity factor, *k'*, for both Zr and Hf in the various acid concentrations (more details on this

calculation are presented in Section 2.2). The capacity factor refers to the number of free column volumes needed to pass through a column to reach the maximum of the elution curve (50% of the element of interest as eluted off the column). A ratio of two elements' *k'* is used to quantify how well they can be separated by a column; this is known as the separation factor. Fractions 1-6 were chosen based on batch study results; it had the acid concentration where the maximum separation factor was measured while one of the radioisotopes' *k'* was small (< 5). This maximized the probability that either Zr or Hf would elute completely within the first six fractions.

2.1.4 Activity Measurements

A PerkinElmer Wizard^2 2480 Automatic Well-Type NaI Gamma Counter was used to assay a majority of the samples. This detector was chosen because of its automated sample changer and high detection efficiency [72]. The sample vials are counted inside of a well that has been built into the 80 mm high x 75 mm diameter cylindrical NaI crystal. The crystal has a nearly 4π counting geometry and is surrounded by 50 mm of Pb shielding above and below [72]. The individual radionuclides had to be studied separately due to the large specific activity differences between ^{89}Zr and ^{175}Hf (Table 2-1). The required count time for the ^{89}Zr samples was considerably shorter (10–30 min) than the ^{175}Hf samples (1–6 h) with comparable metal ion concentrations (≤100 fM, excluding stable metal ion concentration). Also, Compton scattering of 909-keV gamma-rays from the decay of ^{89}Zr would interfere with the detection of 343-keV gamma rays coming from the decay of ^{175}Hf [70].

Sample spectra from the PerkinElmer Wizard^2 2480 Automatic Well-Type NaI Gamma Counter for both ^{89}Zr and ^{175}Hf are shown in Figure 2-2. The spectrum for ^{89}Zr (top of Figure 2-2) was expected; this radionuclide decays by two modes (Table 2-1): positron emission and electron capture [70]. The low energy peak (10–20 keV) is from Y x-rays due to the electronic transition (outer shell to K-shell) that occurs after electron capture [70]. The peak centered at 511 keV is due to positron annihilation, and the peak centered at 909 keV is the photopeak of the prominent gamma-ray transition expected from the decay of ^{89}Zr (Table 2-1) [70]. This sample of ^{89}Zr was active enough that the effects of Compton scattering of the 909-keV gamma-rays (i.e., the Compton Edge [~710 keV] and Backscattering Peak [~199 keV]) could be seen in the spectrum. The absolute detection efficiency for ^{89}Zr was determined to be approximately 13% (gating on the peak centered at 909 keV) for the counting geometry of a 1.0 ml filled PP vial.

However, the ^{175}Hf spectrum (bottom of Figure 2-2) was not expected. Since this radioisotope only decays by electron capture, a 511-keV positron annihilation peak was not observed [70]. Again the low energy peaks (50–60 keV) represented Lu x-rays caused by the electronic transition that occurred after electron capture, and the peak centered at 343 keV was the photopeak of the prominent gamma-ray transition expected from the decay of ^{175}Hf (Table 2-1) [70, 73]. The peak centered at ~400 keV was unexpected and was more intense than the 343-keV peak. It was discovered that this was an artifact of a very efficient detector [74]. When ^{175}Hf decays, both a Lu x-ray and the gamma-ray transition occur at practically the same time, and this peak at ~400 keV was the true coincident sum peak of the two photons. The true coincident sum peak was

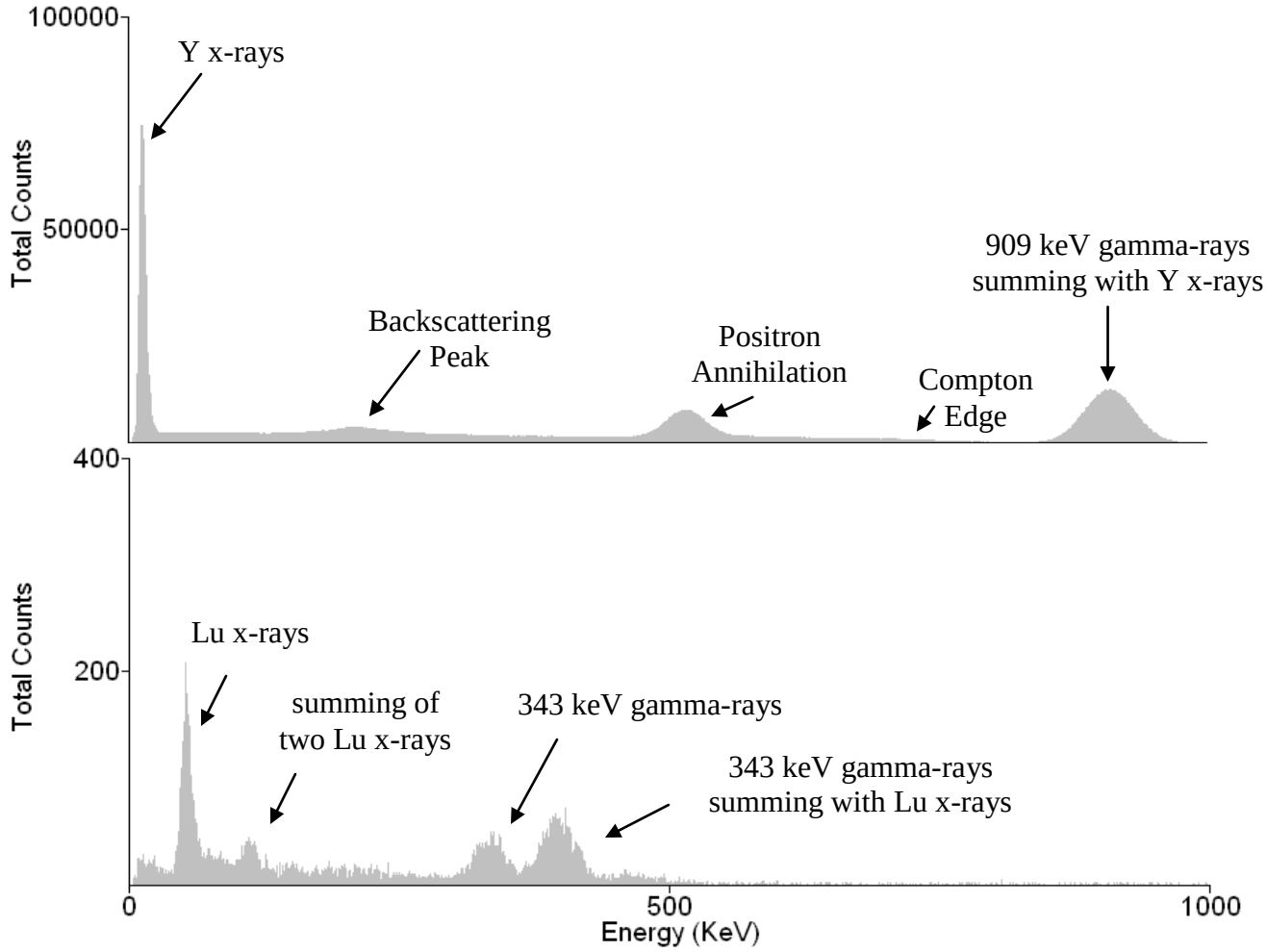

Figure 2-2. Sample spectra from the PerkinElmer Wizard[2] 2480 Automatic Well-Type NaI Gamma Counter. ^{89}Zr spectrum (top) and ^{175}Hf spectrum (bottom). Features of the spectra have been identified; see text for a detailed discussion.

larger than the 343-keV photopeak peak because the PerkinElmer Wizard^2 2480 Automatic Well-Type NaI Gamma Counter has an absolute detection efficiency more than 50% in the 50 to 60 keV region [72]. This effect also occurred when positron emission and electron capture [70]. The low energy peak (10–20 keV) is from Y x-rays due to the electronic transition (outer shell to K-shell) that occurs after electron capture [70]. The peak centered at 511 keV is due to positron annihilation, and the peak centered at 909 keV is the photopeak of the prominent gamma-ray transition expected from the decay of ^{89}Zr (Table 2-1) [70]. This sample of ^{89}Zr was active enough that the effects of Compton scattering of the 909-keV gamma-rays (i.e., the Compton Edge [~710 keV] and Backscattering Peak [~199 keV]) could be seen in the spectrum. The absolute detection efficiency for ^{89}Zr was determined to be approximately 13% (gating on the peak centered at 909 keV) for the counting geometry of a 1.0 ml filled PP vial.

Mixed radionuclides column studies using ^{88}Zr and ^{175}Hf together were performed to confirm the promising results obtained when studying the radioisotopes separately. ^{88}Zr was used instead of ^{89}Zr due to its lower specific activity (Table 2-1) [70]. A high-purity Ge (HPGe) detector, model number GC4018 (40% relative efficiency) made by Canberra Industries, Inc. (Meriden, Connecticut, USA), was used to assay samples that contained both radionuclides. A detector with greater resolution was needed because of spectral interference between the prominent gamma lines of ^{88}Zr and ^{175}Hf (Table 2-1). The Genie2000 Interactive Peak Fit software (Canberra Industries, Inc.) was used to analyze the spectra. True coincident summing of the gamma-ray and x-ray was not an issue, since the HPGe detector has a low absolute detection efficiency

(< 5%) for Y and Lu x-rays. After the mixed radionuclides column studies, the count times for the individual fractions varied depending on the amount of activity present. The absolute detection efficiency for a 1.0 ml filled PP vial was determined to be 6% to 7.5% in the energy region of interest.

The absolute detection efficiency quoted in this section were determined by first calibrating the absolute detection efficiency of the HPGe detector using a NIST traceable ^{152}Eu liquid standard with a comparable counting geometry of a 1.0 ml filled PP vial. ^{152}Eu is commonly used because it has many gamma lines with a wide range of energies. The NaI detector could not be calibrated using the NIST traceable ^{152}Eu liquid standard because the lines will not be resolved. Instead the calibrated HPGe was used to determine the activity of a 1.0 ml filled PP vial sample of ^{89}Zr. Then the same sample was counted on the NaI detector and the absolute detection efficiency for the particular isotope was calculated. This was repeated for a 1.0 ml filled PP vial sample of ^{175}Hf.

2.2 Data Analysis

The data from the batch study was used to quantify how well TEVA or UTEVA extracted Zr and Hf in a wide range of acid concentrations for HCl, HNO_3, and H_2SO_4 using the capacity factor, *k'*. Before *k'* could be determined, the weighted distribution coefficient, D_w, in ml/g was calculated using the following equation [66, 67, 71]:

$$D_w = \frac{(A_o - A_s)/W}{A_s/V} \qquad \text{Eq. 2.1}$$

where A_o is the initial activity of the sample and A_s is the final activity of the sample after the sample has interacted with the resin, the difference is the amount of activity the

resin retained. The initial and final activities must be decay-corrected to the same time (when resin interacted with the radioisotope). W is the mass of the resin in grams and V is the volume of the sample in milliliters. D_w can be converted to capacity factor, k', by dividing D_w by the "resin factor" for the individual resins [66, 67, 71]: The TEVA and UTEVA resin factors are 1.9 and 1.7, respectively [66, 67, 71].

The batch study k' results discussed below were weighted averages of the replicates. For the individual k' measurements, the uncertainty due to counting statistics was negligible. However, the absolute error in the fraction of activity the resin extracted was determined to be 3% (see Section 2.1.2.1) and was applied to the individual k' measurements. The uncertainty of the k' weighted average was the larger of either the propagated weighted error or the standard deviation of the batch study replicates. The dynamic range of the batch study was approximately 1.7% to 98.3% activity uptake by resin, which corresponds to a k' of approximately 0.8 to 2000.

The column study data analysis to determine the elution profile was considerably simpler. For each of the 12 individual fractions, the fraction of activity eluted was determined as the ratio between activity measured in the collected fraction and activity measured in the load sample. The elution profiles shown in this work were an average of the column study replicates. The error due to counting statistics was negligible. Therefore, the uncertainty given for an average elution profile was the standard deviation of the column study replicates. The minimum fraction of activity eluted that could accurately be measured was determined according to the "minimum detectable activity"

equation found in [75]. Equation 2.2 determines the smallest amount of activity that can be accurately detected above background within a 95% confidence interval:

$$MDA = \frac{2.71+3.29\sqrt{R_b t_s(1+t_s/t_b)}}{t_s E} \quad \text{Eq. 2.2}$$

where *MDA* is the minimum detectable activity, R_b is the background count rate, t_s is the sample count time, t_b is the background count time, and E is the detector efficiency for the radioisotope of interest.

2.3 Results

2.3.1 TEVA Batch Studies

The results from the TEVA batch studies are shown in Figure 2-3. Both the measured extraction and *k'* are shown to depict how the two values correlate with each other. The batch study results were used to determine which acid concentration region to focus on for the column separation of Zr and Hf.

The TEVA batch study results in an HCl medium were as expected (top of Figure 2-3). Samples with HCl concentrations below 6.0 M did not show any resin uptake ($k' < 1$) of both Zr and Hf. This was not surprising since Zr and Hf tend to form cationic and neutral species in that HCl concentration region [76]. An extraction of ~10% for Zr by TEVA was measured at 7.8 M HCl (top of Figure 2-3), while Hf stayed completely in solution. This was evidence that Zr formed anionic species more readily than Hf, which is in agreement with Haba *et al.*'s work using the anion-exchange resin CA08Y [63]. The batch study results showed that TEVA's affinity for both Zr and Hf

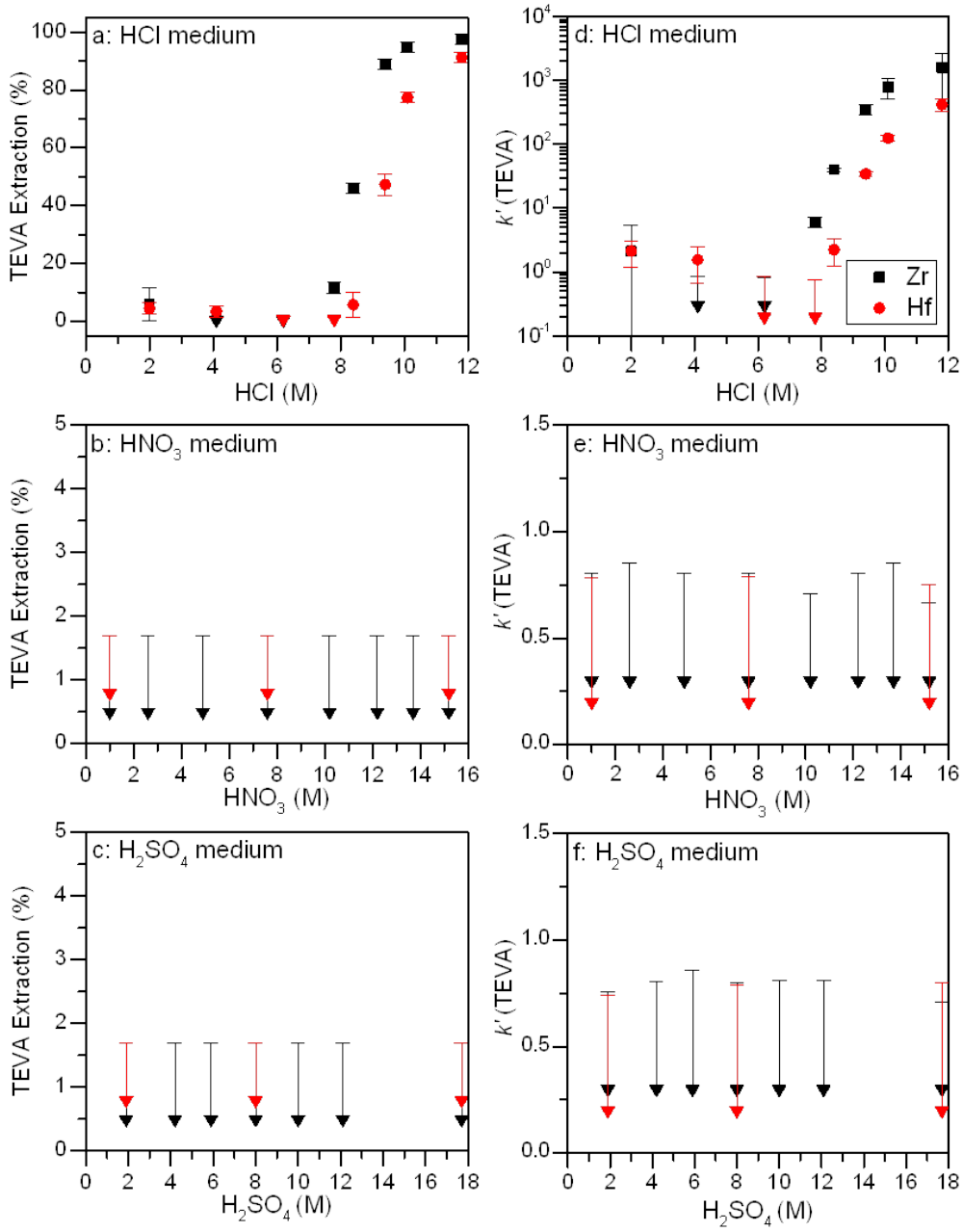

Figure 2-3. Measured extraction (%) and *k'* for ^{89}Zr and ^{175}Hf as a function of acid concentration in batch studies with TEVA. HCl (top, a and d), HNO_3 (middle, b and e), and H_2SO_4 (bottom, c and f). Downward and upward arrows indicate upper limits and lower limits, respectively.

increased with HCl concentration (> 7.8 M). This occurs because as the HCl concentration increased, the complexation reaction with the chloride ions increasingly favored the formation of anionic species (MCl_5^- and MCl_6^{2-}, M = Zr, Hf). A maximum separation factor, 18 ± 8, was measured in 8.4 M HCl; this concentration region was studied for viability in column separations (see the discussion in Section 2.3.2). The TEVA separation of Zr and Hf in an HCl medium was possible because Zr formed anionic species more readily than Hf.

The batch study results of TEVA in both HNO_3 and H_2SO_4 media were not promising for the separation of Zr and Hf (Figure 2-3). TEVA did not show any affinity ($k' < 1$) for either Zr or Hf in any of the concentrations studied (1.0–15.2 M HNO_3 and 1.9–17.7 M H_2SO_4). This agrees with Haba *et al.*'s work where CA08Y showed no affinity for Group IV elements in a wide range of HNO_3 concentrations [63]. The anion exchange adsorption of Group IV elements from a nitric acid medium was also studied using Dowex 1 [77] and little to no adsorption was measured. Dowex 1 and CA08Y also were shown not to have affinity for Zr and Hf in a wide range of H_2SO_4 concentrations (0.1 M–10 M) [78, 79], which supported the H_2SO_4 batch study results with TEVA. However, it is also possible that TEVA could not extract Zr and Hf in a H_2SO_4 due to competing sorption of sulfate ions [80]. Based on the results from the batch studies, neither of these systems were considered for column studies. Information about the intergroup trend of Zr, Hf, and Rf could not be gained from these systems since there was no resin uptake and no separation between Rf homologs.

2.3.2 TEVA Column Studies

The highest separation factor in an HCl medium, 18 ± 8, was measured in 8.4 M HCl for the TEVA resin. The TEVA column separation of Zr and Hf was studied in 7.8 M, 8.1 M, and 8.4 M HCl (Figure 2-4). It was anticipated that Hf would completely elute off the column within the first six fractions. Then six fractions of 4.1 M HCl were used to remove any remaining radionuclides; at this acid concentration, *k'* of less than 0.9 and 1.6 ± 0.9 were measured for Zr and Hf, respectively. The increase in *k*' with HCl concentration is depicted by the elution curves shown in Figure 2-4.

The TEVA column study results showed that in 7.8 M HCl, *k'* for Hf is less than 1 and Hf eluted off the column within a few fractions. However, the Zr/Hf separation factor was not large enough and, at this acid concentration, the *k'* for Zr was too small, such that within six fractions a significant amount of Zr (~39%) eluted off the column. At 8.1 M HCl, the *k'* for Hf increased, which can be seen in the broadening of its elution curve (Figure 2-4). In this acid concentration, Zr was retained by the column, and only 2% to 3% was detected in fractions 5 and 6. The acid concentration where the column separation of Zr and Hf was the greatest was 8.1 M HCl. Increasing the HCl concentration only 0.3 M to 8.4 M caused the *k'* of Hf to become too large, and Hf did not elute off the column within six fractions. The most promising results were obtained using 8.1 M HCl to separate Hf from Zr. Under these conditions, the majority of the Hf eluted in the first six fractions (90 ± 1%) while almost none of the Zr was detected (< 5%). This system shows promise for a future extraction chromatographic study of Rf.

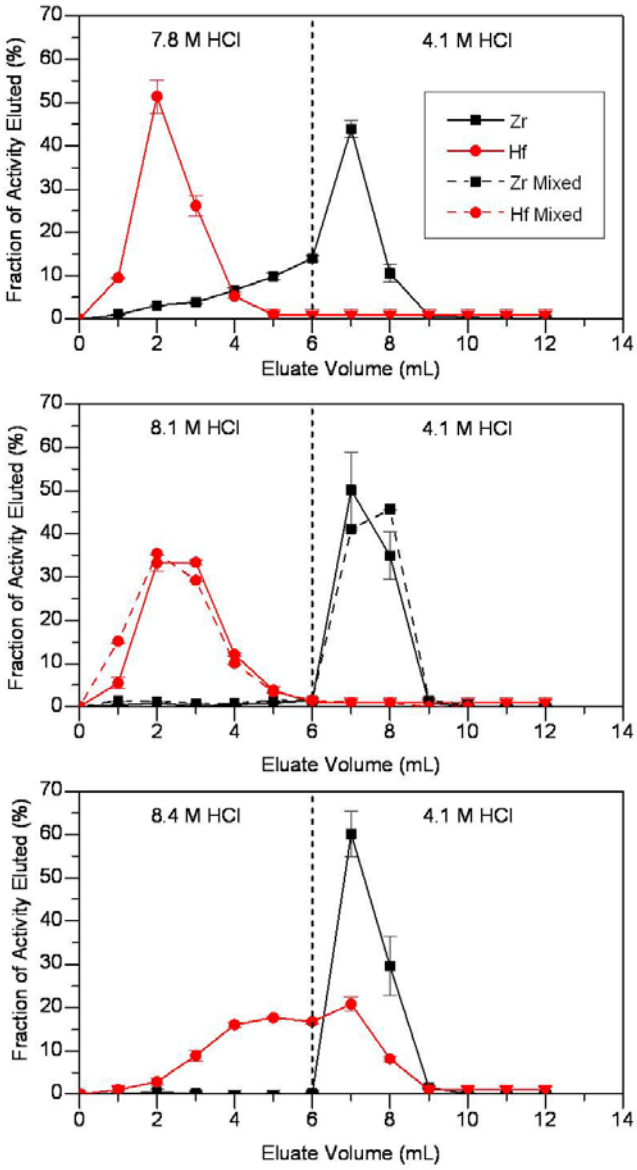

Figure 2-4. HCl elution profiles for Zr and Hf using a 2 ml TEVA resin cartridge with a flow rate of ~1 ml/min. The first fraction is the load fraction. The HCl concentration of the load sample and subsequent five fractions is different in each panel: 7.8 M (top), 8.1 M (middle), and 8.2 M (bottom). The solid-lined results are averages from the triplicate column studies performed with ^{89}Zr and ^{175}Hf, separately. The dashed-lined results in the middle panel are from the mixed radionuclides column study. Arrows indicate upper limits.

The results of the 8.1 M HCl TEVA column study were confirmed by a mixed radionuclide column study using ^{88}Zr and ^{175}Hf (Figure 2-4). Spectra from the HPGe detector can be seen in Figure 2-5. The spectrum of the load sample (Figure 2-5) shows the two radionuclides together before they were separated by the TEVA column. The spectrum of fraction 2 (Figure 2-5) indicates how well the two elements were separated from each other by the TEVA column in 8.1 M HCl: ~35% of the Hf eluted off the column while only ~1% of the Zr was present in this fraction.

The fractions collected after the column study were counted for significantly more time than the load sample (days versus minutes). The long count times were used so that a statistically significant number of counts could be obtained for the Zr present in the fractions that contained mostly Hf and for Hf in the fractions containing mostly Zr.

The spectrum of fraction 7 (Figure 2-5) shows the recovery of ^{88}Zr from the TEVA column with the use of 4.1 M HCl. The results of the mixed radionuclide column study concurred with the previous column study results, as the majority of the ^{175}Hf eluted in the first six fractions (> 95%) and only a small amount of ^{88}Zr was detected (~7%).

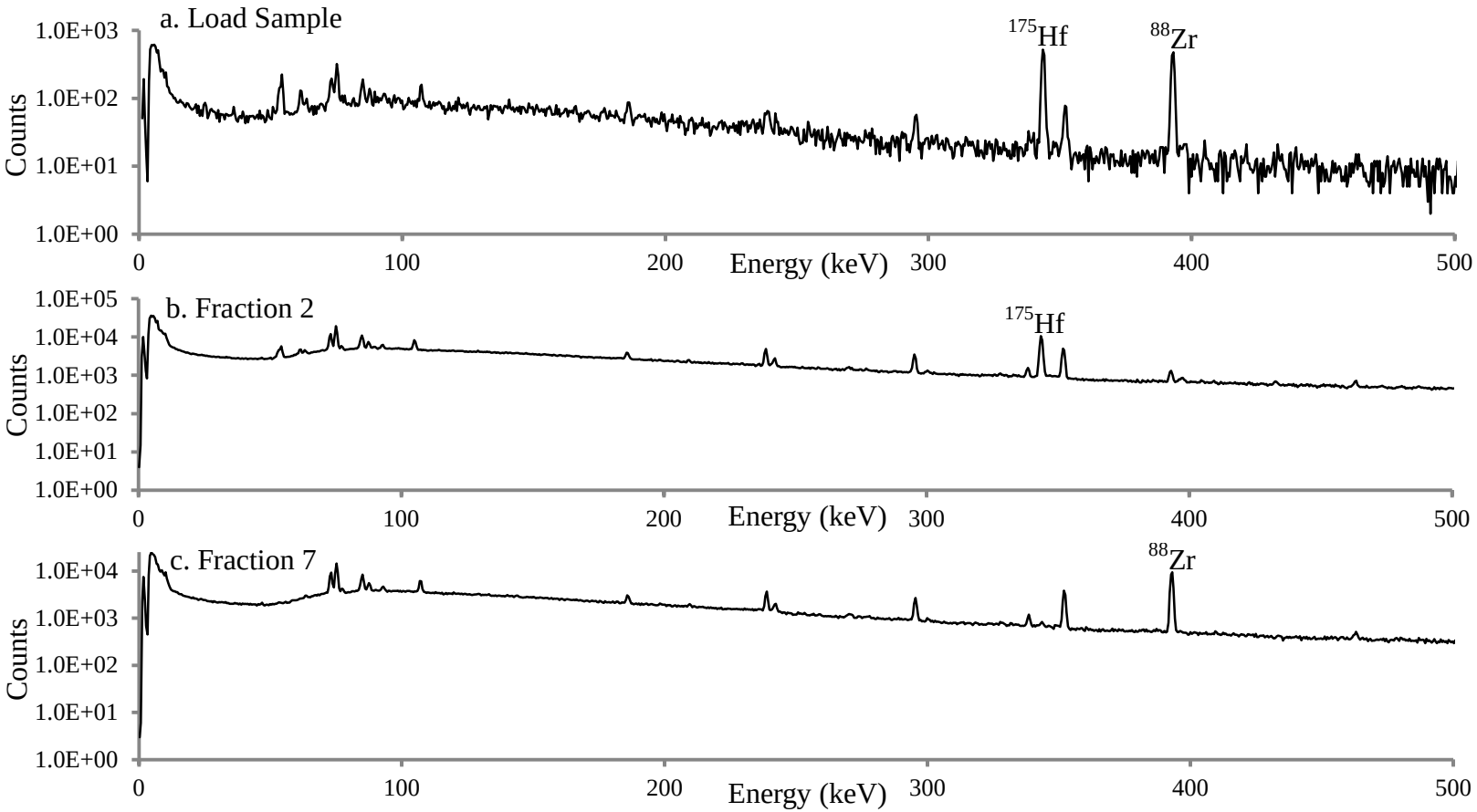

Figure 2-5. HPGe spectra from the TEVA mixed radionuclide column study. The HCl concentration of fractions 1-6 was 8.1 M, while the HCl concentration of fractions 7-12 was 4.1 M. Panel a shows the load sample spectrum before the radioisotopes are separated by the TEVA column. Panel b (fraction 2) shows the maximum of the elution profile for ^{175}Hf, while Panel c (fraction 7) shows the maximum of the elution profile for ^{88}Zr.

2.3.3 UTEVA Batch Studies

The results from the UTEVA batch studies are shown in Figure 2-6. Again, both the measured extraction and *k'* are shown to depict how the two values correlate with each other. These results were used to determine which acid concentration region to focus on for the column separation of Zr and Hf.

UTEVA extraction of ^{89}Zr and ^{175}Hf in an HCl medium showed significant separation of Zr and Hf (top of Figure 2-6). The UTEVA resin did not extract Zr or Hf in samples with HCl concentrations less than 4 M. This is most likely due to the ions forming cationic species in this HCl concentration range since UTEVA is a neutral extractant [76]. Similar to the TEVA batch study results, Zr was retained by UTEVA at a lower acid concentration than that required by Hf. This suggested that at ~5 M HCl, Zr began to form neutral species while Hf remained cationic. UTEVA did not show affinity for Hf until ~6 M HCl. This was the region where the highest separation factor was measured, greater than 9.4 in 5.6 M HCl. These results supported previous results obtained with neutral extractants [62, 63, 65].

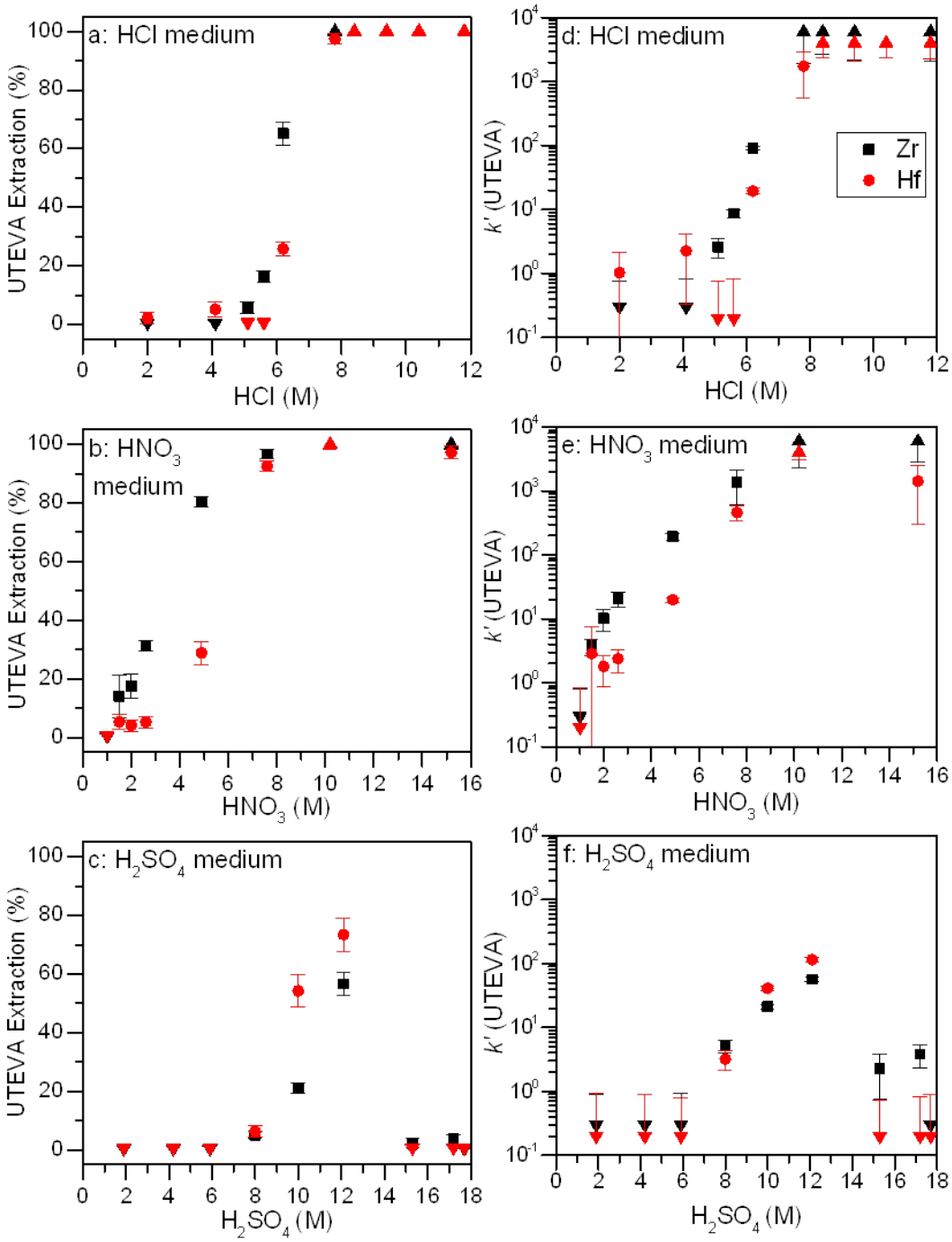

Figure 2-6. Measured extraction (%) and *k'* for ^{89}Zr and ^{175}Hf as a function of acid concentration in batch studies with UTEVA. HCl (top, a and d), HNO_3 (middle, b and e), and H_2SO_4 (bottom, c and f). Downward and upward arrows indicate upper limits and lower limits, respectively.

An unexpected result was that UTEVA retained Zr and Hf at HCl concentrations greater than 8 M. The TEVA batch study had suggested that, in this concentration region, Zr and Hf formed anionic species. However, the UTEVA results can be explained by the equilibrium between neutral and anionic species being shifted whenever an extractant molecule retains a neutral Zr or Hf complex. When the neutral species is extracted by UTEVA, the equilibrium shifts to favor neutral complexes so an anionic complex is converted; this process continues until all of the Zr and Hf complexes are retained by the resin. A similar phenomenon has been seen with cationic and anionic exchange resins in low H_2SO_4 concentrations [81].

The UTEVA batch study in a HNO_3 medium showed promise for the column separation of Zr and Hf. Unlike TEVA, UTEVA did show an affinity for Zr and Hf (middle of Figure 2-6). At low concentrations of HNO_3 (< 2 M), UTEVA did not retain Zr or Hf. Likewise, TEVA also did not show any affinity for Zr or Hf in this HNO_3 concentration region, suggesting that Zr and Hf formed cationic complexes at low HNO_3 concentration. As observed in the other batch studies, the acid concentration required for the resin to retain Zr were lower than those to retain Hf. The highest separation factor, 10 ± 1, was measured in 4.9 M HNO_3. However, this acid concentration was not considered as the region of interest for the column study because the measured *k'* for Hf (20 ± 2) was too large (see discussion in Section 2.1.4). Instead, the acid concentration region around 2.6 M HNO_3 was considered, since it produced a separation factor of 9 ± 4 and Hf's *k'* was measured as 2.4 ± 0.9.

The results from the UTEVA in H_2SO_4 batch study were of particular interest since it was the only system where the resin had a higher affinity for Hf than Zr (bottom of Figure 2-6). The complexation of Zr and Hf in H_2SO_4 is complicated because successive formation reaction constants for sulfate complexes do not vary greatly [81]; cationic (M^{4+} and $M(SO_4)^{2+}$), neutral ($M(SO_4)_2$), and anionic ($M(SO_4)_3^{2-}$ and $M(SO_4)_4^{4-}$) species can coexist in H_2SO_4 solution [80, 81]. UTEVA did not retain Zr and Hf in samples ranging from 2.0 M to 6.0 M H_2SO_4, suggesting that Zr and Hf did not form neutral complexes in this concentration region. When the uptake of Zr and Hf was measured in acid concentrations greater than 8.0 M H_2SO_4, the resin had a higher affinity for Hf than Zr (bottom of Figure 2-6).

It was also noted that the UTEVA resin did not retain Zr or Hf at high H_2SO_4 concentrations; this may be because Zr and Hf did not form neutral complexes in this concentration region. However, a more likely explanation is that the UTEVA resin was being destroyed. This can occur by two different mechanisms: Either the stationary phase (i.e., extractant) separates from the inert support and then passes through the filter during the batch study, or the extraction molecule (diamyl amylphosphante) chemically degrades under these hash conditions [55]. A color change of the solution, colorless to yellow, was observed with the samples tested in concentrated H_2SO_4 (Figure 2-7). The darkest yellow sample contained the most resin (18.6 mg), supporting the theory that the resin was being destroyed.

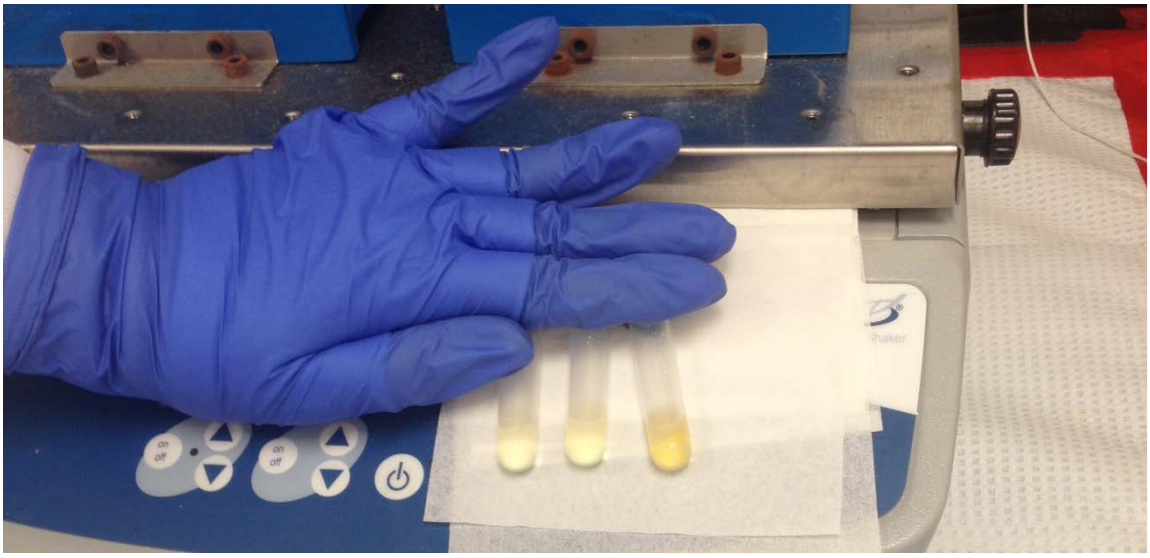

Figure 2-7. Picture of UTEVA batch study samples in concentrated H_2SO_4 medium. The color change from colorless to yellow is evidence that the resin cannot withstand the high acid concentration

The more interesting result of the UTEVA in H_2SO_4 batch study was that Hf was *preferentially* extracted over Zr. The highest separation factor, 2.0 ± 0.2, was measured in 10.0 M and 12.1 M H_2SO_4. However, column studies were not considered because Zr's measured *k'* (21 ± 2 and 57 ± 4, respectively) were too high. In a chromatographic separation a large number of free column volumes would be needed to elute Zr off the column, which would not be conducive for a transactinide experiment.

2.3.4 UTEVA Column Studies

Based on the UTEVA batch study results, the HCl concentration range 4.5 to 6.0 M was studied for viability in column separations. The results of these column studies are shown in Figure 2-8. Various acid concentrations (4.6, 5.1, and 5.6 M HCl) were studied for column separation of Zr and Hf; at these acid concentrations, it was expected

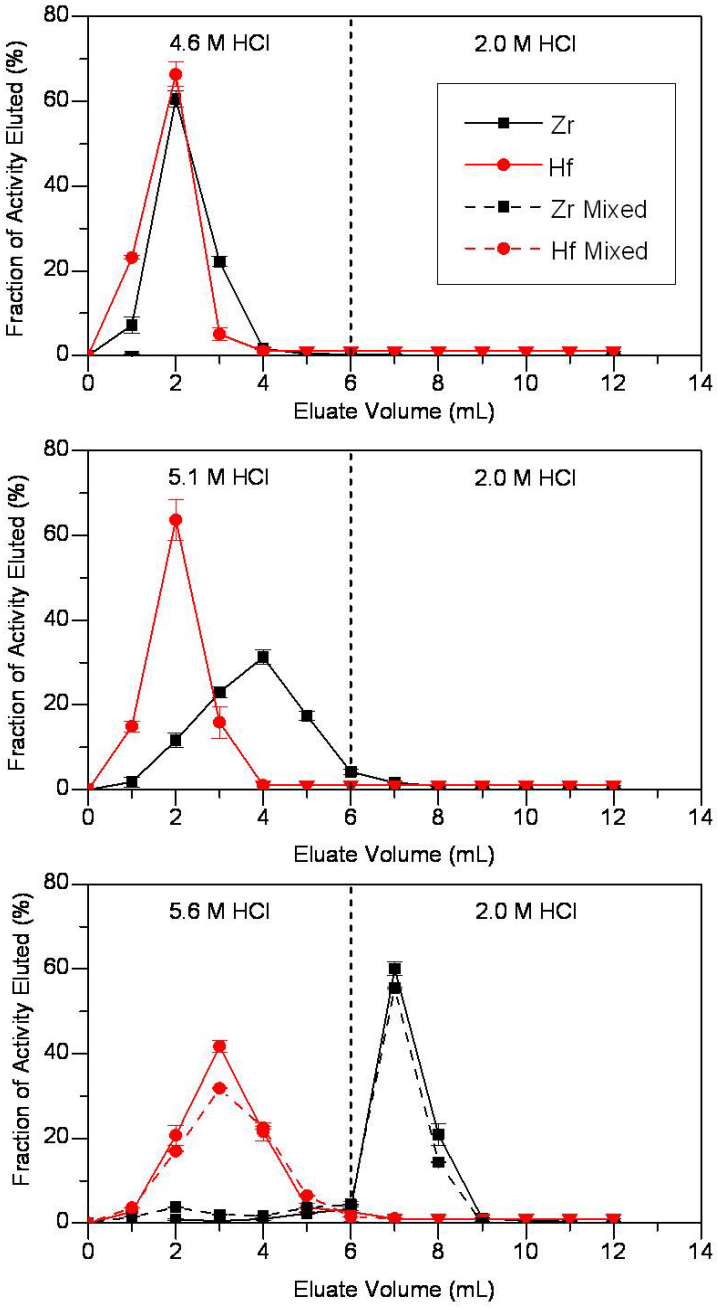

Figure 2-8. HCl elution profiles for Zr and Hf using a 2 ml UTEVA resin cartridge with a flow rate of ~1 ml/min. The first fraction is the load fraction. The HCl concentration of the load sample and subsequent five fractions is different in each panel, 4.6 M (top), 5.1 M (middle), and 5.6 M (bottom). The solid-lined results are averages from the triplicate column studies performed with ^{89}Zr and ^{175}Hf, separately. The dashed-lined results are from the mixed radionuclides column study. Arrows indicate upper limits

(based on batch study results) that Zr would be retained by the column while Hf would elute. Then six fractions of 2.0 M HCl were used to remove any remaining radionuclides. At this acid concentration, *k'* of less than or equal to 1 was measured for both Zr and Hf. Again, the increase in *k*' with HCl concentration is depicted by the elution curves in Figure 2-8. In 4.6 M HCl, Zr's elution curve is almost identical to Hf's elution curve; there is no separation. With a small increase of HCl concentration (to 5.1 M), Zr's *k'* increased (2.6 ± 0.9) and its elution curve broadened significantly. However, in 5.1 M HCl, Hf's elution curve did not change and *k'* remained constant (< 1), which supported the batch study results (Figure 2-6).

The best column separation of Zr and Hf was obtained using 5.6 M HCl, since the majority of the Hf eluted in the first six fractions (93 ± 2%), while Zr was mostly retained. Approximately 8% of the Zr was detected in the first six fractions, with the highest amounts found in fractions 5 and 6. A mixed radionuclides column study using ^{88}Zr and ^{175}Hf confirmed these results (Figure 2-8). The results from this column study demonstrated its capabilities to separate Zr and Hf, suggesting that it might be used to study the chemistry of Rf. The data also suggest that there is a possibility that a small improvement can be made in the separation factor by increasing the HCl concentration of the first six fractions to 5.7 - 5.9 M. Unfortunately, the ^{175}Hf used in these experiments was in extremely short supply, with only small amounts of activity being made available approximately once per year. The activity had to be rationed, and the experiments selected in advance. Although it would have been desirable to study

additional HCl concentrations greater than 5.6 M, this was not possible due to these constraints.

There were some inconsistencies between the results from the UTEVA in HNO_3 medium batch study and the corresponding column study. The most significant issue was that any Zr and Hf retained by the column could not be subsequently eluted from the column.

Based on the results from the batch study, 1.0, 2.0, and 2.6 M HNO_3 were tested for the UTEVA column separation of Zr and Hf (Figure 2-9). The results in the top panel of Figure 2-9 were in agreement with the batch study. The elution curves for both Zr and Hf were identical in 1.0 M HNO_3, indicating that UTEVA did not retain either element. This was consistent with the batch study where a *k'* of less than 1 was measured for both elements. Based on these results, it would also suggest that 1.0 M HNO_3 could be used for fractions 7 through 12 to remove any remaining radionuclides retained on the column after the separation.

The discrepancies between the results from the UTEVA in HNO_3 medium batch study start with the middle panel of Figure 2-9. The batch study measured a *k'* for UTEVA of 10 ± 4 for Zr and 2 ± 1 for Hf in 2.0 M HNO_3. The elution curve for both Hf and Zr did not change from the top panel to the middle panel even though larger *k'*s were measured in the batch study. Both elution curves should have shifted and broadened, and this effect should have been more significant with Zr due to the larger *k'* measured in the batch study. Another surprising result was that only 70% of the Zr eluted in the first three fractions and none was detected in fractions 4-6. This was evidence that some

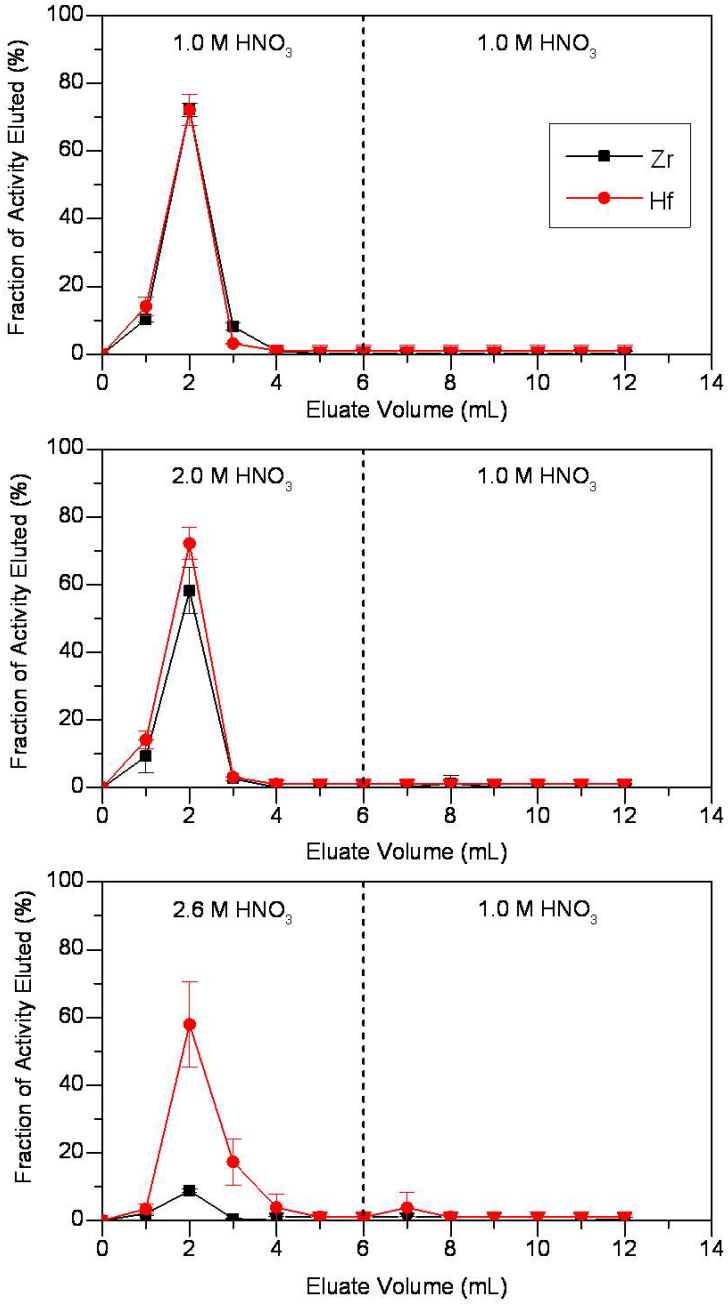

Figure 2-9. HNO_3 elution profiles for Zr and Hf using a 2 ml UTEVA resin cartridge with a flow rate of ~1 ml/min. The first fraction is the load fraction. The HNO_3 concentration of the load sample and subsequent five fractions is different in each panel, 1.0 M (top), 2.0 M (middle), and 2.6 M (bottom). The solid-lined results are averages from the triplicate column studies performed with ^{89}Zr and ^{175}Hf, separately. Arrows indicate upper limits.

of the Zr formed neutral species that were retained by the column. Lastly fractions 7-12 showed that 1.0 M HNO_3 could not be used to remove the remaining Zr from the column, which was unexpected.

The inconsistencies between the results from the UTEVA in HNO_3 medium batch study and column study can be explained by the "resin/solution contact time" differences between the two methods. During a batch study the resin mixes with the solution for 1 h, while the columns are run with a solution flow rate of 1 ml/min. The contact time for the column study in considerably less than the batch study. If the rate of a reaction does not occur on a timescale comparable to the contact time of the column, there will be discrepancies between batch and column study results.

The partial elution of Zr suggested that multiple species, cationic and neutral, coexisted in solution. This was not evident in the batch study because the contact time was so much longer than the column. When a neutral species is extracted by UTEVA, the equilibrium shifts to favor neutral complexes so a cationic complex is converted; this process continues until all of the Zr and Hf complexes are retained by the resin. For this reason, the batch study measured a higher *k'* than the column study. The inability to remove the Zr after it was retained by the column suggests that the kinetics of going from a neutral to a cationic species in 1.0 M HNO_3 did not occur on a timescale adequate for columns with a flow rate of 1 ml/min.

The bottom panel continued the trend of inconsistencies between the results from the UTEVA in HNO_3 medium batch study and column study. In 2.6 M HNO_3 the elution curve again did not broaden or shift suggesting the *k'* was less than 1 even

though the batch study results suggested otherwise. Also, there was a partial elution of Zr (~11%) and Hf (~80%) in fraction 1 through 6 and 1.0 M HNO_3 could not be used to remove the remaining nuclides from the column.

These results suggest that the UTEVA in HNO_3 system cannot be used for a future study of online-produced elements, including Rf. As discussed in Section 1.4.2, during online chemistry experiments, the presence of a radioisotope is unknown until the two elution fractions are analyzed. The element of interest *must* elute from the column in at least one of the two acid concentrations. Since none of the UTEVA in HNO_3 column studies showed promise for online chemistry, a mixed radionuclide study was not performed.

2.4 Conclusions

The separation of Rf homologs using TEVA and UTEVA resins in HCl, HNO_3, H_2SO_4 have been investigated. Three out of the six systems studied did not show encouraging results for probing the intergroup trend of Group IV elements. TEVA did not exhibit affinity for Zr or Hf in either nitric acid or sulfuric acid media; these systems were unable to discern the chemical differences between Group IV elements. On the other hand, the UTEVA batch study in an HNO_3 medium showed evidence of good intergroup separation. Separation factors of 9 ± 4 and 10 ± 1 were measured in 2.6 and 4.9 M HNO_3, respectively. Despite that, UTEVA did not show promise for studying Rf chemistry in a column setting because Zr retained by the column could not be recovered.

However, two systems showed promise for the future extraction chromatographic study of Rf. The TEVA batch study in an HCl medium had a maximum measured

separation factor of 18 ± 8 in 8.4 M HCl. The best TEVA column separation of Hf from Zr was observed using 7.8 M HCl as the eluent. Within the first six fractions, 90 ± 1% of the Hf eluted while more than 95% of the Zr stayed on the column. The UTEVA batch study in an HCl medium had a maximum measured separation factor of greater than 9.4 in 5.6 M HCl. The best UTEVA column separation of Hf from Zr was observed using 5.6 M HCl as the eluent. Within the first six fractions, 93 ± 2% of the Hf eluted while ~ 92% of the Zr stayed on the column.

Lastly, the UTEVA in H_2SO_4 system had the most interesting results. In this system, Hf was shown to have a higher affinity for the resin than Zr. At both 10.0 M and 12.1 M H_2SO_4, a separation factor of 2.0 ± 0.2 was measured. This system did not show promise for extraction chromatographic studies of Rf. However, a batch-like online chemical study should still be considered for analyzing the chemistry of Rf. Most, if not all, the systems used to study Rf have had a greater affinity for Zr than Hf [59-65]. A discussion of the future work needed to modify the promising systems for the chemical characterization of Rf can be found in Chapter IV.

CHAPTER III*

COMMISSIONING OF A GAS STOPPER

A new gas stopper has been commissioned for the study of fusion-evaporation-reaction products. This device uses a combination of gas flow and an electric field to efficiently transport the EVRs. Simulations of these two forces were used to determine the final design. Once fabricated, the device was characterized "offline" using the daughters from a ^{228}Th electroplated source and online using a high-cross-section fusion evaporation reaction, ^{40}Ar(^{118}Sn, 6n)^{152}Er. This chapter will discuss each step in this process.

3.1 Design and Simulations

3.1.1 Design Principles

The design of the RTC was intended to employ the best characteristics of "traditional" gas stoppers used for heavy element chemistry experiments at Lawrence Berkeley National Laboratory [24], at RIKEN [25], and at the GSI [26]. These characteristics were combined with modern ideas on the use of electric fields to guide ions employed at Argonne National Laboratory [32, 33], at RIKEN [35-37], and the NSCL [27-30]. The NSCL device was especially influential on the final design since, in contrast to the Argonne design, it did not require the fabrication of a complex RF

*Part of the data reported in this chapter is reprinted with permission from M. C. Alfonso *et al.*, Nucl. Instr. Meth. Phys. Res. A, **798**, 52-61 (2015), ©2015 Elsevier B.V.

system. This section describes the general design principles, and the following section describes the simulation program used to verify these design principles.

A schematic of the new RTC design can be seen in Figure 3-1. This device is considerably shorter than NSCL gas cell due to the difference in kinematics of projectile fragmentation reactions and fusion evaporation reactions. EVRs are produced with orders of magnitude lower energy than fragmentation products (150–250 keV/u versus tens of MeV/u); therefore, their range is considerably shorter and their stopped distribution is considerably narrower.

Before the ions are stopped in the gas cell, they are slowed by a rotating variable angle degrader (VAD) and the entrance window of the gas cell. The entrance window for this new gas cell is 2.0-μm aluminized Mylar (polyethylene terephthalate) supported by a honey-comb grid; this is the barrier between the beamline vacuum and the RTC gas. Directly upstream of the entrance window is a "protector screen" to prevent pieces of the window from escaping if it fails.

Based on SRIM [82, 83] energy-loss calculations, the VAD also needed to be significantly thinner than the 1.5-mm-thick glass used at NSCL, so a Mylar foil was chosen. The VAD thickness in the online experiment discussed in Section 3.4.2 was 5.9 ± 0.1 μm, although it can be changed based on the energetics of the fusion evaporation reaction and EVR of interest.

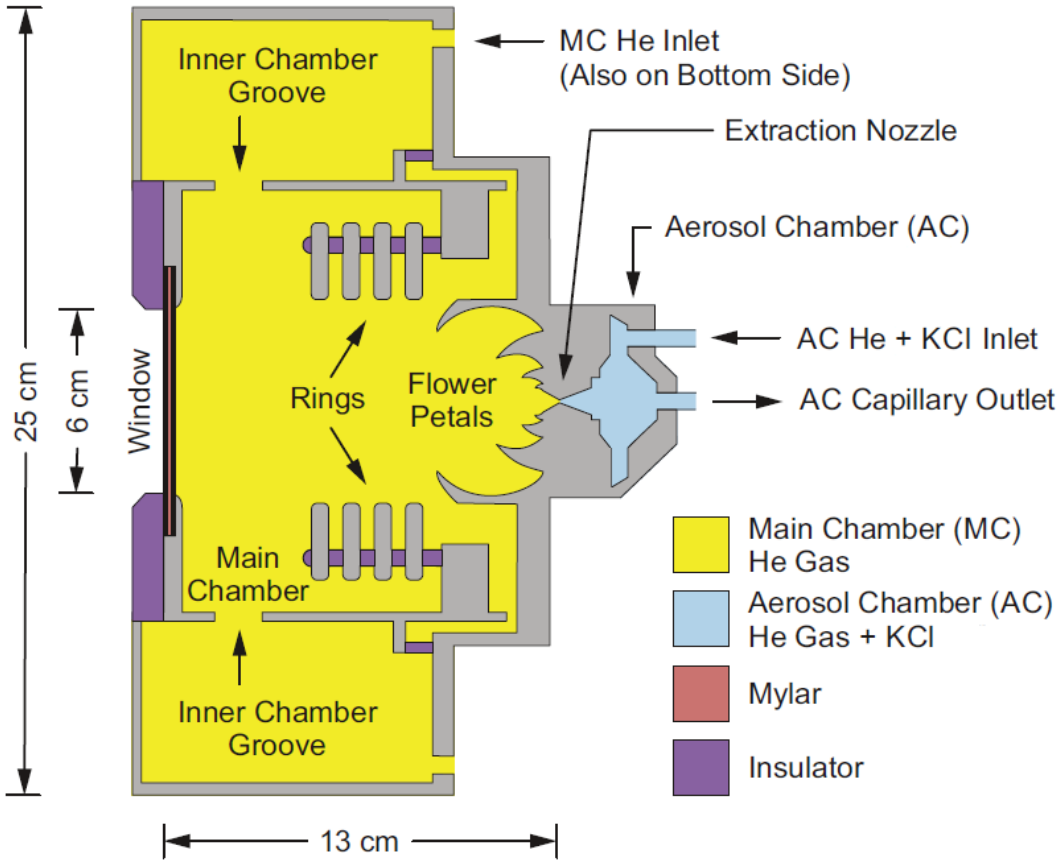

Figure 3-1. Schematic of the RTC. The ions enter the He-filled Main Chamber (shown in yellow) of the RTC through the window after passing through a variable angle degrader (not shown). A series of electrodes (shown in gray) create an electric field that, along with gas flow, draws the ions to the Aerosol Chamber (shown in blue).

The ions enter He gas with a pressure of 228 torr; the selection of the gas pressure is discussed in Section 3.1.2. The depth of this "stopping region" is 5 cm. An outer expansion chamber is used to reduce buffering in the gas entering the device, which required the addition of an "Inner Chamber Groove."

The electrode system design has many similarities to the one used in the NSCL device. Some alterations were made based on simulation results (see Section 3.1.2).

However, it works on the same principles: First a series of ring electrodes with decreasing potentials pull the stopped particles through them, and then four concentric hemispherical “flower petal” electrodes focus the ions into an Extraction Nozzle. The inner diameter of the rings is 5 cm and they are spaced 0.5 cm apart. Similar to the NSCL device, a laminar gas flow throughout the entire device aids the electric field in the transportation of thermalized ions, and the gas flow becomes the dominant force that pushes the ions through the Extraction Nozzle at the end of the gas stopper.

Another significant change to the design was the addition of an Aerosol Chamber (AC) (Figure 3-1). In order to study the liquid phase chemistry of EVRs, they must be transported through a relatively long capillary (up to ~30 m) to a chemistry laboratory. Ions are typically attached to KCl aerosols to prevent them from getting caught on the sides of the capillary. However, aerosols cannot be used in the Main Chamber (MC) because the aerosols would make the ions heavier and could possibly neutralize the ions, eliminating the focusing ability of the electrode system. Due to the small diameter of the Extraction Nozzle (0.6 mm), a slight difference in pressure (DP) between the two chambers can be maintained in order to limit the aerosol contamination of the Main Chamber ($DP = P_{MC} - P_{AC}$). Once in the AC, the EVRs attach to KCl aerosol clusters, which aid in the transmission of the ions through the capillary.

3.1.2 Electrode System Simulations

The design of the electrode system was optimized through a series of simulations. The newly commissioned RTC was built to thermalize EVRs after they were purified using the Momentum Achromat Recoil Spectrometer (MARS) as a

physical pre-separator (See Section 3.3.4 for discussion of MARS). Fusion evaporation reactions previously used for the online chemical study of Rf and its homologs were considered: ^{70}Ge(^{18}O,3n)^{85}Zr [84, 85], ^{124}Sn(^{50}Ti,5n)^{169}Hf [84, 85], and ^{208}Pb(^{50}Ti,n)^{257}Rf [9]. LISE++ [86] was used to simulate the expected energy and spatial distribution of EVRs exiting MARS (Table 3-1). SRIM [82, 83] was then used to simulate the width of the thermalized ions in the longitudinal direction and their angular straggling after passing through the VAD and the window. A combination of the results from both LISE++ and SRIM simulations gave the initial spatial distribution of the thermalized ions for an assumed He gas pressure.

Table 3-1. Properties of the reactions used to simulate the RTC. Targets were assumed to have a thickness of 500 μg/cm^2 with a ~50 μg/cm^2 ^{nat}C stripper foil directly downstream. Reduced mobilities were estimated using [87]

Reaction	EVR energy after stripper foil (MeV)	Horizontal FWHM (mm)	Vertical FWHM (mm)	Estimated reduced mobility ($cm^2\ V^{-1}\ s^{-1}$)
^{70}Ge(^{18}O, 3n)^{85}Zr	12.5 ± 1.9	_*	17.2	15.9
^{124}Sn(^{50}Ti, 5n)^{169}Hf	53.6 ± 3.1	_*	13.1	15.7
^{208}Pb(^{50}Ti, n)^{257}Rf	39.5 ± 1.2	29.8	7.7	15.6

* The distribution was only slightly peaked in the horizontal direction.

SIMION [88] was used to simulate the trajectory of the thermalized ions due to the RTC's electrode system after stopping. The RTC was modeled in SIMION with cylindrical symmetry; the figures shown throughout this chapter are two-dimensional slices. The Statistical Diffusion Simulation (SDS) Model user program [89] was used to

simulate the effects of large number of collisions between the ions and gas atoms. This program required reduced mobility of the EVRs (Table 3-1), which was estimated using data from [87].

Many different design elements of the RTC were varied in SIMION: the number of rings, the distance between the entrance and the ring region, and the number and size of flower petals. A 0.1 mm x 0.1 mm grid size was used for the SIMION simulations. When a larger grid size was tested the resolution was not high enough to accurately depict the shape of the flower petal electrodes. The extraction efficiency was estimated from the fraction of ions that reached a chosen plane perpendicular to the beam axis in the nozzle region.

The distance between the entrance widow and the ring region is critical to the performance of the RTC. This is the where the ions will come to rest, so it is important that this region is large enough to contain the entire stopped distribution. Like the NSCL device, the RTC is designed so that the centroid of the stopped distribution can be controlled by the VAD angle. The effective degrader thickness increases with the reciprocal of the cosine of its angle: If the ions stop too far into the RTC, then the VAD angle can be increased. (In practice, the window thickness is also added to the effective VAD thickness since both are made of Mylar.)

The optimum angle for the VAD was estimated to be 25° to 30°. This angle allows for significant energy loss adjustments to be possible in either direction. SRIM calculations suggested that the stopped distribution width for the studied EVRs (Table 3-

1) would be ~5 cm in 228 torr He, so 5 cm was chosen as the distance from the window to the first ring. A pressure of 228 torr was also used in the following simulations.

Across the ring region, a series of resistors creates a linear decrease in potential between rings 1 and 4, which pulls the thermalized ions to the flower petal region. The optimum number of rings was determined to be four. Fewer rings did not provide adequate separation of the electric fields produced by the window and the flower petals, but increasing the number of rings did not result in enhanced extraction. Another benefit of a shorter gas cell is a shorter extraction time.

Simulations were run with different flower petal electrode designs; the diameters of the flower petals were altered and the addition of a fifth flower petal was considered. Overall, there was a negligible change in the extraction efficiency and distribution between the simulated designs. Furthermore, during the design phase of this project, it was discovered that the NSCL's gas cell had been decommissioned and was available for us to repurpose. After simulating the NSCL unit design, it was decided to reuse that flower petal system. This decision saved a significant amount of time in the design and fabrication of the RTC; since the flower petal system was very complex, each petal would have had to be electrically isolated from the others.

Simulations showed advantages to biasing the walls of the device and the entrance window. The equipotential lines of the NSCL gas stopper (Figure 1-6) suggested that the ions stopped in the first ~20% of the gas cell would be defocused due to the grounded beryllium window, so biasing the window was simulated. It was discovered that including a bias difference between the RTC window and first ring

created an extra focusing region. The outer walls of the RTC must be grounded for safety reasons, but when this was simulated, the resulting equipotential lines were unusable (Figure 3-2, left), resulting in defocusing in both the stopping region near the window and in the rings. The optimum solution to this problem was biasing the walls to the same potential as the RTC window (Figure 3-2, right). Thus, a grounded outer chamber was added to the design. This outer chamber also created an expansion chamber that reduced buffering in the He gas entering the MC.

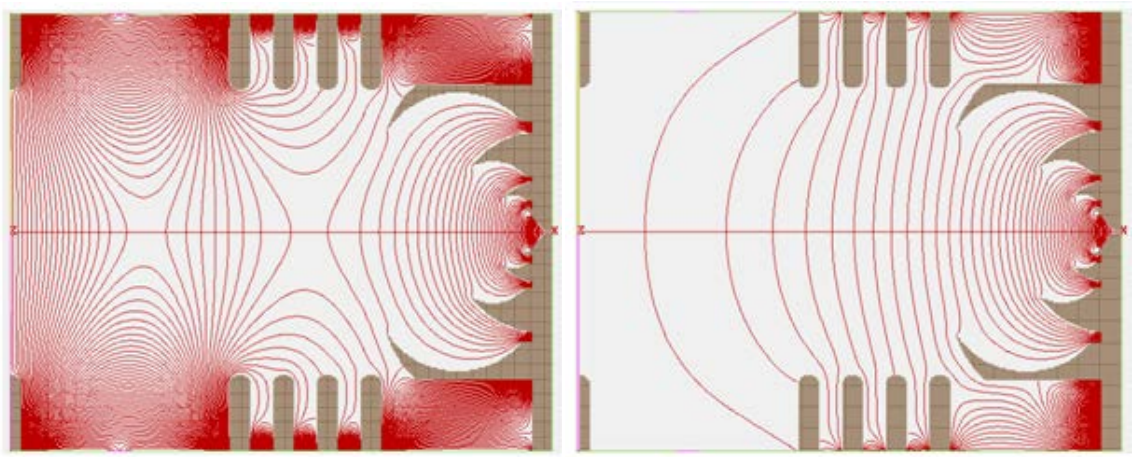

Figure 3-2. Equipotential line diagrams determined by SIMION of the RTC with grounded walls and biased walls. Left: Equipotential lines of the RTC with grounded walls. Right: Equipotential lines of the RTC with walls with the same bias as the entrance window. Ions travel perpendicular to the equipotential lines. The difference in potential between each line is 10 V in both images.

A large number of potential gradients were simulated with a variety of shapes and magnitudes. The optimum potential gradient was qualitatively similar to the one used at NSCL (Figure 1-5). One significant difference in the current design is that the

entrance window is biased to the same potential as the first ring. In the flower petal region, the potential decreases more rapidly and the shape of the electrodes causes the ions to be focused into the extraction nozzle. The simulated optimum biases are shown in Figure 3-3. Various EVRs (Table 3-1) were simulated in SIMION, and the probability of reaching the entrance to the nozzle was greater than 70% for all reactions.

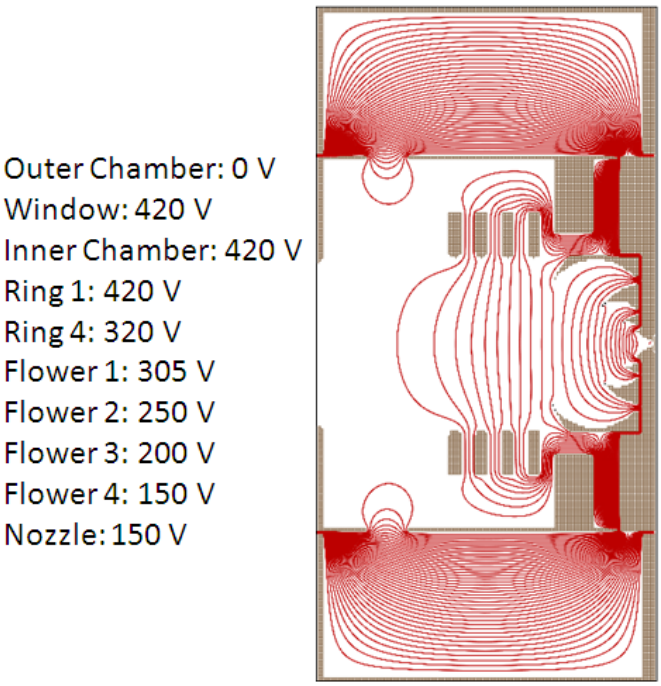

Figure 3-3. Optimum electrode system settings and the corresponding equipotential line diagram determined by SIMION. Ions travel perpendicular to the equipotential lines. The difference in potential between each line is 10 V.

3.1.3 Gas Flow Simulations

The design of the gas cell was also driven by results from gas flow simulations using the STAR-CCM++ program [90]. Figure 3-4 shows the flow simulation results for the finalized RTC design. It was critical that the gas flow in the MC did not hinder the focusing of the electrode system; the gas flow could not have any eddies where the ions could get trapped. The addition of an outer chamber was advantageous to the gas flow because the inner chamber could then have a groove-like inlet for the helium gas. This allowed the gas to equilibrate in the outer chamber before entering through the Inner Chamber Groove and interacting with the stopped ions. Also, in the Extraction Nozzle region, there was minimal focusing due to the electrode system; gas flow became the dominate force in this region. Therefore, the gas flow had to be optimized to aid in ion extraction. Lastly, in the AC, the gas flow had to carry the ion-aerosol clusters into the capillary (Figure 3-4). Previous gas cell experiments suggested that the flow in the capillary became turbulent at flow rates greater than 2 to 3 L/min [91], resulting in loss of ions to the side of the capillary walls. Therefore, the gas flow rate across the Extraction Nozzle was simulated at 2 L/min, and the capillary flow rate was simulated at 2.5 L/min.

The results of the final STAR-CCM++ simulations were included in the final SIMION simulations. A gas flow vector map from STAR-CCM++ was imported using the optional “bulk gas velocity fields” variable in the SDS user program. These final results validated the design principles discussed above.

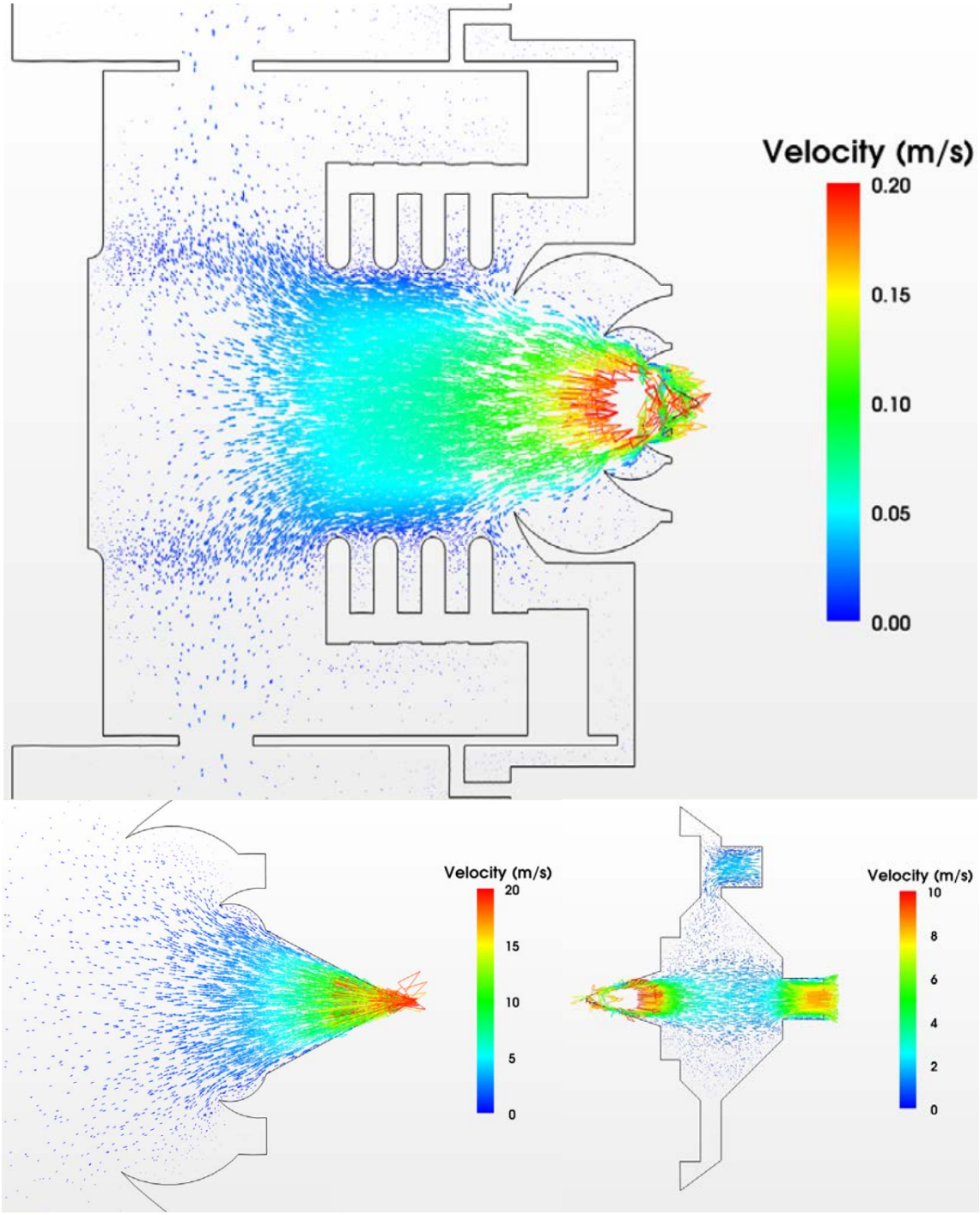

Figure 3-4. STAR-CCM+ simulation of the gas flow in the RTC. Top: STAR-CCM+ simulation of the gas flow in the MC. Bottom left: Detail of the gas flow in the nozzle region. Bottom right: Detail of the gas flow in the Aerosol Chamber. Note that the scales are different between the three panels.

3.1.4 Gas-Handling System

The purity of the gas in the MC was very important to the effectiveness of the electrode system [32]. EVRs could be neutralized by forming molecules with contaminants present in the He gas. The He used inside RTC was purified by a MonoTorr Rare Gas Purifier from SAES Pure Gas, which reduced the level of impurities (H_2O, O_2, CO, CO_2, H_2, N_2, and other hydrocarbons) to ppb levels [92]. Outgassing of the material inside of the RTC could also be a source of impurities in the He [37]. A majority of the device was made of stainless steel, but the insulators were made of Macor ceramic and polyphenylene sulfide. These two materials were chosen for their low adsorption of moisture, low outgas rates, and ability to withstand temperatures of ~90°C. All vacuum seals of the RTC were Cu gaskets with the exception of the RTC window seals. Viton o-rings were used because they have low outgas rates and could also withstand temperatures of ~90°C. Before the device was used in an online experiment, the entire RTC was baked at ~90°C for 48 hours to further decrease the impurity levels.

A schematic of the gas-handling system is shown in Figure 3-5. Again this entire system was bakeable, made of all-metal valves and metal seals. The RTC had two inlets, one to each chamber. A series of hand valves made it possible for the gas entering the AC to have two options: to pick-up aerosols from an aerosol generator or not. During the commissioning experiments of the RTC, the aerosol generator was bypassed. A pressure transducer (P_{MC} in Figure 3-5) was used to measure the pressure in the MC, while a differential pressure transducer (DPT in Figure 3-5) between the

chambers' two inlets measured the DP (P_{MC} - P_{AC}). A LABVIEW [93] proportional-integral-derivative (PID) controller used the pressure information to manipulate the MC and AC computer-controlled valves (shown in purple in Figure 3-5). Lastly, a mass flow controller (MF in Figure 3-5) was used in between the RTC outlet and the vacuum pump (oil-free scroll pump). During future chemistry experiments, a sample collection system will be located upstream of the vacuum pump. A custom interface was built using LABVIEW [93]. Three different variables could be set: pressure in the MC, DP between the MC and AC, and the flow rate out of the RTC (Figure 3-6).

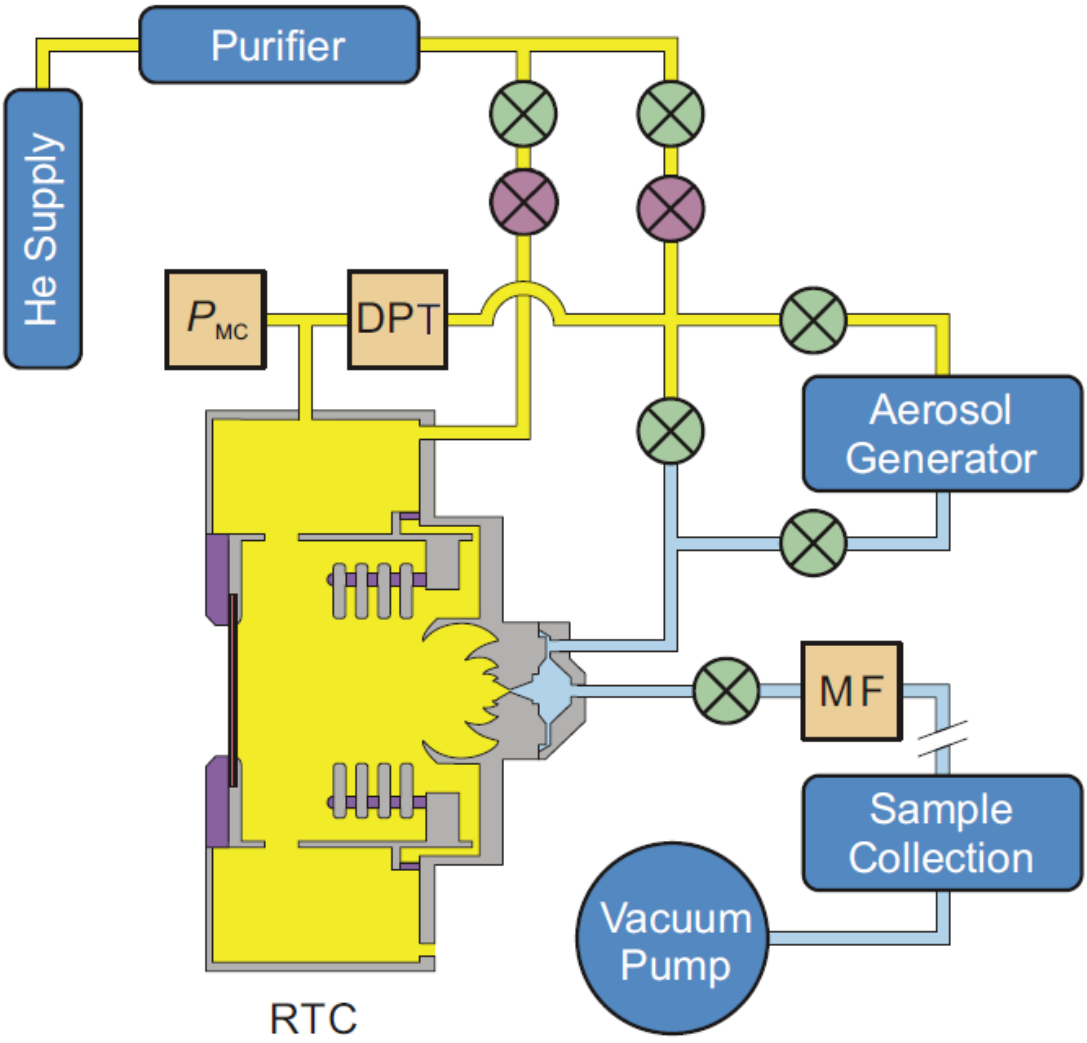

Figure 3-5. Gas-handling system of the RTC. Gas color scheme is that same as figure 3-1. Green circles with an "X" are hand valves while the purple circles with an "X" are computer-controlled valves. P_{MC} is the pressure transducer, DPT is a differential pressure transducer, and MF is a mass flow controller. See the main text for more detail.

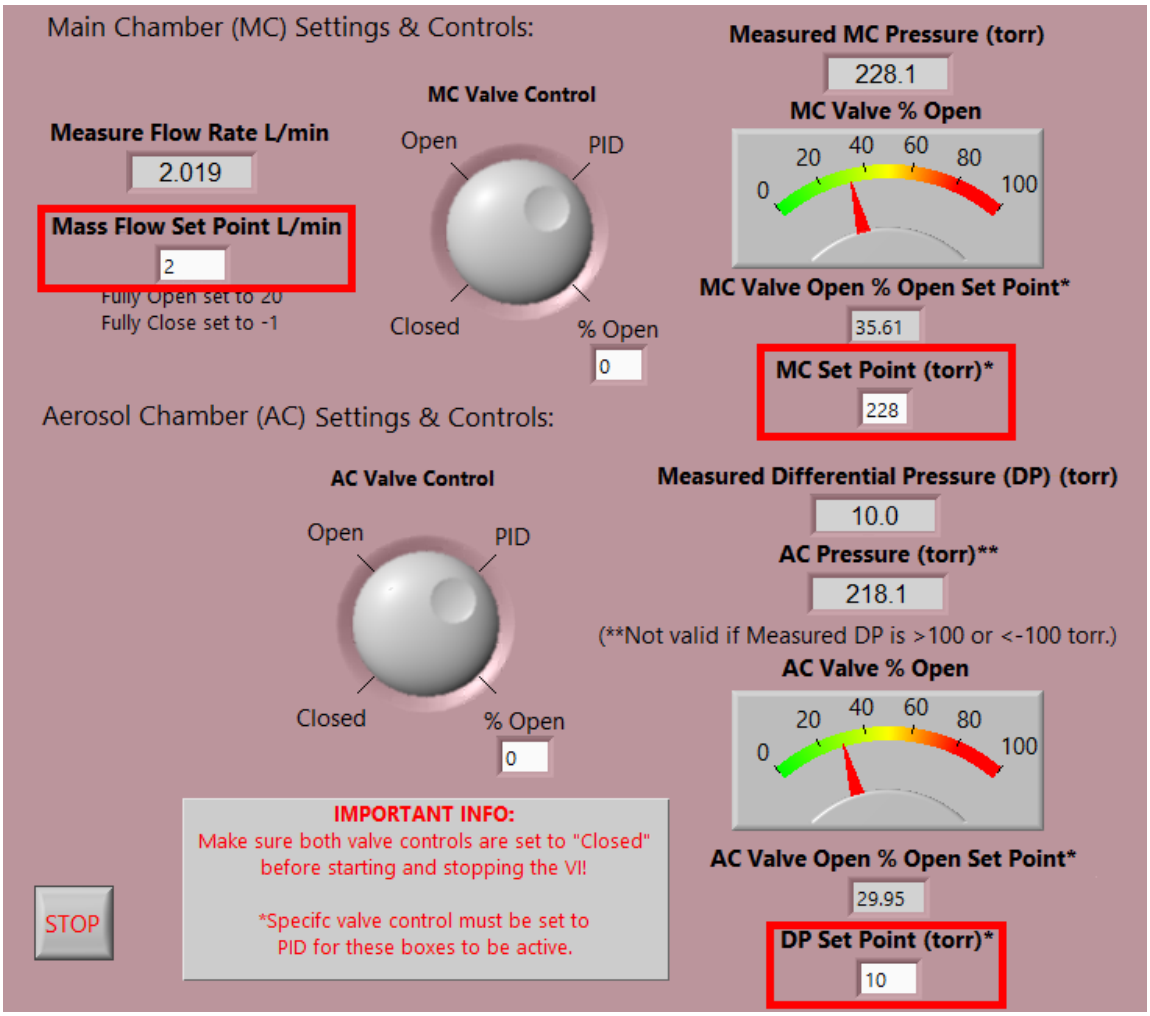

Figure 3-6. Gas-handling system custom interface built using LABVIEW. Conditions of the RTC that can be set by user are surrounded in a red box. The MC and AC Valve Control dials allowed the user to force the computer controlled valves to either: fully opened, fully closed, opened to a set amount, or be controlled by the LABVIEW's proportional-integral-derivative (PID) controller.

3.1.5 Detector System

A two-detector system was installed in this RTC to monitor the transportation of ions through the system (Figure 3-7). A Canberra large-area (~2000 mm^2), ruggedized Si detector was placed behind the RTC window (MC detector). This particular Si detector was considerably more robust than the average Si detector: It was bakeable and could work at high pressure. The MC detector was attached to a linear actuator so it could be plunged in and out of the path of the EVRs. An identical detector was placed directly downstream of the Extraction Nozzle (AC detector) to measure the rate of EVRs successfully being transported by the MC. This made it possible to measure the effect of varying the gas flow and electrode system settings on the EVR transportation efficiency. The second detector required the AC to be retractable. This was done by attaching the downstream half of the chamber to a bellows system, so when necessary, the chamber could be pulled out of the way of the detector.

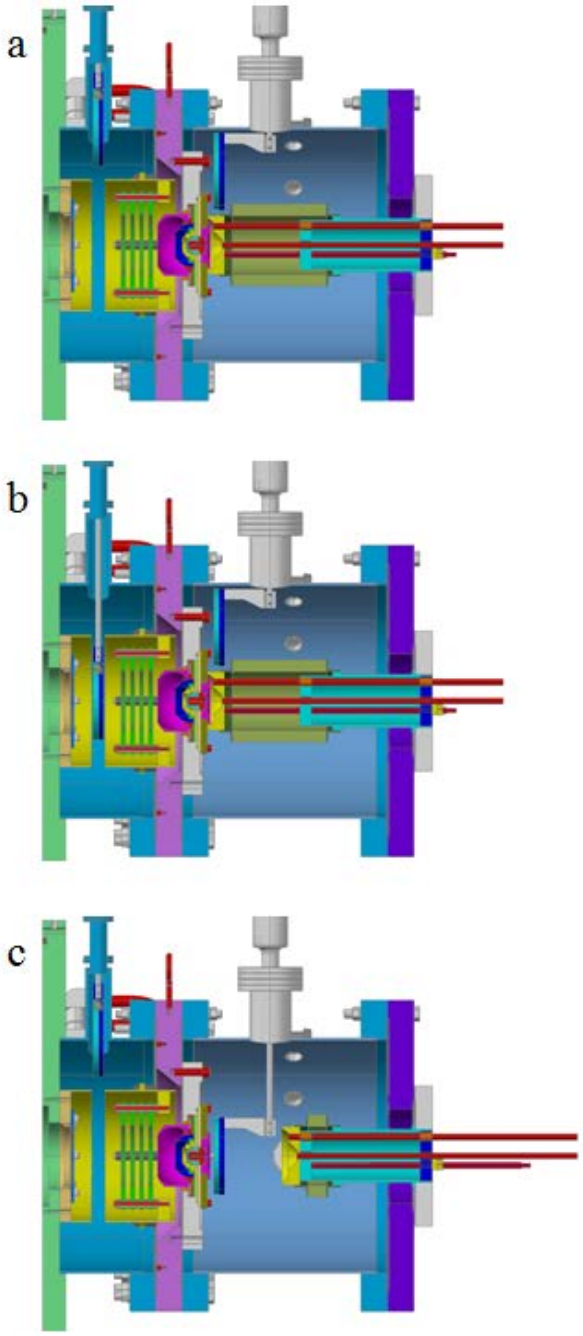

Figure 3-7. Three images depicting the detector system options of the RTC. (a) Both the AC and MC detectors are retracted, and the Aerosol Chamber is in place to transport ions to the chemistry experiment. (b) MC detector is in place to detect the incoming ions. (c) AC has been retracted so the AC detector can detect the ions exiting the Extraction Nozzle.

3.2 Offline Characterization

The inner diameter of the capillary between the outlet of the RTC and the vacuum has a large effect on the gas flow of the system. Twenty-five-foot-long capillaries with various inner diameters (1/16", 3/32", 1/8", and 5/32") were tested offline. As expected, the outlet flow rate increased with the inner diameter of the capillary (Table 3-2). However, for a pressure difference (DP) to be possible between the MC and the AC, the outlet flow rate had to be larger or equal to the flow rate across the extraction nozzle. Using a capillary with inner diameter of 1/16", the device could not sustain a high enough flow rate or maintain a constant DP. Moreover, as the outlet flow rate increased, the maximum possible DP also increased (Table 3-2). Maximum DP occurs when the flow rate across the extraction nozzle equals the outlet flow rate. The flow rate across the extraction nozzle directly correlates with the DP across the two chambers.

Table 3-2. Capillary inner diameter offline test

Capillary Inner Diameter (inches)	Maximum Measured DP (torr)	Measured Outlet Flow Rate (L/min)
1/16	0	<0.2
3/32	3.1	1.1
1/8	19	2.8
5/32	40	4.0

Offline characterization of the RTC efficiency was limited because it was not possible to emulate the stopped distribution of EVRs offline. However, as a proof-of-principle experiment, the performance of the RTC was tested with a ^{228}Th source.

Almost all recoils formed in the ^{228}Th source were neutral. However, a small amount of ^{220}Rn, a gaseous element, constantly emanated out of the source [94]. ^{216}Po ($t_{1/2}$ = 145 ms) [85] daughters from the emanated ^{220}Rn were produced in a positive charge state [95] and transported through the RTC. Offline, a thin metal disk was used in place of the aluminized Mylar RTC window; attached to the thin metal disk was a 2.5-cm metal cylinder which acted as a holder for the ^{228}Th source. The AC detector was used to measure the transmission of ^{216}Po recoils (Figure 3-8). Quantitative measurements could not be determined for the efficiency of the RTC because the ^{220}Rn emanation fraction could not be accurately measured. Measurement of the ^{220}Rn emanation fraction with the MC detector was tested. However, this measurement was not used because of the large uncertainties in the Rn collection efficiency of the MC detector.

SIMION simulation was used to determine the optimum voltage settings of the electrode system (Figure 3-3). The rate of ^{216}Po on the AC detector was monitored as the DP across the two chambers was varied. The electrode system was not varied during these experiments. It was discovered that from 0 to 10 torr, the rate of ^{216}Po on the AC detector increased; above 10 torr, the ^{216}Po rate remained constant. However, when DP was held constant and the inner diameter of the capillary was changed, the ^{216}Po rate remained constant. This suggested that the transmission across the Extraction Nozzle was dependent solely on DP and not outlet flow rate. During offline testing, it was also noted that the rate of ^{216}Po would decrease to barely above background levels when either the electrode system or gas flow was turned off. This was evidence that both gas flow and the electric field were needed to efficiently transmit the ions through the MC.

Even though the transportation time could not be measured directly, the transportation time had to be on the order of sub-seconds to transport the short-lived nuclei ^{216}Po. These offline experiments showed that this device could effectively transport heavy ions through the Extraction Nozzle to the AC.

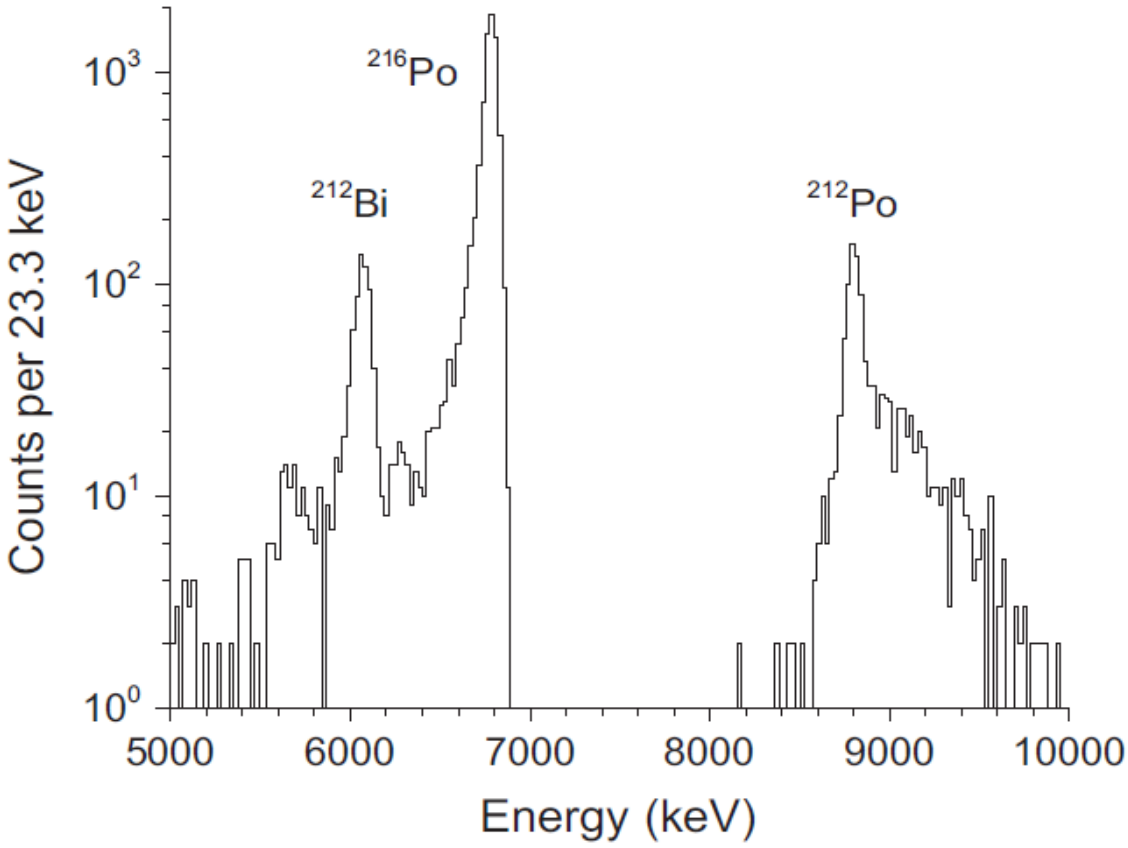

Figure 3-8. Sample AC detector spectrum from offline experiment.

3.3 Experimental Set-up of Online Characterization

The next step for the commissioning of the RTC was measuring the device's efficiency using a high-cross-section fusion evaporation reaction, ^{40}Ar(^{118}Sn, 6n)^{152}Er

[96]. A schematic of the online commissioning experiment is shown in Figure 3-9. The particle beam from the cyclotron first enters the target chamber—this is where the fusion evaporation reaction occurs between the accelerated ions and target atoms. The EVRs then travel through a physical separator, Momentum Achromat Recoil Separator (MARS), which removes beam particles and unwanted reaction products from the EVRs of interest. Then the EVRs are degraded by passing through a VAD and a RTC window and reach thermal energies in the RTC. Upstream of the RTC is a retractable position-sensitive silicon detector (PSSD), which made it possible measure the rate of EVRs at the end of MARS.

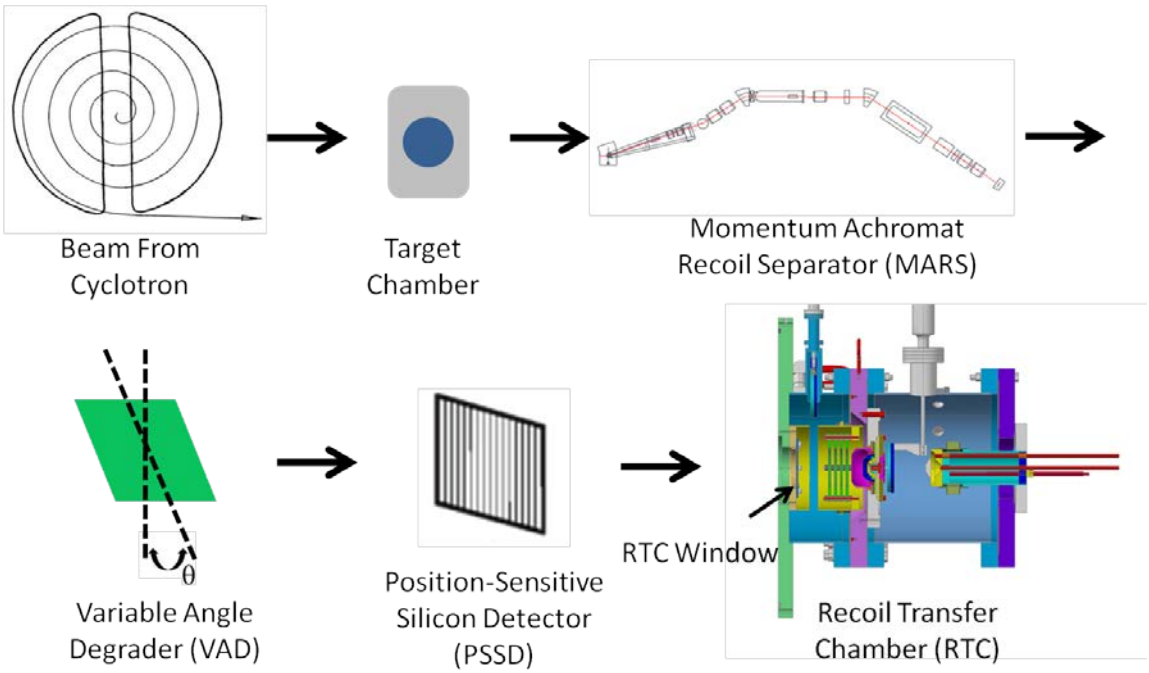

Figure 3-9. Schematic of online commissioning experiment.

3.3.1 Fusion Evaporation Reaction of Interest: ^{40}Ar(^{118}Sn, 6n)^{152}Er

The reaction ^{40}Ar(^{118}Sn, 6n)^{152}Er was chosen for the online characterization of the RTC for many reasons. It was critical that the production rate of the EVR be as high as possible. Optimization of the RTC was only possible if the error bars of the individual measurements were relatively small. The reaction ^{118}Sn(^{40}Ar, 6n)^{152}Er has a maximum cross section of ~100 mb [96-98] (relatively large for fusion evaporation reactions). This reaction was also advantageous since it used a gaseous beam that can be produced at significantly higher intensities than non-gaseous beams. ^{152}Er has a large alpha branch (~90%) [98], which was important since the EVRs were detected by silicon detectors. Lastly, the half-life of ^{152}Er (10.3 ± 0.1 s) [70] was suitable since the transportation time through the RTC was unknown. If gas flow alone were used to guide the ions through the device, the transportation time would be on the order of multiple seconds based on STAR-CCM+ simulations (Section 3.1.3). The gas-flow-only efficiency needed to be a measureable baseline to facilitate the electric field optimization, so the EVR produced needed to have a half-life on the order of multiple seconds. Once the gas-flow-only efficiency baseline was established, it was possible to determine whether the electric field changes were improving or hindering the device's efficiency.

3.3.2 Target Chamber

There are three target ladders in the target chamber (Figure 3-10). Each target ladder serves a different function in the production of EVRs. The accelerated ions first go through the degrader ladder, then the target ladder, and lastly the carbon stripper foil

ladder. A Faraday cup attached to the carbon stripper foil ladder monitors beam intensities in the target chamber. All three ladders are operated on remotely controllable telescoping arms; this makes it possible to quickly change the targets depending on the needs of the experiment.

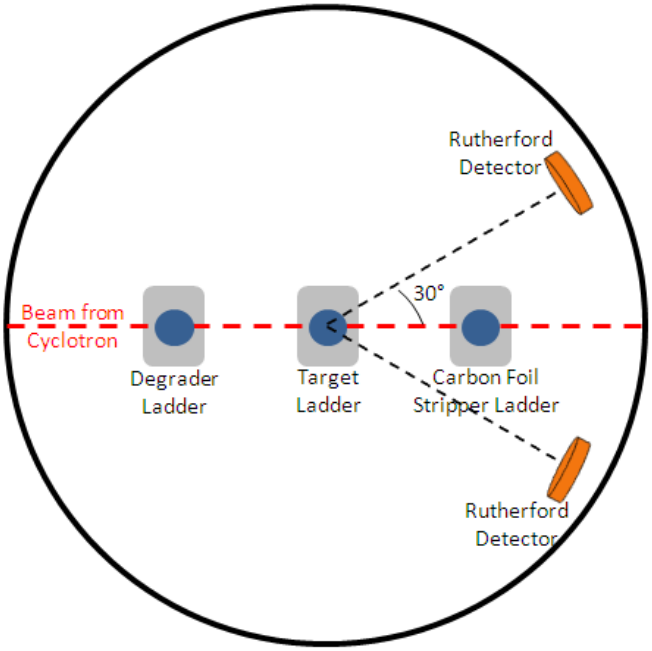

Figure 3-10. Schematic of target chamber.

The degrader ladder consists of multiple Al foils in a range of thicknesses (1.2–5.7 μm) that were used to degrade the beam's energy. This is necessary because the cross section of a fusion evaporation reaction is a function of beam energy but retuning the cyclotron is extremely time-consuming. These series of aluminum degraders make it

possible to degrade the beam up to ~25 MeV so that the excitation function can be scanned.

After exiting the degrader ladder, the beam passes through the target ladder. This ladder has a 97.06% enriched ^{118}Sn 315 μg/cm^2 target made by Microfoils Co. (Arlington, WA). The beam first passes through the target's backing, a 20 μg/cm^2 ^{nat}C foil that adheres the ^{118}Sn target to an Al target frame. After the degraded ^{40}Ar beam interacts with the ^{118}Sn, the resulting products and the unreacted beam particles pass through a 48 μg/cm^2 ^{nat}C foil. The ^{nat}C foil is used to equilibrate the EVRs' charge state distribution and improve the EVRs' transmission through the MARS (see Section 3.3.4 for discussion on MARS).

3.3.3 Rutherford Detectors

The EVR production rate, *P* (nuclei per unit time), for a specific reaction is the product of the reaction's cross section, σ (unit area per nuclei), beam intensity, *I* (particles per unit time), and the areal density of the target, N_t (target nuclei per unit area) [99].

$$P = \sigma I N_t \qquad \text{Eq. 3.1}$$

This equation assumes that *I* and *N* are constant. However, throughout a beam experiment, *I* can fluctuate significantly due to ion source and accelerator performance. Also the intense beam may cause the target to sputter, decreasing N_t. Before the number of observed EVRs between different detectors can be compared for efficiency calculations, they must be normalized to detector efficiency, the beam dose (integral of *I* over time of run), and average N_t during the run.

Rutherford scattering, also known as Coulomb scattering, makes it possible to account for fluctuations in both I and N_t throughout the online commissioning experiment. The high nuclear charge of the target nucleus will deflect the beam nuclei in a large range of angles [99]. The number of observed Rutherford scattering events in a specific run is a product of the Rutherford scattering cross section, the fraction of space subtended by the collimator, beam dose, and average N_t during the run. The Rutherford scattering cross section at a specific angle, θ, can be determined by Equation 3.2 [99]:

$$\frac{d\sigma_{Ruth}}{d\omega} = \left[\frac{e^2 Z_p Z_t}{4\pi\varepsilon_0(2E_p)}\right]^2 \frac{1}{\sin^4\theta} \cdot \frac{[\cos\theta + \sqrt{1-(m_p/m_t)^2\sin^2\theta}]^2}{\sqrt{1-(m_p/m_t)^2\sin^2\theta}} \qquad \text{Eq. 3.2}$$

This equation is only true when the mass of the projectile, m_p, is less than mass of the target, m_t, which was the case for the ^{40}Ar(^{118}Sn, 6n)^{152}Er reaction. Z_p and Z_t are the atomic number of the projectile and target nuclei and Ep is the kinetic energy of the beam in the lab frame. The rate of observed Rutherford scattering events makes it also possible to monitor the beam intensity during a run, since fluctuation in N_t for most targets tend to be small in comparison to fluctuation in I.

During the online characterization of the RTC, two silicon detectors were used to detect the deflected projectile nuclei. These two detectors were located in the target chamber, ±30° to the beam axis and 241 mm from the stationary target (Figure 3-10). These detectors were known as Rutherford East and West. Cylindrical tubes made of Delrin (21.6 mm long with a 6.1-mm-diameter hole) were placed in front of the detector to reduce the background of unwanted scattering events. A 1-mm-diameter collimator

was placed directly upstream of each detector to decrease the rate of deflected beam nuclei.

The Rutherford scattering detectors were also used to monitor beam alignment on the target. Due to the transfer of momentum, the spatial distribution of the EVRs when exiting the target chamber is directly affected by beam alignment, and MARS' transmission is sensitive to the spatial distribution of the EVRs. It is assumed in RTC efficiency calculations that the transmission of MARS is constant. The alignment of the beam on the target was controlled by a dipole magnet (BLD1) immediately upstream of the target chamber. Small fluctuations in BLD1 would cause the beam to go off axis. When the beam is on axis, the ratio between the events observed in the Rutherford East and West detectors is 1. This ratio changes when the beam drifts off axis. During the RTC online commissioning experiment, the ratio between the events observed in Rutherford East and West was given a tolerance of ± 0.1. It has been estimated that the beam would have to move > 2 mm off axis to see a change in the Rutherford ratio > 0.1. During the online experiment it was measured that a ±0.5% change in BLD1 setting would cause the Rutherford ratio to be outside of the tolerance of ± 0.1. When the Rutherford ratio was outside of the accepted range BLD1 was adjusted to minimize the transmission fluctuations of the MARS.

The Rutherford scattering cross section and the fraction of space subtended by the collimator were constant throughout the entire online commissioning experiment. Therefore, differences in both beam dose and the average N_t during different runs could

be accounted for by normalizing the number of observed ^{152}Er events to the number of observed Rutherford scattering events.

3.3.4 MARS: Physical Separator

At the Cyclotron Institute, MARS was used to separate the EVRs from the unwanted reaction products and unreacted beam particles. MARS employs both a magnetic rigidity filter and a velocity filter (also known as a Wien filter) to isolate the EVRs [100]. A schematic of MARS can be seen in Figure 3-11. Unique abbreviations, D1-3 and Q1-5, are given to the individual dipole and quadrupole magnets, respectively. The abbreviations SL1-4 is given to the individual movable slits in MARS. These slits can be used to decrease the acceptance of the separator at various locations. For a majority of the RTC commissioning experiment all the slits were wide open.

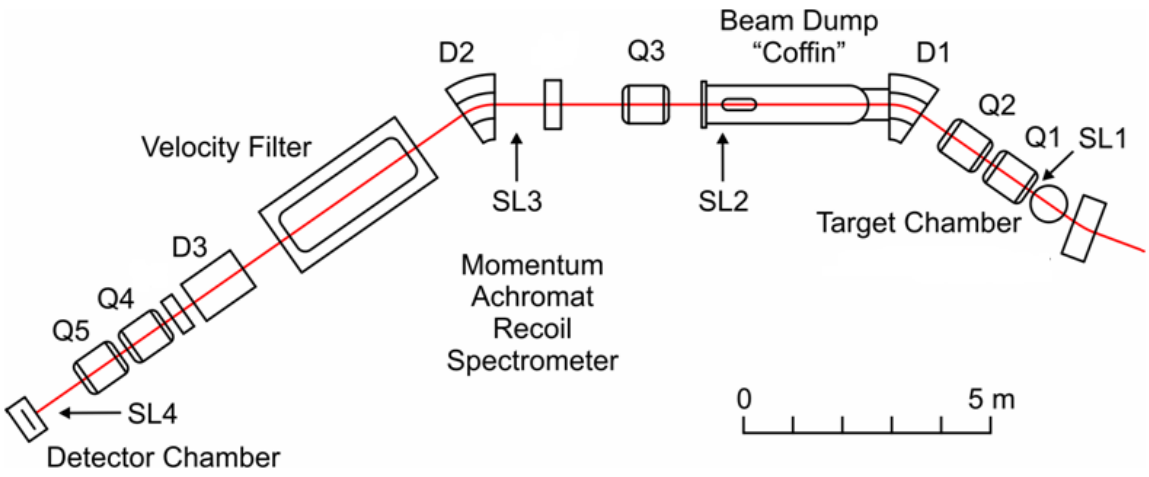

Figure 3-11. Schematic of Momentum Achromat Recoil Separator (MARS). Figure from Nucl. Instr. Meth. Phys. Res. A [100].

After the target chamber, the resulting product will first pass through Q1 (which focuses particles in the vertical direction) and then Q2 (which focuses particles in the horizontal direction); these magnets are used to focus particles into the magnetic rigidity filter [100]. Both magnetic rigidity filters and velocity filters work under the principle of the Lorentz Force Law, which describes the force on a charge particle moving through an electric and magnetic field:

$$\vec{F} = q(\vec{E} + \vec{v} \times \vec{B}) \qquad \text{Eq. 3.3}$$

where $\vec{F}$ is the force vector on the particle, q is the charge of particle, $\vec{E}$ is the electric field vector, $\vec{v}$ is the velocity vector, and $\vec{B}$ is the magnetic field vector. Magnetic rigidity filters do not use an electric field, and the magnetic field is perpendicular to the trajectory of a charged particle. Therefore, in scalar terms, this equation simplifies to $F=qvB$, and this force will cause the particles' trajectory to curve. The radius of this curve can be calculated by using the centripetal force equation:

$$F = \frac{mv^2}{\rho} \qquad \text{Eq. 3.4}$$

where v is velocity of the particle, m is mass of the particle, and ρ is the radius of curvature of motion. These two equations can be combined to give $B\rho = mv/q$, the magnetic rigidity of a particle is its momentum, mv, divided by charge, q.

In a magnetic rigidity filter, the radius of curvature is a characteristic of the magnet's design and B. The magnetic field strength is set to accept the expected magnetic rigidity of the EVRs. It is important to note that the EVRs exit the target

chamber in a range of different charge states and velocities. The LISE++ program is used to determine the most probable magnetic rigidity of the EVRs.

MARS D1 and D2 both have a radius of curvature of 1.116 m and are both set to the same magnetic field strength [100]. In between the two magnets is a Beam Dump "Coffin." This is one of two dispersive planes that allows for the particles with different magnetic rigidity to spread out spatially. The magnetic rigidities of the beam particles are significantly different than the EVR of interest and a majority will collide with the Beam Dump Coffin. The remaining particles go through Q3 (which focuses horizontally) and then are subjected to another magnetic rigidity filter, D2, before entering the velocity filter [100].

The velocity filter uses crossed electric and magnetic fields to select ions of a specific velocity. The EVRs will follow a straight path through the velocity filter if the net force, $\vec{F}$, of the electric field and the magnetic field is equal to zero. Therefore, in scalar terms, Equation 3.3 can be simplifies to $v = E/B$. The velocity filter is set to accept the most probable velocity of the EVRs, the trajectory of all ions where $v \neq E/B$ curve away from the EVRs and they will implant the walls of the filter.

In our experiments, the system downstream of D3 was on adjustable arm set to 5°. Thus, after the velocity filter, the remaining particle beam was bent up by D3. Lastly, Q4 (which focused vertically) and Q5 (which focused horizontally) were used to focus as much of the EVR distribution as possible on a PSSD in the Detector Chamber. This detector was placed directly in front of the entrance of the RTC and was used to monitor the alignment of the product into the RTC.

Before 2009, MARS had been used in experiments to select ions in the range of 8% to 30% of the speed of light. Fusion evaporation reactions produce EVRs at much lower velocities, in the range of 1.5% to 2% of the speed of light. The velocity filter in MARS had to be calibrated for this lower velocity [101]. This was done offline using an alpha source, ^{241}Am, to simulate the products of a beam experiment. Aluminum degraders of various thicknesses (0, 6.1, 12.3, and 18.4 μm) were used to decrease the velocity of the alpha particle to 5.33%, 4.92%, 4.20%, and 3.20% of the speed of light, respectively. For the different velocities of alpha particles, the optimum electric and magnetic field settings were determined for the MARS velocity filter. This was done by first turning off the velocity filter and tuning the rest of MARS for the maximum alpha rate on the PSSD at the end of MARS. Next the velocity filter was turned on, the electric field was set to a constant value and the alpha rate on the PSSD was maximized by changing the magnetic field setting. This was repeated for a total of five different electric field settings. The complete process was repeated for the four alpha particle velocities.

Additionally, MARS transmission was optimized and measured for EVRs using the reactions ^{118}Sn(^{40}Ar, 6n)^{152}Er and ^{165}Ho(^{40}Ar, 6n)^{199}At [101]. All the magnetic settings in MARS were systematically scanned and the rate on the PSSD at the end of MARS was maximized. The transmission of MARS was determined to be between 2% and 4%, depending on the kinematics of the reaction. A beam rejection factor of $\gtrsim 10^{15}$ was also measured [101].

MARS was also used at the beginning of the RTC online commissioning experiment to characterize the beam and targets. The beam energy was determined by measuring the magnetic rigidity of the beam's charge states after passing it through a 48-$\mu g/cm^2$ ^{nat}C foil. The beam energy was corrected for the energy loss through a 48-$\mu g/cm^2$ ^{nat}C foil by using SRIM. The thickness of each individual Al degrader and stationary target was then confirmed by measuring the energy loss of the beam.

The ^{40}Ar beam for the online commissioning experiment had 220 MeV of energy, while the $^{40}Ar(^{118}Sn, 6n)^{152}Er$ excitation function peaked between 200 to 205 MeV [96]. A 4.5-μm Al degrader was used to degrade the beam to 205 MeV. Based on LISE++ simulations, ^{152}Er entered MARS with 43.0 MeV of kinetic energy with a charge state of +20, and MARS was set accordingly to maximize the transmission of ^{152}Er.

3.3.5 Detector Chamber

After MARS separated the EVRs from the unwanted reaction products and unreacted beam particles, the remaining particles entered the detector chamber. During the RTC online commissioning experiment, the ions then passed through a rotating Mylar degrader and implanted onto a retractable X1 design 16-strip PSSD (purchased from Micron Semiconductor Ltd) in the detector chamber. The rotating degrader was set to 0° when the PSSD was in place. This detector had an active area of 50 mm X 50 mm and a thickness of 300 μm.

The energy signal of the implanted ions was recorded from the back of the detector along with the alpha-decay of the EVRs. Each individual strip had a width of

~3 mm and would give the horizontal location of the event. An additional energy signal was measured from the top of the individual strips. Thus, the vertical location of the event could be determined through resistive charge division.

The energy calibration of this detector was acquired using a four-peak α source that contained a mixture of ^{148}Gd, ^{239}Pu, ^{241}Am, and ^{244}Cm with an activity of ~10 nCi each. The resulting alpha-energy spectrum had alpha peaks with 70 to 80 keV full width half maximum. The vertical position calibration of the individual strips was determined using the same source and an aluminum mask with multiple horizontal slits that were 1 mm wide and spaced 8 mm apart vertically.

The PSSD detector was located about ~10 cm upstream of the RTC and was centered with the RTC window. The incident rate and spatial distribution of the EVRs into the RTC was optimized using the PSSD. Based on SIMION simulations, the incoming product distribution needed to be centered with the RTC window and spatially focused. D3 was used to center the product beam vertically, while Q4 and Q5 were used to decrease the size of the spatial distribution.

3.4 Results of Online Characterization

The primary goal of the online experiment was to optimize the efficiency of the RTC. To do this, it was critical to understand how ions were transmitted through each stage of the device. The first stage of ion transmission was from the PSSD (end of MARS) to the MC detector (entrance of the RTC), and the second stage was from the MC detector (entrance of the RTC) to the AC detector (outlet of the RTC). Before the ^{152}Er rate, *R*, on different detectors could be compared, they had to be normalized to the

alpha detection efficiency, ε_α, of the particular detector and the rate of Rutherford scattering events, R_{ruth}, measured during that particular run (see Section 3.3.3). The equation to determine the normalized ^{152}Er rate R' is:

$$R' = \frac{R}{\varepsilon_\alpha R_{ruth}} \qquad \text{Eq. 3.5}$$

The EVRs detected by the PSSD and the MC detector were not completely thermalized and implant with a non-negligible energy. Equation 3.6 [102] shown below can be used to estimate ε_α for EVRs that implant into the silicon detector.

$$\varepsilon_\alpha = \frac{1}{2}\left(1 + \frac{r_{EVR}}{r_\alpha}\right) \qquad \text{Eq. 3.6}$$

which depends on the implantation depth of the EVRs, r_{EVR}, and range of the emitted alpha particles, r_α. In general the range of the alpha particles is considerably greater than that implantation depth of the EVRs [102]. Therefore, even for implanted EVRs there is a high chance that alpha particles emitted away from the detector will escape before depositing their full energy into the detector (i.e. not be detected). ^{152}Er emits a 4.8 MeV alpha particle which has a SRIM estimated range in Si of ~23 μm [70, 82, 83]. The 43 MeV EVRs passed through the ~6μm mylar VAD at 0° and implanted into the PSSD with ~14 MeV of energy, corresponding to a SRIM estimated range in Si of ~3.7 μm [82, 83] and an ε_α of ~0.58. The EVRs that implant onto the MC detector had between 0 and 8 MeV of energy (depending on the angle of the VAD), corresponding to a SRIM estimated range in Si of 0 to ~2.3 μm [82, 83] and an ε_α of 0.5 to 0.55. These SRIM range calculations and corresponding ε_α do not include the effect of the momentum spread of the EVRs from MARS, so ε_α for both the PSSD and the MC detector was

estimated to be 55 ± 3%. In contrast, thermalized EVRs have a ε_α of 0.5 because they will sit on the surface of the silicon detector and 50% of the alpha particles will be emitted into the detector and deposit their full energy (i.e. be detected). The other 50% of the alpha particles will be emitted in the opposite direction of the detector and will not be detected. This is the case for the EVRs detected by the AC detector.

3.4.1 Stage One Results

The transmission of ions from the PSSD to the MC detector was useful for understanding the trajectory and spatial distribution of the EVRs entering into the RTC. This information was needed to determine the fraction of ions that enter the RTC that implant into the MC detector, f_{MC}. All of the measurements described in this section were taken with the VAD set at 0° (perpendicular to the beam) and the RTC evacuated ($P_{MC} \approx 0$ torr).

The rate on the MC detector can be modeled as the product of several factors:

$$R'_{MC} = R'_{PSSD} f_{screen} f_{grid} f_{holder} f_{MC} \qquad \text{Eq. 3.7}$$

As previously discussed, R'_{MC} and R'_{PSSD} are determined by Equation 3.5. In Equation 3.7, f_{screen} is the fraction of ions that pass through the "protector screen," f_{grid} is the fraction of ions that pass through the honeycomb RTC window support grid, and f_{holder} is the fraction of ions that are not geometrically blocked by the window holder.

The product of f_{screen} and f_{grid} was measured by closing SL4 (slits 4) in MARS to ±0.5 cm and comparing R'_{MC} and R'_{PSSD}. For this particular measurement, it was assumed any ^{152}Er that reached the PSSD would also implant into the MC detector, so f_{holder} and f_{MC} both equaled 1. This was considered a true assumption was based on the

measured spatial distribution of ions on the PSSD. The product of f_{screen} and f_{grid} was measured at 71 ± 6%. This corresponded to the product of the geometric transparency of f_{screen}, 88% and f_{grid}, 81% ($f_{screen}f_{grid}\approx$ 71%).

Next, the product of f_{holder} and f_{MC} was measured. This was done by comparing R'_{MC} and R'_{PSSD} with the SL4 in MARS fully open. During normal operation of the RTC, SL4 in MARS was fully open to maximize the rate of ^{152}Er. Since all other factors in Equation 3.7 had been measured, the product of f_{holder} and f_{MC} was measured at ~87%. This loss was due to the product beam expanding as it traversed the distance between the PSSD and the MC detector. This is consistent with the previous experiment with SL4 closed to ± 0.5 cm, which showed the product beam expanded spatially as the ions traversed from SL4 to the PSSD. The measured spatial distribution of ions on the PSSD was used to simulate what "product beam expansion" would cause a 13% loss from the PSSD to the MC detector. Based on this simulation, it was determined that f_{holder} was 99^{+1}_{-4}% and f_{MC} was 88 ± 4%. These results are consistent with the fact that the diameter of the window holder is 6 cm but the diameter of the MC detector is only 5 cm.

3.4.2 Stage Two Results

The main characterization of the RTC took place in stage two, the ion transmission measurements between the MC detector and the AC detector. Both the electrode settings and gas flow settings were optimized. Also, by using the VAD, the location of the stopped distribution could be moved to better understand how the RTC worked. The effective thickness of the rotating degrader increased with its angle, moving the stopped ^{152}Er distribution closer to the RTC window.

Based on SRIM energy loss calculations, it was determined that a VAD thickness of ~6 μm plus the 2-μm aluminized Mylar RTC window would be sufficient to stop 43.0 MeV ^{152}Er in 2.5 cm of 228 torr He. The actual thickness of the VAD was 5.9 ± 0.1 μm with an estimated error on its angle of ± 1°. The VAD effective thickness changed with the reciprocal of the cosine of its angle. The RTC window was 2.0 ± 0.1 μm Mylar plus 32 ± 16 nm of Al on both sides. The total degrader thickness was the sum of the VAD effective thickness and RTC window thickness.

Two different extraction efficiencies were determined for the RTC. One was the measured efficiency, ε_{RTC}, the ratio between the rate of ^{152}Er entering the RTC window versus the rate detected on the AC detector. The second was the corrected efficiency, ε'_{RTC}, that could be theoretically achieved if no ^{152}Er were lost by thermalization in the RTC window. The two equations that were used to determine the two different efficiency of the RTC as a function of VAD angle, θ, were:

$$R'_{AC}(\theta) = \frac{R'_{MC}(0°)}{f_{MC}}\varepsilon_{RTC}(\theta) \qquad \text{Eq. 3.8}$$

$$R'_{AC}(\theta) = \frac{R'_{MC}(\theta)}{f_{MC}}\varepsilon'_{RTC}(\theta) \qquad \text{Eq. 3.9}$$

Both R'_{MC} and R'_{AC} are determined by Equation 3.5 and are dependent on the VAD angle, θ. Figure 3-12 shows example energy spectra of EVRs on the two detectors. Again, f_{MC} is the fraction of ^{152}Er that enters the RTC and is detected by the MC detector.

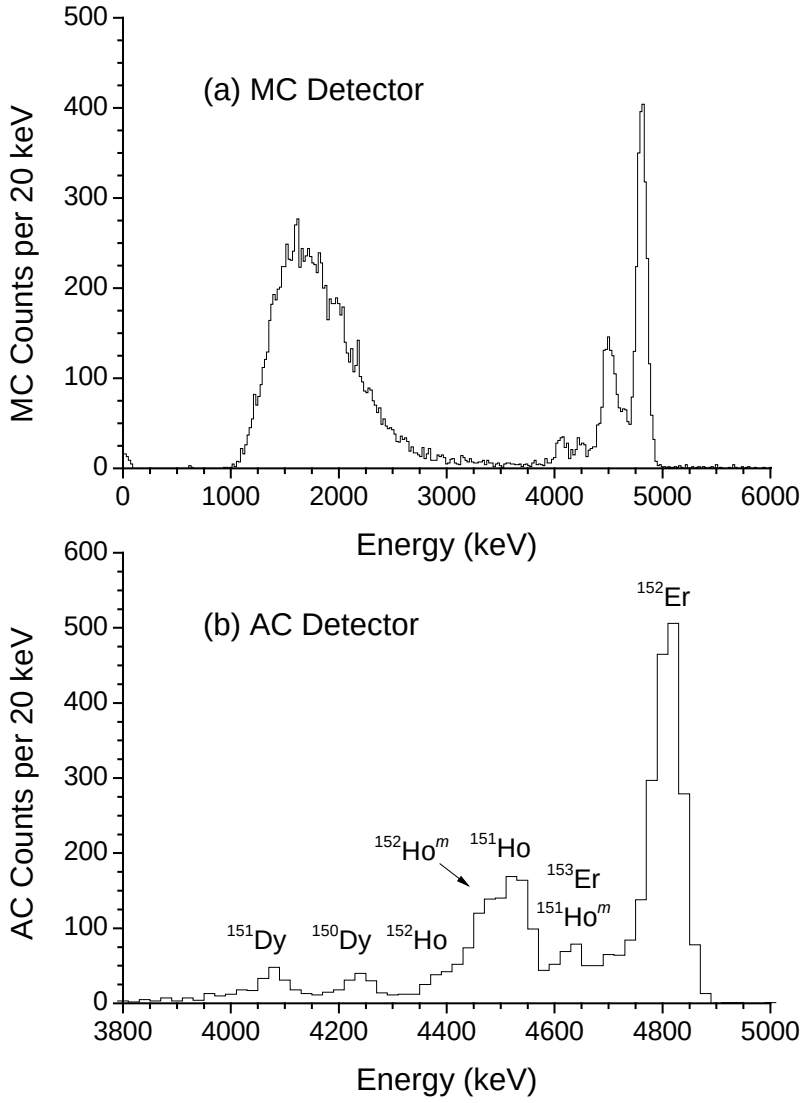

Figure 3-12. Sample MC and AC detector spectra from online experiments. (a) Energy spectrum observed on the MC detector with a total degrader thickness of 10.3 ± 0.2 µm (VAD at 45°). The broad peak at 1000-3000 keV is due to the implanting EVRs and target-like fragments. (b) Alpha spectrum observed on the AC detector. As expected the implant EVRs and target-like fragments are not observed in the AC detector.

All measurements of R'_{MC} were taken with the RTC evacuated ($P_{MC} \approx 0$ torr). In Equation 3.8, it was assumed that no ions stopped in the window when $\theta = 0°$. This was assumed because $R'_{MC}(\theta)$ was flat until $\theta > 30°$. All measurements of R'_{AC} were taken with P_{MC} = 228 torr; the effect of varying the gas flow and electrode system setting was quantitatively measured by the AC detector.

After R'_{MC} was measured at various VAD angles, the online characterization of the RTC began with the electric field turned off. Only gas flow transported the ions to the AC detector. Based on results from offline measurements (Section 3.2), the DP was set to 10 torr and the outlet flow rate was set to 2.5 L/min. The rate was then maximized on the AC detector by varying the VAD angle (shown in red in Figure 3-13a), and the maximum rate was measured at θ=45°.

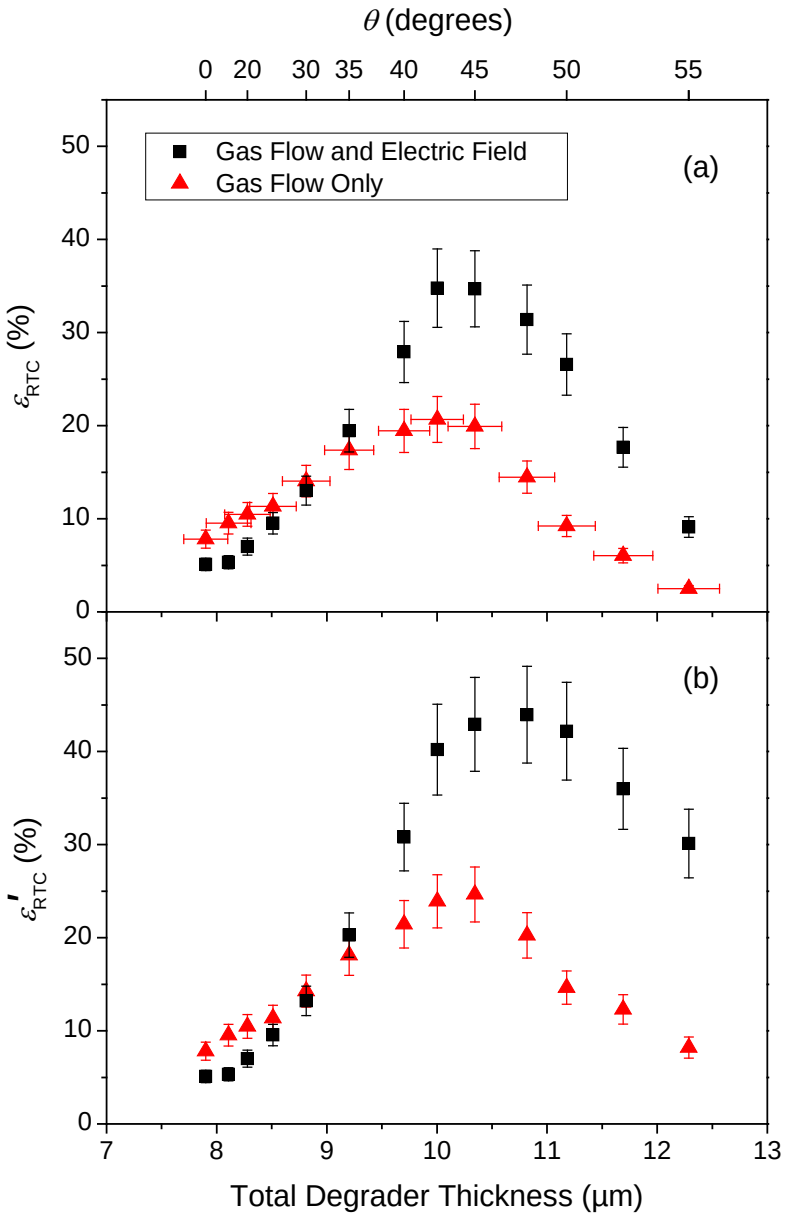

Figure 3-13. Extraction efficiency of the RTC as a function of the degrader thickness. The RTC was run in two different modes: gas flow only (shown in red) and gas flow and electric field (shown in black). (a) Efficiencies calculated by Eq. 3.6. (b) Efficiencies calculated by Eq. 3.7.

Then the electric field was turned on, while the gas flow and VAD angle were not changed. The electrode settings determined in SIMION were used as a starting point (Figure 3-3). The rate of ^{152}Er that implanted on the AC detector dropped to zero. All the SIMION electrode settings were decreased by a factor of ~3, a potential gradient across the entire device of ~150 V, and a measurable rate of ^{152}Er was detected on the AC detector. This allowed for the individual electrode settings to be optimized systematically. After R'_{AC} was maximized, it was concerning that the rate with the electric field on was lower than that with gas flow only. Again, all the electrode settings were decreased by various factors. It was discovered that a potential gradient of ~20 V across the entire RTC gave the maximum ^{152}Er rate on the AC detector. This was at least a 50% increase over the gas-flow-only rate (Table 3-3). When the potential gradient of across the whole RTC was changed to ~10 V, the rate of ^{152}Er decreased by ~20% (Table 3-3). The results of this entire process were surprising; further discussion can be found in Section 3.5.

Table 3-3. Efficiencies and transportation times for various electrode system settings. The highest ε'_{RTC} was measured with a potential gradient of ~20 V. In all experiments the VAD angle was 45°, DP was 10 torr, and the outlet flow rate was 2.5 L/min. Calculation of transportation time, τ_{RTC}, is discussed in section 3.4.4.

Electrode Name	Electrode Potential (V)				
Inner Chamber	0	11.0	21.6	42.4	83.8
Ring 1	0	10.8	21.6	42.4	83.8
Ring 4	0	10.4	21.6	42.4	83.8
Flower 1	0	10.0	21.6	40.0	80.0
Flower 2	0	7.6	15.0	30.0	60.2
Flower 3	0	4.4	9.6	19.4	39.4
Flower 4	0	2.2	4.8	9.8	19.8
Nozzle	0	2.2	4.8	9.8	19.8
ε'_{RTC} (%)	25 ± 3	35 ± 4	43 ± 5	39 ± 5	33 ± 4
τ_{RTC} (s)	8.5 ± 1.0	7.2 ± 2.4	6.9 ± 0.6	8.1 ± 1.9	2.2 ± 1.2

Results for the extraction efficiency as a function of degrader thickness are shown in Figure 3-13. The RTC was run under two different modes during these measurements. One mode used only gas flow to transport the ions through the AC detector, referred to as "gas flow only." The other mode used both gas flow and the optimum electrode system settings (Table 3-3) to transport the ions through the AC detector, referred to as "gas flow and electric field." The maximum measured extraction efficiencies were 21 ± 3% (gas flow only) and 35 ± 4% (gas flow and electric field) (Figure 3-13a). When the total degrader thickness was greater than 9 μm of Mylar (VAD $\theta > 30°$), ^{152}Er started to thermalize before reaching the end of the RTC window, and extraction efficiencies were corrected accordingly (Eq. 3.7, Figure 3-13b). The maximum corrected extraction efficiencies were 25 ± 3% (gas flow only) and 44 ± 5% (gas flow and electric field).

These results suggest that ions thermalized too far into the device are defocused by the electric field, since extraction efficiency decreases with the addition of electric field at a degrader thickness less than 9 μm of Mylar (Figure 3-13). Furthermore, the broadening of the "gas flow and electric field" results is evidence that the electric field can compensate when the ions stop too close to the window for the gas flow to be most effective. The results are consistent with the SIMION simulations; the electric field works best when the ions stop closer to the RTC window, and the highest efficiencies are measured at large VAD angles. However, this also suggests that the stopped distribution of the ^{152}Er in the RTC is too wide, since at large VAD angles a significant portion of the ^{152}Er are trapped in the RTC entrance window. If the pressure in the RTC were increased, then the width of the stopped distribution could be decreased, which would likely lead to higher extraction efficiency. Increasing the device's pressure will be investigated in future experiments with the device.

3.4.3 Gas Flow Online Characterization

After the electrode system settings and the VAD angle were optimized, the gas flow settings were investigated. The effects of DP and outlet flow rate on efficiency were studied. As previously discussed, both electric field and gas flow play a vital role in the transportation of the ions through the RTC. Figure 3-14 shows the corrected efficiency as a function of DP. Similar to the offline measurements (Section 3.3), there is a significant decrease in the RTC's efficiency with a DP less than 10 torr, and the efficiency seems relatively constant with DP greater than or equal to 10 torr. There may

be a maximum efficiency around a DP of 15 torr; however, the error bars of these measurements are too large to definitively make that statement.

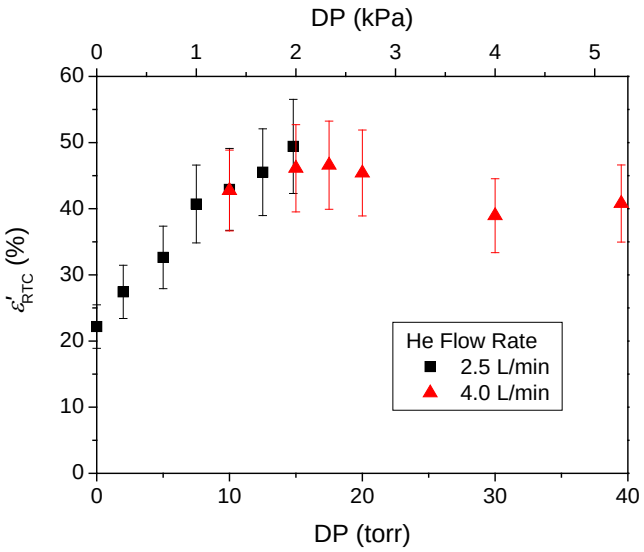

Figure 3-14. Corrected efficiency, $\boldsymbol{\varepsilon'_{RTC}}$, as a function of DP. Two different outlet flow rates were tested, 2.5 L/min (black squares) and 4.0 L/min (red triangles).

It is also interesting that the efficiency seems to be unaffected by the outlet flow rate; the two curves from the different outlet flow rates overlap very well with each other. The same observation was made in offline DP measurements. Also, the shape of the curve in Figure 3-14 is qualitatively similar to Figure 4 by J. Evens *et al.* [26], which plots efficiency as a function of flow rate for a traditional "gas flow only" RTC. This seems to confirm the hypothesis that flow rate across the Extraction Nozzle is controlled by the DP between the two chambers and is unaffected by outlet flow rate.

Figure 3-15 shows the corrected efficiency as function of outlet flow rate with the DP held at a constant 10 torr. These results again show that the RTC's efficiency is

constant at 43 ± 2%, regardless of the outlet flow rate. (The outlet flow rate is a sum of the flow rate across the Extraction Nozzle and the flow rate across the AC inlet.) If DP is held constant, the flow rate through the Extraction Nozzle is also constant. Therefore, when the DP is held constant and the outlet flow rate is increased, the additional flow comes from the AC inlet.

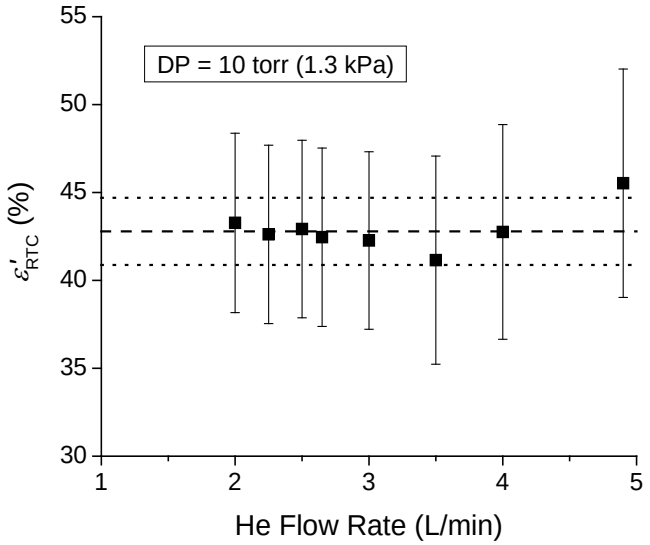

Figure 3-15. Corrected efficiency, $\boldsymbol{\varepsilon'_{RTC}}$, as a function of outlet flow rate. DP was set to 10 torr during these measurements. The dashed line represents the weighted average value, and the dotted lines represent the 1σ confidence interval. A DP of 10 torr was not possible with an outlet flow rate < 2.0 L/min.

3.4.4 Transportation Time Correction

The online transportation time of the ions from the entrance of the RTC window to the AC detector was also measured. Offline measurements (Section 3.3) showed evidence that the transportation time was less than 1 second. However, offline, the

potential gradient difference the RTC was more than 20 times larger than in the online experiment. It was expected that ions travel faster in an RTC with a larger potential gradient difference.

The time distribution of ^{152}Er events on the PSSD shows an ingrowth of ^{152}Er the moment the beam hit the target because the transportation time through MARS is negligible. This, however, is not the case for the AC detector. The time distribution of ^{152}Er events on AC detector will change with the RTC's transportation time. In particular, the ingrowth curve of ^{152}Er will be shifted in time due to the transportation time of the RTC. The equation below can be used to describe how the time distribution, *N(t)*, of a ^{152}Er events would change with the RTC's transportation time, τ_{RTC} [103]:

$$N(t) = \frac{\varepsilon P}{\lambda + \tau_{RTC}^{-1}} \{1 - e^{[-(\lambda + \tau_{RTC}^{-1})(t - \tau_{RTC})]}\} \qquad \text{Eq. 3.10}$$

In this equation ε is the product of the efficiency for the transmitting ions from the target chamber to the AC detector and the alpha detection efficiency of the AC detector, *P* is the production rate of ^{152}E determined by Equation 3.1, and λ is the decay constant of ^{152}Er. Equation 3.9 is only true for time $t > \tau_{RTC}$, because at $t < \tau_{RTC}$ the freshly made ^{152}Er has not had enough time to travel through the RTC and reach the AC detector. To determine τ_{RTC}, the time distribution of ^{152}Er events on the AC detector was fitted using Equation 3.10.

The results of this analysis for various electrode system settings are shown in Table 3-3. As expected, the transportation time decreased with increasing potential gradient across the RTC. However, the overall efficiency of the device decreased with

potential gradients greater than or equal to 22 V, indicating that the effectiveness of the electric field decreased.

A transportation time of multiple seconds is detrimental to the transportation of ^{152}Er, which has a half-life of 10.3 s. Theoretically, if this device were used to transport EVRs with longer half-lives, higher extraction efficiencies could be achieved. To determine this theoretical maximum efficiency, ε''_{RTC}, the measured efficiencies needed to be corrected for the fact that ^{152}Er decayed while traveling through the RTC to the AC detector. Equation 3.11 was used to determine the theoretical maximum efficiencies:

$$\varepsilon''_{RTC} = \varepsilon'_{RTC} e^{+\lambda \tau_{RTC}} \qquad \text{Eq. 3.11}$$

A transportation time of 6.9 ± 0.6 s was measured for the optimum electrode system settings (Table 3-3), which gives a theoretical maximum efficiency of 70 ± 9%.

3.5 Additional Simulations and Offline Characterization

The discrepancy between the online electrode system and the offline electrode system warranted further investigation. Therefore, offline characterization with the ^{228}Th source was revisited.

As discussed previously, an electroplated source with an active diameter of 5 mm does not emulate the spatial distribution of thermalized EVRs in a RTC very accurately. Therefore, an experiment was performed where the rate of ^{216}Po on the AC detector was measure as the source was moved within the MC both on and off the central axis. The results showed that the rate of ^{216}Po on the AC detector was significantly dependent on the source location (Figure 3-16); the transmission of ^{216}Po decreased by over 50% when the source was moved off axis by only 1 cm. The rate of ^{216}Po was less affected when

the source was moved along the central axis. However, as expected from SIMION simulations, the maximum transmission occurred when the source was placed 0.25 cm to 2.5 cm away from the window.

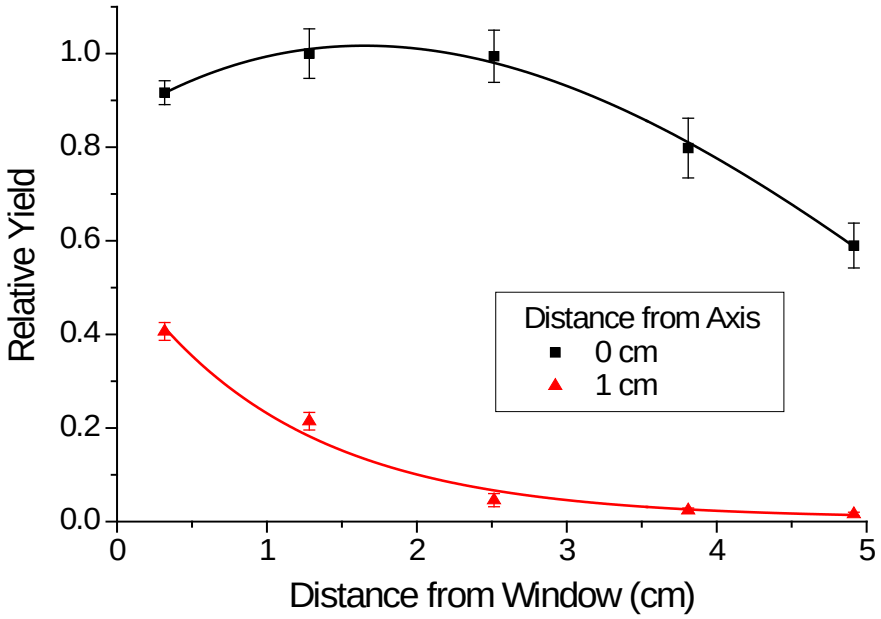

Figure 3-16. Yield of $^{216}Po^{+}$ from a ^{228}Th source as a function of position within the RTC. All yields are representative has relative yield to the maximum measured yield. The maximum yield was measured when the source was located on axis and 2.5 cm from the RTC window. Black squares are the results when the source was on axis. The red triangles are the results when the source was 1 cm off axis. The lines are drawn to guide the eye.

The optimum offline settings were simulated using SIMION to determine why the transmission of ^{216}Po was very sensitive to source position. An electric field diagram of the offline electrode setting is shown in Figure 3-17a. A grid of thermalized $^{216}Po^{+}$ ions with 5-mm spacing was simulated in SIMION to better understand the "effective

volume" of the MC (Figure 3-17b). The black squares are ions that reached the entrance to the nozzle and blue triangles are ions that reached flower petal 4. The ions with the highest probability of being extracted are shown as black squares. The effective volume of the MC is a narrow region along the center axis of the RTC, which corresponds with offline source measurements (Figure 3-16). Ions that stop along the center axis of the RTC have a high chance of being extracted, while ions that stop slightly (~1 cm) off axis do not. Using these settings would give poor extraction in an online experiment.

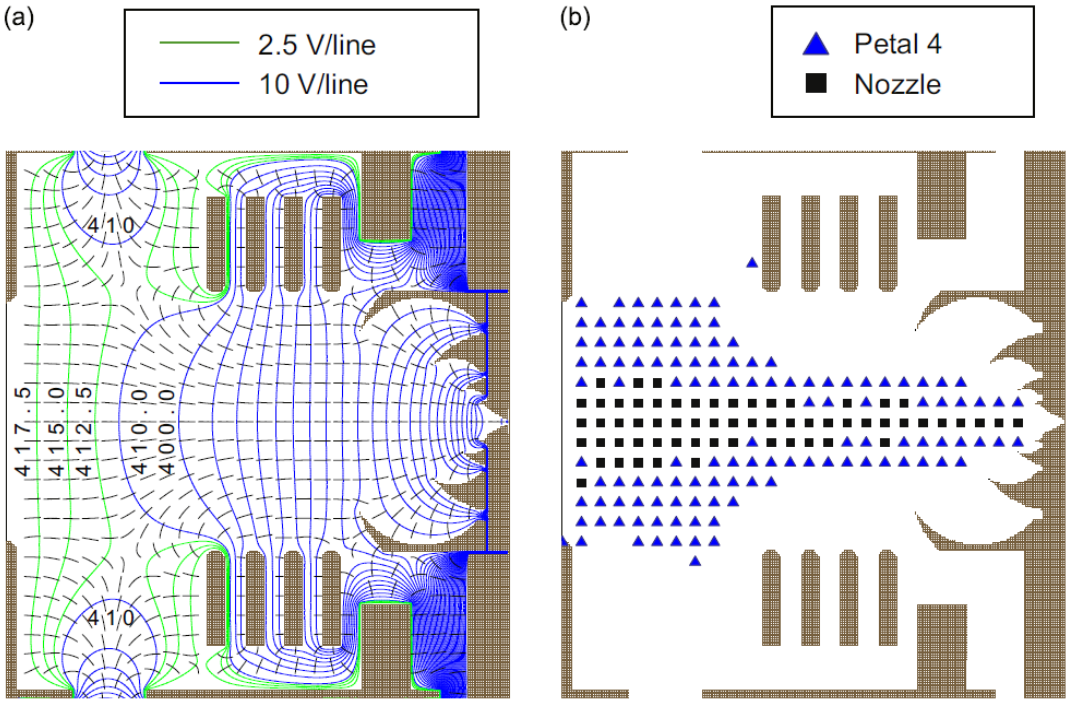

Figure 3-17. SIMION simulations of the optimum offline electrode system settings. (a) Electric field diagram. (b) "Effective volume" of the RTC. A grid of thermalized $^{216}Po^{+}$ ions with 5 mm spacing was simulated in SIMION. The black squares are ions that reached the entrance to the nozzle and blue triangles are ions that reached flower petal 4. See main text for more details.

Similar SIMION simulations and electric field diagrams were performed for the optimized online electrode settings (Figure 3-18). This time, a grid of thermalized $^{152}Er^{+}$ ions with 5-mm spacing was tested for the simulation of online settings. Figure 3-18b shows a significantly larger "effective volume" than the offline settings. The electric field diagram shows evidence that a significant portion of the ions that stop after the RTC window are being attracted to the grounded outer chamber through the Inner Chamber Groove. This is an area of the RTC that should be a focus for future improvements of the RTC's electrode system (discussed in Chapter IV).

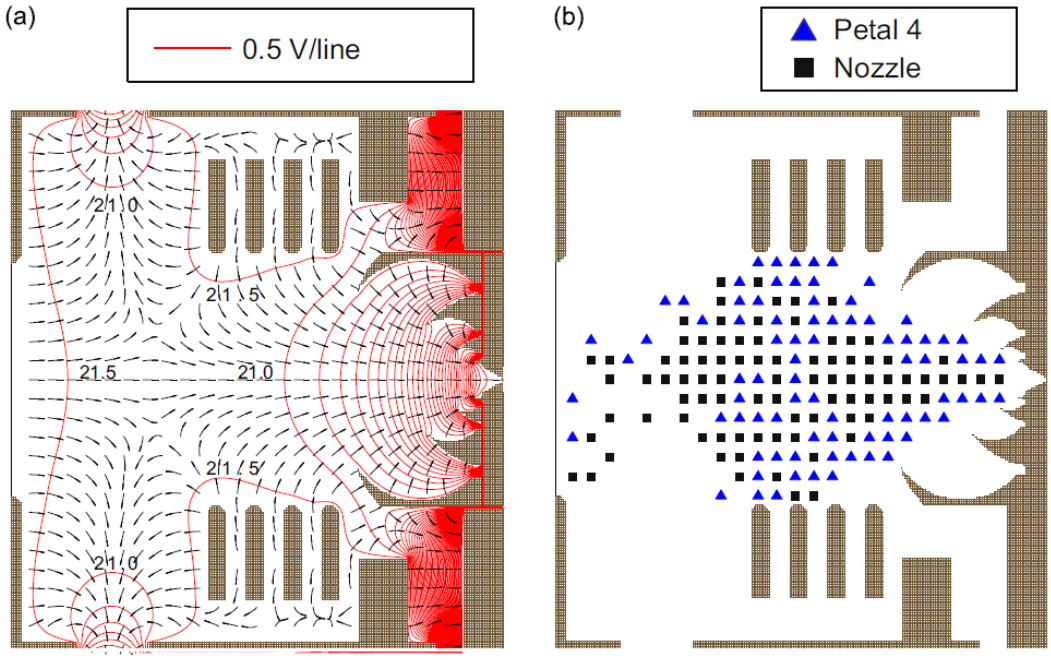

Figure 3-18. SIMION simulations of the optimum online electrode system settings. (a) Electric field diagram. (b) "Effective volume" of the RTC. A grid of thermalized 152Er^{+} ions with 5 mm spacing was simulated in SIMION. The black squares are ions that reached the entrance to the nozzle and blue triangles are ions that reached flower petal 4. See main text for more details.

3.6 Conclusions

A new gas stopper optimized for online heavy element chemistry experiments has been successfully designed, fabricated, and characterized at the Cyclotron Institute at Texas A&M University. This gas stopper is a hybrid of previously used RTCs in the transactinide field [24-26] and one used at NSCL for stopping projectile fragmentation reaction products [27-30]. The results from the online characterization of this RTC are promising for the future chemical study of online-produced elements. Table 3-4 is a summary of the maximum efficiencies measured.

Table 3-4. Summary of online results, maximum efficiencies based on different efficiency calculations. The results from the two different "modes" the RTC was run in are included.

	Gas Flow Only	Gas Flow and Electric Field
Maximum ε_{RTC} (%)	21 ± 3	35 ± 4
VAD θ, total degrader thickness (μm)	42.5°, 10.0 ± 0.2	42.5°, 10.0 ± 0.2
Maximum ε'_{RTC} (%)	25 ± 3	44 ± 5
VAD θ, total degrader thickness (μm)	45°, 10.3 ± 0.2	48°, 10.8 ± 0.20
τ_{RTC} (s)	8.5 ± 1.0	6.9 ± 0.6
Maximum ε''_{RTC} (%)	44 ± 6	70 ± 9
VAD θ, total degrader thickness (μm)	45°, 10.3 ± 0.2	48°, 10.8 ± 0.20

The directly measured maximum efficiency (ε_{RTC}) of our device is 35 ± 4%, which is comparable to the RF device built at Argonne National Laboratory (extraction efficiency 40-50%) [32]. The efficiency of our device is somewhat smaller than J. Evens *et al.* device's efficiency of 80 ± 8% [26]. Further improvements, discussed in

Chapter IV, should significantly improve the efficiency of the RTC. Our device has the advantage of a small emittance of the products exiting from the Extraction Nozzle without the use of aerosols, which would be beneficial for next-generation transactinide experiments such as precision mass measurements. Additionally our RTC has an optional AC that can be used for the more traditional liquid phase chemical studies of online-produced elements. In comparison to the gas cell normally used in the transactinide field [24-26], a wider range of chemical systems can be studied using our RTC.

CHAPTER IV

FUTURE WORK

The goal of the work presented in this dissertation was to establish the foundation for the future study the chemistry of transactinides at the Cyclotron Institute at Texas A&M University. The results of this work shows promise for both projects: commissioning of a gas stopper for the thermalization of accelerator-produced elements and offline development of a chemical system for the future study of Rf. Nevertheless, as with all research initiatives, there is still more work to be done.

4.1 Gas Stopper

The RTC built in this project has a directly measured maximum efficiency (ε_{RTC}) of 35 ± 4%. However, data suggest that the efficiency is reduced by ions being thermalized in the RTC window. This is because the stopped distribution of the EVRs is too wide in 228 torr of He gas. A solution to this problem would be to significantly increase the pressure of the RTC. Pressure tests of the RTC window show that it can hold back a pressure difference of ~760 torr. Based on results from online measurements, an RTC efficiency of 44 ± 4% (ε'_{RTC}) could be achieved by narrowing the stopped distribution of EVRs.

Data also show that the RTC's efficiency is reduced by slow transportation times. The transportation time could be faster if the potential gradient across the RTC were larger (Table 3-3). However, as shown in Section 3.5, a larger potential gradient across the RTC has a smaller "effective volume." I believe this is mostly due to the ions being

guided towards the Inner Chamber Groove by the grounded outer chamber. Evidence of this effect can be seen more clearly in the electric field diagram of the online electrode settings (Figure 3-18). A biased wire mesh across the Inner Chamber Groove could solve this problem. SIMION simulations (Figure 4-1) of this new design depict a significantly larger "effective volume." In the SIMION simulation (Figure 4-1), all electrode settings would be the same as the optimum offline electrode system settings in Figure 3-3, except that the RTC window, inner chamber, and ring 1 are set to 320 V instead of 420 V.

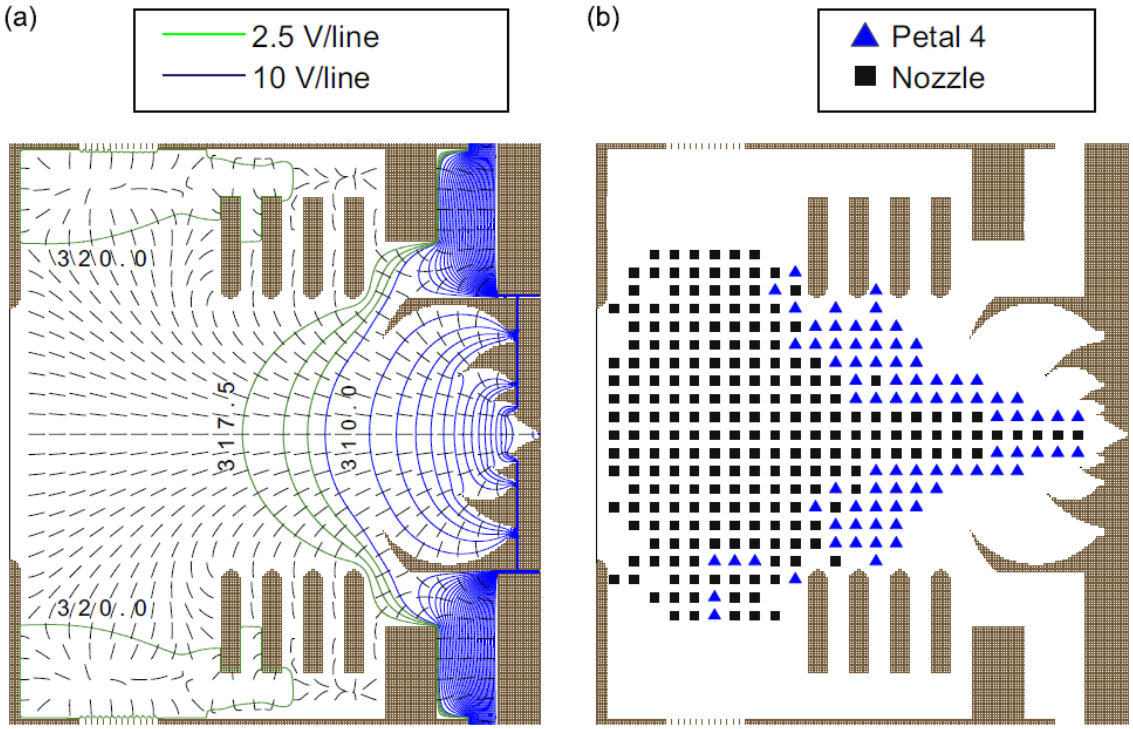

Figure 4-1. SIMION simulations of the electrode system with a wire mesh across the Inner Chamber Groove. Potential gradient across this entire device is 320 V. (a) Electric field diagram. (b) "Effective volume" of the RTC. A a grid of thermalized $^{152}Er^{+}$ ions with 5 mm spacing was simulated in SIMION. The black squares are ions that reached the entrance to the nozzle and blue triangles are ions that reached flower petal 4. See main text for more details.

4.2 Future Extraction Chromatographic Study of Rf

Two systems showed promise for the future extraction chromatographic study of Rf: TEVA and UTEVA in a HCl medium. More work is needed before these systems can be used for the study of online-produced elements.

The columns tested in this project had free column volumes of 1.3 to 1.4 ml, which is considerably larger than microcolumns commonly used in transactinide chemistry experiments. Smaller columns, with free column volumes of less than a few hundred microliters, need to be studied offline.

Another issue is that the same acid concentration is used to load the activity on the column and elute Hf from the column. This could be problematic due to possible presence of contaminants (e.g. target-like transfer products) in the sample during an online experiment, which could compete with the detection of Group IV elements. It could be possible to find a different acid concentration for the load solution that allowed for the purification of Group IV elements from contaminants. The acid concentrations would need to be optimized offline before attempting an online experiment.

REFERENCES

[1] P. Pyykkö and J.P. Desclaux, Acc. Chem. Res. **12**, 276-281 (1979).

[2] *The Chemistry of Superheavy Elements*, ed. M. Schädel and D.A. Shaughnessy, (Berlin, Germany, Springer-Verlag Berlin Heidelberg, 2014).

[3] A. Türler and V. Pershina, Chem. Rev. **113**, 1237-1312 (2013).

[4] K. Siwek-Wilczyńska, A. Borowiec, I. Skwira-Chalot, and J. Wilczyński, Int. J. Mod. Phys. E **17**, (2008).

[5] W.J. Świątecki, K. Siwek-Wilczyńska, and J. Wilczyński, Phys. Rev. C **71**, 014602 (2005).

[6] E.K. Hyde, D.C. Hoffman, and O.L. Keller Jr., Radiochim. Acta **42**, 57-102 (1987).

[7] IUPAC, Pure Appl. Chem. **69**, 2471-2473 (1997).

[8] F.P. Heßberger, S. Hoffmann, V. Ninov, P. Armbruster, H. Folger, G. Münzenberg, H.J. Schött, A.G. Popeko, A.V. Yeremin, A.N. Andreyev, and S. Saro, Z. Phys. A **359**, 415-425 (1997).

[9] I. Dragojević, K.E. Gregorich, D.A. Davies, C.E. Düllmann, M.A. Garcia, J.M. Gates, S.L. Nelson, L. Stavsetra, R. Sudowe, and H. Nitsche, Phys. Rev. C **78**, 024605 (2008).

[10] L.P. Somerville, M.J. Nurmia, J.M. Nitschke, and A. Ghiorso, Phys. Rev. C **31**, 1801-1815 (1985).

[11] E.R. Sylwester, K.E. Gregorich, D.M. Lee, B. Kadkhodayan, A. Türler, J.L. Adams, C.D. Kacher, M.R. Lane, C. Laue, C.A. McGrath, D.A. Shaughnessy, D.A. Strellis, P.A. Wilk, and D.C. Hoffman, Radiochim. Acta **88**, 837-843 (2000).

[12] M. Murakami, S. Goto, H. Murayama, T. Kojima, H. Kudo, D. Kaji, K. Morimoto, H. Haba, Y. Kudou, T. Sumita, R. Sakai, A. Yoneda, K. Morita, Y. Kasamatsu, H. Kikunaga, and T.K. Sato, Phys. Rev. C **88**, 024618 (2013).

[13] M. Thoennessen, Atomic Data and Nuclear Data Tables **99**, 312-344 (2013).

[14] E.R. Sylwester, K.E. Gregorich, D.M. Lee, B. Kadkhodayan, A. Türler, J.L. Adams, C.D. Kacher, M.R. Lane, C. Laue, C.A. McGrath, D.A. Shaughnessy, D.A. Strellis, P.A. Wilk, and D.C. Hoffman, Radiochim. Acta **88**, 837-843 (2000).

[15] J. V. Kratz, A. Nahler, U. Rieth, A. M. Kronenberg, B. Kuczewski, E. Strub, W. Bruchle, M. Schadel, B. Schausten, A. Turler, H. Gaggeler, D. T. Jost, K. E. Gregorich, H. Nitsche, C. Laue, R. Sudowe, and P.A. Wilk, Radiochim. Acta **91**, (2003).

[16] P. A. Ellison, K. E. Gregorich, J. S. Berryman, D. L. Bleuel, R. M. Clark, I. Dragojević, J. Dvorak, P. Fallon, C. Fineman-Sotomayor, J. M. Gates, O. R. Gothe, I. Y. Lee, W. D. Loveland, J. P. McLaughlin, S. Paschalis, M. Petri, J. Qian, L. Stavsetra, M. Wiedeking, and H. Nitsche, Phys. Rev. Lett. **105**, 182701 (2010).

[17] Y.T. Oganessian, V.K. Utyonkov, Y.V. Lobanov, F.S. Abdullin, A.N. Polyakov, I.V. Shirokovsky, Y.S. Tsyganov, G.G. Gulbekian, S.L. Bogomolov, B.N. Gikal, A.N. Mezentsev, S. Iliev, V.G. Subbotin, A.M. Sukhov, A.A. Voinov, G.V. Buklanov, K. Subotic, V.I. Zagrebaev, M.G. Itkis, J.B. Patin, K.J. Moody, J.F. Wild, M.A. Stoyer, N.J. Stoyer, D.A. Shaughnessy, J.M. Kenneally, P.A. Wilk, R.W. Lougheed, R.I. Ilkaev, and S.P. Vesnovskii, Phys. Rev. C **69**, 064609 (2004).

[18] J.V. Kratz, Pure Appl. Chem. **75**, 103-138 (2003).

[19] S.N. Dmitriev, Y.T. Oganessyan, V.K. Utyonkov, S.V. Shishkin, A.V. Yeremin, Y.V. Lobanov, Y.S. Tsyganov, V.I. Chepygin, E.A. Sokol, G.K. Vostokin, N.V. Aksenov, M. Hussonnois, M.G. Itkis, H.W. Gäggeler, D. Schumann, H. Bruchertseifer, R. Eichler, D.A. Shaughnessy, P.A. Wilk, J.M. Kenneally, M.A. Stoyer, and J.F. Wild, Mendeleev Commun. **15**, 1-4 (2005).

[20] N.J. Stoyer, J.H. Landrum, P.A. Wilk, K.J. Moody, J.M. Kenneally, D.A. Shaughnessy, M.A. Stoyer, J.F. Wild, R.W. Lougheed, S.N. Dmitriev, Y.T. Oganessian, S.V. Shishkin, N.V. Aksenov, E.E. Tereshatov, G.A. Bozhikov, G.K. Vostokin, V.K. Utyonkov, and A.A. Yeremin, Nucl. Phys. A **787**, 388-395 (2007).

[21] H. Wollnik, H.G. Wilhelm, G. Röbig, and H. Jungclas, Nucl. Instr. Meth. **127**, 539-545 (1975).

[22] H. Wollnik, Nucl. Instr. Meth. **139**, 311-318 (1976).

[23] R.D. MacFarlane, R.A. Gough, N.S. Oakey, and D.F. Torgerson, Nucl. Instr. Meth. **73**, 285-291 (1969).

[24] C.E. Düllmann, C.M. Folden III, K.E. Gregorich, D.C. Hoffman, D. Leitner, G.K. Pang, R. Sudowe, P.M. Zielinski, and H. Nitsche, Nucl. Instr. Meth. Phys. Res. A **551**, 528-539 (2005).

[25] H. Haba, D. Kaji, H. Kikunaga, T. Akiyama, N. Sato, K. Morimoto, A. Yoneda, K. Morita, T. Takabe, and A. Shinohara, J. Nucl. Radiochem. Sci. **8**, 55-58 (2007).

[26] J. Even, J. Ballof, W. Brüchle, R.A. Buda, C.E. Düllmann, K. Eberhardt, A. Gorshkov, E. Gromm, D. Hild, E. Jäger, J. Khuyagbaatar, J.V. Kratz, J. Krier, D. Liebe, M. Mendel, D. Nayak, K. Opel, J.P. Omtvedt, P. Reichert, J. Runke, A. Sabelnikov, F. Samadani, M. Schädel, B. Schausten, N. Scheid, E. Schimpf, A. Semchenkov, P. Thörle-Pospiech, A. Toyoshima, A. Türler, V. Vicente Vilas, N. Wiehl, T. Wunderlich, and A. Yakushev, Nucl. Instr. Meth. Phys. Res. A **638**, 157-164 (2011).

[27] L. Weissman, D.A. Davies, P.A. Lofy, and D.J. Morrissey, Nucl. Instr. Meth. Phys. Res. A **522**, 212-222 (2004).

[28] L. Weissman, D.A. Davies, P.A. Lofy, and D.J. Morrissey, Nucl. Instr. Meth. Phys. Res. A **531**, 416-427 (2004).

[29] L. Weissman, D.J. Morrissey, G. Bollen, D.A. Davies, E. Kwan, P.A. Lofy, P. Schury, S. Schwarz, C. Sumithrarachchi, T. Sun, and R. Ringle, Nucl. Instr. Meth. Phys. Res. A **540**, 245-258 (2005).

[30] P.A. Lofy, *Development of High-pressure, Gas-filled Ion Source for a Radioactive Beam Facility*. 2003, Michigan State University.

[31] M. Block, C. Bachelet, G. Bollen, M. Facina, C.M. Folden III, C. Guénaut, A.A. Kwiatkowski, D.J. Morrissey, G.K. Pang, A. Prinke, R. Ringle, J. Savory, P. Schury, and S. Schwarz, Nucl. Instr. Meth. Phys. Res. B **266**, 4521-4526 (2008).

[32] G. Savard, J. Clark, C. Boudreau, F. Buchinger, J.E. Crawford, H. Geissel, J.P. Greene, S. Gulick, A. Heinz, J.K.P. Lee, A. Levand, M. Maier, G. Münzenberg, C. Scheidenberger, D. Seweryniak, K.S. Sharma, G. Sprouse, J. Vaz, J.C. Wang, B.J. Zabransky, and Z. Zhou, Nucl. Instr. Meth. Phys. Res. B **204**, 582-586 (2003).

[33] G. Savard, Journal of Physics: Conference Series **312**, 052004 (2011).

[34] J.B. Neumayr, L. Beck, D. Habs, S. Heinz, J. Szerypo, P.G. Thirolf, V. Varentsov, F. Voit, D. Ackermann, D. Beck, M. Block, Z. Di, S.A. Eliseev, H. Geissel, F. Herfurth, F.P. Heßberger, S. Hofmann, H.J. Kluge, M. Mukherjee, G. Münzenberg, M. Petrick, W. Quint, S. Rahaman, C. Rauth, D. Rodríguez, C. Scheidenberger, G. Sikler, Z. Wang, C. Weber, W.R. Plaß, M. Breitenfeldt, A. Chaudhuri, G. Marx, L. Schweikhard, A.F. Dodonov, Y. Novikov, and M. Suhonen, Nucl. Instr. Meth. Phys. Res. B **244**, 489-500 (2006).

[35] A. Takamine, M. Wada, Y. Ishida, T. Nakamura, K. Okada, Y. Yamazaki, T. Kambara, Y. Kanai, T. M. Kojima, Y. Nakai, N. Oshima, A. Yoshida, T. Kubo, S. Ohtani, K. Noda, I. Katayama, P. Hostain, V. Varentsov, and H. Wollnik, Rev. Sci. Instrum. **76**, 103503 (2005).

[36] M. Wada, Y. Ishida, T. Nakamura, Y. Yamazaki, T. Kambara, H. Ohyama, Y. Kanai, T.M. Kojima, Y. Nakai, N. Ohshima, A. Yoshida, T. Kubo, Y. Matsuo, Y. Fukuyama, K. Okada, T. Sonoda, S. Ohtani, K. Noda, H. Kawakami, and I. Katayama, Nucl. Instr. Meth. Phys. Res. B **204**, 570-581 (2003).

[37] M. Wada, Nucl. Instr. Meth. Phys. Res. B **317**, 450-456 (2013).

[38] C. Droese, S. Eliseev, K. Blaum, M. Block, F. Herfurth, M. Laatiaoui, F. Lautenschläger, E. Minaya Ramirez, L. Schweikhard, V.V. Simon, and P.G. Thirolf, Nucl. Instr. Meth. Phys. Res. B **338**, 126-138 (2014).

[39] G. Bollen, Int. J. Mass Spectrom. **299**, 131-138 (2011).

[40] F. Arai, Y. Ito, M. Wada, P. Schury, T. Sonoda, and H. Mita, Int. J. Mass Spectrom. **362**, 56-58 (2014).

[41] M. Brodeur, A.E. Gehring, G. Bollen, S. Schwarz, and D.J. Morrissey, Int. J. Mass Spectrom. **336**, 53-60 (2013).

[42] S. Schwarz, G. Bollen, M. Brodeur, S.S. Chouhan, J. DeKamp, A.E. Gehring, N.S. Joshi, C. Magsig, D.J. Morrissey, R. Ringle, J. Ottarson, and A.F. Zeller, Nucl. Instr. Meth. Phys. Res. B **317**, 463-467 (2013).

[43] U.W. Kirbach, C.M. Folden III, T.N. Ginter, K.E. Gregorich, D.M. Lee, V. Ninov, J.P. Omtvedt, J.B. Patin, N.K. Seward, D.A. Strellis, R. Sudowe, A. Türler, P.A. Wilk, P.M. Zielinski, D.C. Hoffman, and H. Nitsche, Nucl. Instr. Meth. Phys. Res. A **484**, 587-594 (2002).

[44] D.J. Morrissey, Eur. Phys. J. Special Topics **150**, 365-366 (2007).

[45] S. Naimi, S. Nakamura, Y. Ito, H. Mita, K. Okada, A. Ozawa, P. Schury, T. Sonoda, A. Takamine, and M. Wada, International Journal of Mass Spectrometry **337**, 24-28 (2013).

[46] P. Pyykkö, Angew. Chem. Int. Ed. **43**, 4412-4456 (2004).

[47] F. Calvo, E. Pahl, M. Wormit, and P. Schwerdtfeger, Angew. Chem. Int. Ed. **52**, 7583-7585 (2013).

[48] G.T. Seaborg and W.D. Loveland, *The Elements Beyond Uranium*, (Hoboken, New Jersey, Wiley-Interscience, 1990).

[49] V.A. Glebov, L. Kasztura, V.S. Nefedov, and B.L. Zhuikov, Radiochim. Acta **46**, 117-121 (1989).

[50] B.L. Zhuikov, V.A. Glebov, V.S. Nefedov, and J. Zvara, J. Radioanal. Nucl. Chem. **143**, 103-111 (1990).

[51] B.L. Zhuikov, Y.T. Chuburkov, S.N. Timokhin, K.U. Jin, and I. Zvara, Radiochim. Acta **46**, 113-116 (1989).

[52] V. Pershina, D. Trubert, C. Le Naour, and J.V. Kratz, Radiochim. Acta **90**, 869-877 (2002).

[53] V. Pershina, D. Polakova, and J.P. Omtvedt, Radiochim. Acta **94**, 407-414 (2006).

[54] V.K. Manchanda, P.N. Pathak, and P.K. Mohapatra, *Ion Exchange and Solvent Extraction: A Series of Advances*, ed. B.A. Moyer, (Boca Raton, Florida, CRC Press, 2009).

[55] S. Siekierski, *Extraction Chromatography*, ed. T. Braun and G. Ghersini, (New York, New York, Elsevier, 1975).

[56] E.P. Horwitz, Extraction Chromatography of actinides and Selected Fission Products: Principles and Achievement of Selectivity, http://www.eichrom.com/products/extraction.aspx.

[57] R. Silva, J. Harris, M. Nurmia, K. Eskola, and A. Ghiorso, Inorg. Nucl. Chem. Letters **6**, 871-877 (1970).

[58] E.K. Hulet, R.W. Lougheed, J.F. Wild, J.H. Landrum, J.M. Nitschke, and A. Ghiorso, J. Inorg. Nucl. Chem. **42**, 79-82 (1980).

[59] K.R. Czerwinski, K.E. Gregorich, N.J. Hannink, C.D. Kacher, B.A. Kadkhodayan, S.A. Kreek, D.M. Lee, M.J. Nurmia, A. Türlerd, G.T. Seaborg, and D.C. Hoffman, Radiochim. Acta **64**, 23-28 (1994).

[60] K.R. Czerwinski, C.D. Kacher, K.E. Gregorich, T.M. Hamilton, N.J. Hannink, B.A. Kadkhodayan, S.A. Kreek, D.M. Lee, M. Nurmia, A. Türlerd, G.T. Seaborg, and D.C. Hoffman, Radiochim. Acta **64**, 29-35 (1994).

[61] W. Brüchle, E. Jäger, V. Pershina, M. Schädel, B. Schausten, R. Günther, J.V. Kratz, W. Paulus, A. Seibert, P. Thörle, S. Zauner, D. Schumann, B. Eichler, H. Gäggeler, D. Jost, and A. Türler, J. Alloys Compd. **271–273**, 300-302 (1998).

[62] R. Günther, W. Paulus, J.V. Kratz, A. Seibert, P. Thörle, S. Zauner, W. Brüchle, E. Jäger, V. Pershina, M. Schädel, B. Schausten, D. Schumann, B. Eichler, H.W. Gäggeler, D.T. Jost, and A. Türler, Radiochim. Acta **80**, 121-128 (1998).

[63] H. Haba, K. Tsukada, M. Asai, S. Goto, A. A. Toyoshima, I. Nishinaka, A. K.;, H. M.;, S. Ichikawa, Y. Nagame, Y. Shoji, M. Shigekawa, T. Koike, M. Iwasaki, A. Shinohara, T. Kaneko, T. Maruyama, S. Ono, H. Kudo, Y. Oura, K. Sueki, H. Nakahara, M. Sakama, A. Yokoyama, J.V. Kratz, M. Schädel, and W. Brüchle, J. Nucl. Radiochem. Sci. **3**, 143-146 (2002).

[64] H. Haba, K. Tsukada, M. Asai, A. Toyoshima, Y. Ishii, H. Toume, T. Sato, I. Nishinaka, T. Ichikawa, S. Ichikawa, Y. Nagame, W. Sato, K. Matsuo, Y. Kitamoto, Y. Tashiro, A. Shinohara, J. Saito, M. Ito, T. Ikezawa, M. Sakamaki, S. Goto, H. Kudo, H. Kikunaga, M. Arai, S. Kamataki, A. Yokoyama, K. Akiyama, K. Sueki, Y. Oura, M. Schädel, W. Brüchle, and J.V. Kratz, Radiochim. Acta **95**, 1-6 (2007).

[65] A. Toyoshima, Y. Kasamatsu, K. Tsukada, M. Asai, Y. Ishii, H. Toume, I. Nishinaka, T.K. Sato, Y. Nagame, M. Schädel, H. Haba, S. Goto, H. Kudo, K. Akiyama, Y. Oura, K. Ooe, A. Shinohara, K. Sueki, and J.V. Kratz, J. Nucl. Radiochem. Sci. **11**, 7-11 (2010).

[66] E.P. Horwitz, M.L. Dietz, R. Chiarizia, H. Diamond, S.L. Maxwell, and M.R. Nelson, Anal. Chim. Acta. **310**, 63-78 (1995).

[67] E.P. Horwitz, M.L. Dietz, R. Chiarizia, H. Diamond, A.M. Essling, and D. Graczyk, Anal. Chim. Acta. **266**, 25-37 (1992).

[68] K.A. Kraus and F. Nelson. *Anion-exchange studies of the fission products*. in *Proceedings of the international conference on the peaceful uses of atomic energy*. 1955. United Nations Publishers.

[69] M.E. Bennett, D.A. Mayorov, K.D. Chapkin, M.C. Alfonso, T.A. Werke, and C.M. Folden III, Nucl. Instr. Meth. Phys. Res. B **276**, 62-65 (2012).

[70] National Nuclear Data Center (2016), available at http://www.nndc.bnl.gov.

[71] E.P. Horwitz, R. Chiarizia, and M.L. Dietz, Solvent Extr. Ion Exch. **10**, 313-336 (1992).

[72] PerkinElmer Wizard 2480 Automatic Well-Type NaI Gamma Counter Manual.

[73] F. Kaihong, W. Dawei, Y. Shaobo, Z. Jiangtao, P. Haibo, W. Qiang, and W. Tieshan, Applied Radiation and Isotopes **70**, 2328-2331 (2012).

[74] M.F. L'Annunziata, *Handbook of Radioactivity Analysis*, (Cambridge, Massachusetts, Academic Press, 2012).

[75] D.J. Storm and P.S. Stansbury, J. Health Phys. **63**, 360-361 (1992).

[76] J.I. Kim, H. Lagally, and H.J. Born, Anal. Chim. Acta. **64**, 29-43 (1973).

[77] J.P. Faris and R.F. Buchanan, Anal. Chem. **36**, 1157-1158 (1964).

[78] R. Caletka, R. Hausbeck, and V. Krivan, J. Radioanal. Nucl. Chem. **142**, 383-391 (1990).

[79] Z.J. Li, A. Toyoshime, K. Tsukada, and Y. Nagame, Radiochim. Acta **98**, 7-12 (2010).

[80] L.I. Guseva and G.S. Tikhomirova, Radiochemistry **44**, 337-341 (2002).

[81] R.E. Connick and W.H. McVey, J. Am. Chem. Soc. **71**, 3182-3191 (1949).

[82] J.F.Ziegler, Computer Code SRIM-2010, available at http://www.srim.org.

[83] J.F. Ziegler, M.D. Ziegler, and J.P. Biersack, Nucl. Instr. Meth. Phys. Res. B **268**, 1818-1823 (2010).

[84] R. Sudowe, M.G. Calvert, C.E. Düllmann, L.M. Farina, C.M.F. III, K.E. Gregorich, S.E.H. Gallaher, D.C. Hoffman, S.L. Nelson, D.C. Phillips, J.M. Schwantes, R.E. Wilson, P.M. Zielinski, and H. Nitsche, Radiochim. Acta **94**, 123–129 (2006).

[85] C.E. Düllmann, K.E. Gregorich, G.K. Pang, I. Dragojević, R.d. Eichler, C.M. Folden III, M.A. Garcia, J.M. Gates, D.C. Hoffman, S.L. Nelson, R. Sudowe, and H. Nitsche, Radiochim. Acta **97**, 403-418 (2009).

[86] O.B. Tarasov and D. Bazin, Nucl. Phys. A **746**, 411-414 (2004).

[87] R. Johnsen and M.A. Biondi, J. Chem. Phys. **57**, 5292-5295 (1972).

[88] Computer Code SIMION, available at http://www.simion.com.

[89] A.D. Appelhans, J.E. Delmore, and J.E. Olson, Int. J. Mass Spectrom. **241**, 1-9 (2005).

[90] CD-adapco, Computer Code STAR-CCM+, available at http://www.cd-adapco.com/products/star-ccm.

[91] R. Sudowe, D.A. Shaughnessy, and K.J. Moody, (private communication).

[92] Monotorr Brochure, http://www.saespuregas.com/Library/specifications-brochures/monotorr_brochure_551.pdf.

[93] National Instruments, Computer Code LABVIEW, available at http://www.ni.com/labview.

[94] A.J. Howard, Nucl. Instr. Meth. Phys. Res. B **73**, 53-62 (1993).

[95] K. Hámori, M. Váradi, and J. Csikai, Appl. Radiat. Isot. **64**, 854-857 (2006).

[96] H. Gauvin, Y.L. Beyec, M. Lefort, and R.L. Hahn, Phys. Rev. C **10**, 722-728 (1974).

[97] H. Gauvin, Y.L. Beyec, and N.T. Porile, Nucl. Phys. **A223**, 103-117 (1974).

[98] R.L. Hahn, K.S. Toth, C. Cabot, H. Gauvin, and Y. LeBeyec, Phys. Rev. Lett. **42**, 218-221 (1979).

[99] E. Segrè, *Nuclei and Particles: An Introduction to Nuclear and Subnuclear Physics* (Massachusetts, Benjamin-Cummings, 1977).

[100] R.E. Tribble, R.H. Burch, and C.A. Gagliardi, Nucl. Instr. Meth. Phys. Res. A **285**, 441-446 (1989).

[101] C.M. Folden III, M.C. Alfonso, D.A. Mayorov, K.R. Lawrence, A.A. Alharbi, E. Berdugo, P.J. Cammarata, A.C. Raphelt, B.T. Roeder, and T.A. Werke, Nucl. Instr. Meth. Phys. Res. A **678**, 1-7 (2012).

[102] C.C. Sahm, H.G. Clerc, K.H. Schmidt, W. Reisdorf, P. Armbruster, F.P. Hessberger, J.G. Keller, G. Münzenberg, and D. Vermeulen, Nucl. Phys. A **441**, 316-343 (1985).

[103] R. Dressler, D. Piguet, A. Serov, and R. Eichler, PSI Annual Report 2006, 7 (2007).

[104] Y. Ito, P. Schury, M. Wada, S. Naimi, T. Sonoda, H. Mita, F. Arai, A. Takamine, K. Okada, A. Ozawa, and H. Wollnik, Physical Review C **88**, 011306 (2013).

APPENDIX: SUMMARY OF EXISTING GAS CELLS UTILIZING RF ION-GUIDE DESIGN

In 2006, a gas cell that used the RF funnel design was built at GSI (Figure A-1) [34]. This device consisted of forty 1-mm-thick stainless steel rings spaced 1 mm apart. The inner diameter of the forty rings decreased from 130 to 5 mm. At the end of the RF funnel was an extraction nozzle with a 0.6-mm inner diameter. The GSI gas cell used a DC field ring system upstream to guide the ions into the RF funnel. This device was optimized using the fusion evaporation reactions ^{121}Sb(^{35}Cl, 4n)^{152}Er and ^{118}Sn(^{40}Ar, 6n)^{152}Er. An overall efficiency (stopping and extraction) between 4% and 8% was measured with an average extraction time of approximately 10 ms [34]. The optimum peak-to-peak voltage difference between neighboring electrodes was determined to be 190 to 200 V with a frequency of 700 kHz and a DC gradient of 10 V/cm. After exiting the RF funnel, the gas increased to supersonic speeds and gas flow became the dominant force guiding the ions through the extraction nozzle. This occurred due to the large pressure difference (50–10^{-2} mbar) across the extraction nozzle [34].

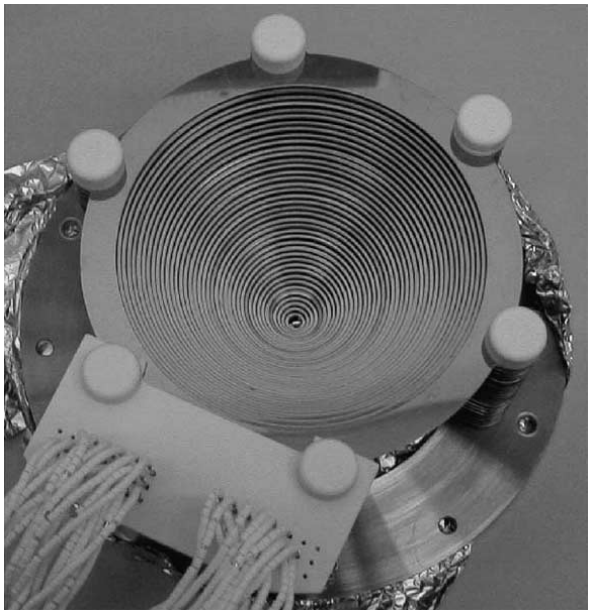

Figure A-1. Photograph of an RF funnel used at GSI. See text for more detail. Figure from Nucl. Instr. Meth. Phys. Res. B [34].

Since the early 2000s, Argonne National Laboratory has built multiple RF devices for the thermalization of both fusion-evaporation and fragmentation products [32, 33]. These devices use either a DC ring system or an RF wall to guide the ions into a RF funnel. The size of the device changes depending on the energy of the products (see section 1.2.3.1). A small gas catcher system for stopping EVRs was tested and G. Savard *et al.* claimed an extraction efficiency of 40-50% with a transportation time of 10 ms [32].

RF carpets can be used in place of RF funnels [35-37]. A benefit of RF carpets is that the electrodes can be made on a printed circuit board, which makes it possible to create very fine electrode structures. This is advantageous because F_{RF} is inversely proportional to the distance between adjacent electrodes [37]. RF carpet gas catchers

have been used to facilitate high-precision mass measurements of short-lived nuclei such as ^{8}Li ($t_{½}$ = 838 ms) with a multi-reflection time-of-flight spectrograph [104]. Figure A-2 (left) shows a photograph of an RF carpet used at the Institute of Physical and Chemical Research in Japan, Rikagaku Kenkyusho (RIKEN) [37]. This RF carpet is printed on Kapton (polyamide film). The ring electrodes are 80 µm thick and are spaced 80 µm apart, and the exit hole diameter is 0.3 mm. The simulated trajectory of an ion is shown in the right side of Figure A-2: The DC field guides the ions onto the RF carpet, the RF field keeps the ions from touching the electrodes, and the decreasing potential gradient across the RF carpet moves the ions to the exit hole. This particular device has an ion guide efficiency of ~30% [37]. Currently, a group at RIKEN is working on a similar system to measure the mass of transactinides [45].

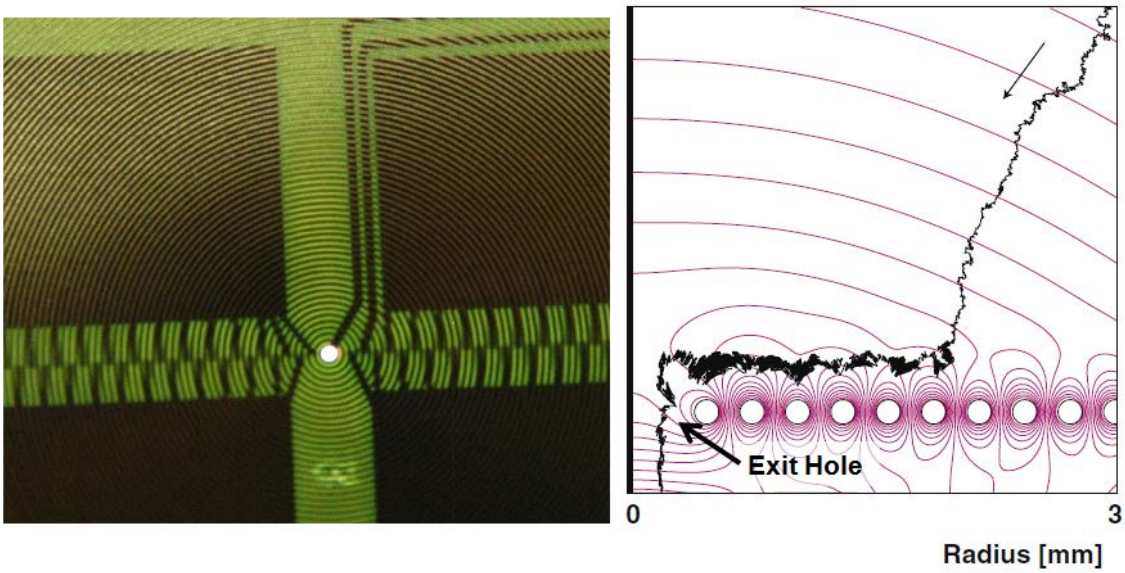

Figure A-2. RF carpet at the Institute of Physical and Chemical Research in Japan, Rikagaku Kenkyusho (RIKEN). Left: Photograph of an RF carpet used. Right: Simulation showing the trajectory of ions across the RF carpet. See text for more detail. Figures from Nucl. Instr. Meth. Phys. Res. B [37].

RF carpets are also used in a new method known as "ion surfing" [37, 39-41]. This method transports the ions across the device using a traveling wave instead of a static decreasing potential gradient. Due to breakdown voltage, the typical limit on the DC field in RF devices is 10-40 V/cm [39-41], which hinders the minimum possible transportation time. However, ion surfing makes it possible to achieve shorter transportation times with lower maximum voltages [39-41].

With ion surfing devices, an extra force, F_P, is needed to keep the ions close to the carpet electrodes in order for them to be transported by the traveling wave [39-41]. This force is generated by a biased planar electrode (known as a push plate) placed above the RF carpet (Figure A-3). The traveling wave originates from an audio frequency signal (kHz range) that is superimposed onto the electrodes, causing adjacent

electrodes to be 90° out of phase from each other (Figure A-3) [41]. The amplitude and velocity, v_w, of the traveling wave control the transport velocity of the ion, v_i. If the amplitude is too low, the ion can "slip out" of the traveling wave; this happens because the viscous drag force of the He gas is larger than the force of the traveling wave parallel to the carpet electrodes, so v_i is less than v_w. Increasing the amplitude decreases the chance of the ion slipping out by keeping the ion "locked" to the traveling wave so that v_i equals v_w. However, if the traveling wave's amplitude is too large, the force of the wave in the direction of the carpet electrodes could cause the ions to collide with them [39].

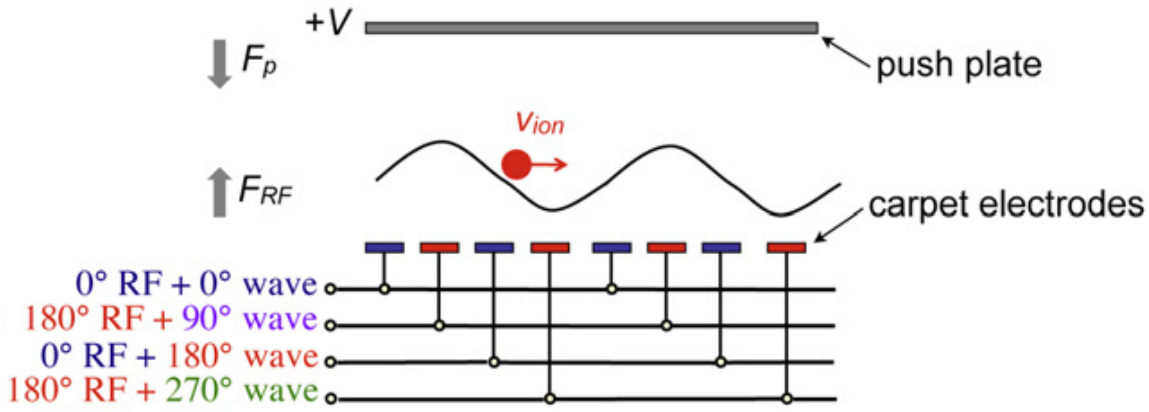

Figure A-3. Conceptual schematic of ion surfing device. F_{RF} is the repulsive force created by the carpet electrodes and F_P is the push force created by the positively biased push plate. Figure from Int. J. Mass Spectrom. [41].

The ion surfing technique is in the preliminary phase but shows great promise. Tests of recent ion surfing devices have simulated ion transport velocities greater than 200 m/s at a He pressure of 100 mbar. In a first generation RF carpet device, this would

require a DC gradient of about 100 V/cm [39], which is well above the breakdown voltage threshold of 10-40 V/cm. A group at RIKEN tested an ion surfing device with a thermal K^+ ion source and claimed that an ion guide efficiency of 100% is achievable [40].

RF ion-guided gas catchers have proven useful for the thermalization and transportation of projectile fragmentation and fusion-evaporation reaction products. They have transportation times on the order of milliseconds with varying extraction efficiencies (10-50%). However, these systems are complex and require a larger number of component s [31-34]. One device built at Argonne National Laboratory had over 7000 parts [33]. Also, the efficiency of these devices depends on the purity of the He, and the components must be cleaned to high vacuum standards [32, 35, 37]. On the other hand, RF carpet gas cells require significantly fewer parts (a printed circuit board instead of 40 to 80 individual rings, each with their own insulator and circuit) [35-37]. However, the circuit board material outgases impurities, decreasing the purity of the He in the gas cell [37]. One solution is cryogenic cooling of the entire gas cell, which has been shown to reduce the levels of impurities of a RF device [37, 38]. Recently, GSI researchers built a second-generation RF funnel gas cell that implements cryogenic cooling, and preliminary radioactive source measurements showed the ion guide efficiency increasing by a factor of 2 [38]. However, this process adds an additional level of complexity to the design.